STEADY-STATE AND DYNAMIC MODELING OF A CHLOR-ALKALI CELL WITH OXYGEN DEPOLARIZED CATHODE

Doctoral Thesis
(Dissertation)

to be awarded the degree of
Doctor of Engineering (Dr.-Ing.)

submitted by
M. Sc. Nareshkumar Chavan
from Faizpur, India

approved by the Faculty of
Mathematics/Computer Science and Mechanical Engineering
Clausthal University of Technology

Date of oral examination
24 June 2015

Chairperson of the Board of Examiners

Prof. Dr. rer. nat. Alfred Weber

Chief Reviewer

Prof. Dr.-Ing. Thomas Turek

Reviewer

Prof. Dr.-Ing. Ulrich Kunz

PREFACE

This dissertation is the result of my work at Clausthal University of Technology (TUC) between December 2008 and December 2011. In 2006, due to the initiative of Bayer MaterialScience (BMS) joint research started in association with 12 project partners. This project was funded by the German Ministry of Education and Research (BMBF) for work on the project of *CO$_2$ Reduction During the Production of Basic Chemicals*. One of the important goals of the project was to reduce the cell voltage down to 2.2 V – 2 V of the chlor-alkali cell by using a Oxygen Depolarized Cathode (ODC). Eventually, successful outcome of the project should be a commercially viable technology for chlor-alkali cell based ODC. TUC was also one of the project partners; manufacturing of the ODCs and mathematical modeling was the assigned responsibilities at TUC. Other project partners were from the universities and the industries. Total budget allocated to the project was € 12.3 million over a period of four years. Professor Turek gave me the opportunity to work on this industrially relevant project as a Ph. D. student. During my initial tenure at TUC, I manufactured the electrodes and tested them in bench scale electrolyzer; later started modeling.

This modeling dissertation is for those who are interested in ODC based chlor-alkali cell as well as gas diffusion electrode. To understand throughly, some relevant background of physical chemistry and electrochemical process engineering is desirable.

ABSTRACT

Chlor-alkali electrolysis, the electrolytic splitting of NaCl solutions, is an energy intensive process. The most modern variant, the membrane electrolysis process, has been continuously improved over the last decades. Nevertheless, the average energy demand with the current state of the art of this technology is 2292 kWh/t$_{Cl_2}$ at 6 kA/m^2. Consequently, any reduction of the electrical energy demand in chlor-alkali electrolysis would be highly desirable for both economic and environmental reasons. Replacing hydrogen evolving reaction by oxygen reduction reaction can reduce the energy demand by approximately 30%. In this work mathematical models in steady and dynamic state for an industrial scale chlor-alkali electrolysis cell with ODC is developed.

The steady state model predicts the distributions of temperature, concentration, current density, and overpotential as a function of height. At an industrially relevant current density of 4 kA/m^2 neither current density nor overpotentials exhibit strong variations along the cell height. Main reason for this behavior is the uniformity of temperature distributions in the solid compartments of the cell (anode, membrane, ODC) which can be explained by efficient heat transfer between the electrodes and the electrolyte streams. This is especially true for the caustic solution, through which most of the irreversible heat released in the cell is removed. However, the temperature of the oxygen stream increases slowly along the height. Due to the initially low temperatures and the low water content of the inlet oxygen stream, the gas phase takes up considerable net amounts of water vapor. Nevertheless, the oxygen partial pressure at the electrochemically active regions of the ODC remains high allowing for efficient operation of the cathode. Operating cell at higher current requires better heat management as the heat production is high. However, cell operating at lower oxygen partial pressure up to 90% won't affect the performance of the electrode significantly.

The dynamic model predicts the performance of the electrode un-

der the ripple voltage. However, Current Interruption (CI) measurements have been used to validate this model. Due to ripples, hysteresis appears at even low frequency of 100 Hz. As frequency increases the amplitude of current oscillation reduce. No significant difference in the hysteresis can be seen after lowering oxygen partial pressure up to 75%.

Gratitude is the inward feeling of kindness received.
Thankfulness is the natural impulse to express that feeling.
Thanksgiving is the following of that impulse.
—Henry Van Dyke.

ACKNOWLEDGMENTS

CONTENTS

LIST OF FIGURES

LIST OF TABLES

LIST OF ABBREVIATIONS

BMBF German Ministry of Education and Research

BMS Bayer MaterialScience

CI Current Interruption

CSTR Continuous Stirred-Tank Reactor

GDE Gas Diffusion Electrode

GDL Gas Diffusion Layer

NaCl-ODC NaCl electrolyzer based on Oxygen Depolarized Cathode

ODC Oxygen Depolarized Cathode

ORR Oxygen Reduction Reaction

PSA Pressure Swing Adsorption

PTFE Polytetrafluoroethylene

RL Reaction Layer

TFFA Thin-Film Flooded Agglomerate

DC Direct Current

AC Alternating Current

LIST OF SYMBOLS

A Area of the electrode (m^2)

b Width of the electrode (m)

c Molar concentration of oxygen dissolved in NaOH solution at boundary film-agglomerate (mol/m^3)

c^* Molar concentration of dissolved oxygen in NaOH solution at the boundary of gas-film (mol/m^3)

c_{ag} O_2 concentration in agglomerate (mol/m^3)

C_H Constant related to heat of oxygen dissolution in caustic (K)

C_p Molar heat capacity (J/molK)

c_p Specific heat capacity (J/kgK)

d Thickness (m)

$D_{i,j}$ Binary diffusion coefficient of species i and j (m^2/s)

$D_{O_2}^l$	Diffusivity of oxygen in caustic solution (m^2/s)
E	Equilibrium potential (V)
F	Faraday's constant (96485 C/mol)
G	Gibbs free energy (J/mol)
H	Enthalpy (J/mol)
h	Height of the electrode (m)
H_{dil}	Enthalpy of dilution (J/kg)
He	Henry's constant of oxygen in caustic solution ($Pa\,m^3/mol$)
H_{wg}	Specific enthalpy of water vapor (J/kg)
H_{wl}	Specific enthalpy of liquid water (J/kg)
j	Local current density (A/m^2)
j_0	Exchange current density (A/m^2)
j_{di}	Double layer current density (A/m^2)
j_{tf}	Faradic current density (A/m^2)
C_H	Constant related heat of dissolution of oxygen in caustic solution (K)
K_i	Thermal conductivity of species i (W/m K)
Le	Lewis Number (dimensionless)
M	Molar mass (kg/kmol)
$\dot{m}_i$	Mass flow rate of species i (kg/h)
n	Number of electrons in half-cell reaction (dimensionless)
n_d	Number of moles of water flowing per mole of Na^+ ion (mol/mol)

N_i	Flux of species i (mol/m^2 s)
P	Pressure (Pa)
P_{O_2}	O$_2$ partial pressure (Pa)
Q	Heat (J/mol)
$\dot{Q}$	Heat flow rate gradient (W/m)
$\dot{q}$	Heat (W)
R	Resistances (V)
r	Rate of reaction (mol/m^{3}s)
r_{ag}	Radius of agglomerate (m)
R_j	Rate of production or consumption of the species j (kg/s)
R_{th}	Contact resistance (m^2 K/W)
S	Entropy (J/mol K)
S_{tf}	Specific surface of thin-film per total volume of reaction layer (m^2/m^3)
T	Temperature (K)
T_s	Tafel slope (V/decade)
U	Heat transfer coefficient (W/m^2 K)
U_{cell}	Total cell voltage (V)
U_{tn}	Thermo-neutral cell voltage (V)
V	Voltage (V)
w_i	Mass fraction of species i (kg/kg)
x	Height domain (m)
z'	Length domain of gas diffusion layer (m)
z''	Length domain of boundary layer (m)

z_s	Thickness of gas diffusion layer (m)
z_t	Thickness of reaction layer (m)

Greek symbols

α	Heat transfer coefficient (W/m^{2}K)
δ	Thickness of boundary layer (m)
δ_{tf}	Thickness of electrolyte film (m)
ϵ	Porosity (m^3/m^3)
ϵ_{ano}	Fraction of contact area between anode and membrane (m^2/m^2)
η	Overpotential (V)
κ	Ionic conductivity (S/m)
μ	Viscosity of caustic solution (Pa s)
ν	Stoichiometric coefficient (dimensionless)
φ	Potential (V)
τ	Relaxation time (s)

Subscripts

Ag	Silver
ano	Anode
avg	Average
b	Boundary layer
brine	Related to brine solution or it's chamber
caustic	Related to caustic solution or it's chamber
conc	Concentration
DC	Direct Current

e	Electronic, solid phase of agglomerate
eff	Effective
gas	Mixture of oxygen and water vapor
in	Inlet for height dependent model and ionic for CI model
irr	Irreversible
Joule	Related to Joule heat
kr	Kinetic relaxation
λ	Related to phase change
l	Liquid
loss	Loss to the surrounding
mem	Membrane
n	Agglomerate phase
Ni	Nickel
ODC	Oxygen depolarized cathode
out	Outlet
peak	Peak voltage
PTFE	Polytetrafluoroethylene
ref	Reference value
rev	Reversible
r	Ripple
s	Gas diffusion layer
sd	Solid
t	Gas phase in reaction layer
tf	Thin film

thermal   Thermal

T   Total

Superscripts

⊖   Standard conditions

sat   Saturation

INTRODUCTION

*"The first step to knowledge
is to know that we are ignorent."*
— *Socrates*

CHLOR-ALKALI ELECTROLYSIS

Chlorine has an exceptional importance in chemistry and, so in our lives. It is involved in over 50% of all commercial chemistry [1]; even though, it may not be present in the final product. For example, it is used to produce polymers, pesticides, high purity silicon for photo-voltaic applications, and lifesaving pharmaceuticals. Biggest use (35%) of chlorine is for manufacturing polyvinyl chloride [2]. Worldwide chlorine production capacity was 84 Mt/a in the year 2012 [3]. Growth in chlorine production indicates the developments of and in the chemical industry.

Chlorine is produced by energy intensive electrolysis of NaCl solution. Germany alone produces 41% of Europe's chlorine, which makes it the largest producer in the Europe [4]. The European chlor-alkali industry consumes about 35 TWh of electricity per year [5]. Electricity consumption of NaCl electrolysis by membrane process is about 2400 to 3000 kWh/t_{C_2} [6]. The current state of the art of this technology still requires 2035 kWh/t_{NaOH} ($\equiv$ 2292 kWh/t_{Cl_2}) at 6 kA/m^2 [7]. 90% of the electricity is used only for the electrolysis and rest 10% are used for operating pumps and compressor like equipment [2]. The European Union-Emissions Trading system (EU-ETS) directive compels to include indirect CO_2 emission cost in electricity prices [5]. This hampers the competitiveness of European chlor-alkali industry compared to the regions where electricity is cheaper than the Europe. Therefore, the optimization strategy should be reducing the electricity demand. It will also reduce possible emission of CO_2 during production of electricity.

About 95% of chlorine is produced by electrolysis of sodium chloride solution. This work focus only on the NaCl electrolysis. There are three main production processes,

- The diaphragm cell (Greisheim cell) since 1885

- The mercury cell (Castner-Kellner cell) since 1892 and

- The membrane process since 1970

Among these, the membrane process is the least energy intensive and competitive process contrary to the mercury cell, which consumes the highest amount of electricity. Membrane cell reduces approximately thirty percent of electrical demand than the mercury cell [6, 8]. While mercury and diaphragm cell produce approximately 70% of world chlorine [9]. Diaphragm technology is predominate in the United States, Russia and China [9]. Due to the environmental regulation and economic benefits, membrane chlor-alkali cell is used in Europe. Since 1999, all production sites in Japan were made to switch to the membrane cell. Summary of usage of production technologies, in Europe and Germany is given in table 1.1.

Table 1.1: Percentage of mass of chlorine produced in Europe by different processes in year 2014[*] [10]

	Amalgam	Diaphragm	Membrane	Other [†]
Europe	24.6	13.6	58.8	3.0
Germany	11.8	22.4	60.0	5.7

1.1.1 *Diaphragm cell*

First commercial technology was developed by Griesheim Company, in Germany. In this type of cell Cl_2 is produced at the anode

---

[*] total production 12.4 kt_{Cl_2}

[†] electrolysis of HCl or moltan salt electrolysis

and cathode generates H_2 and NaOH. Half-cell reactions and total cell reaction is given by eqs. (R 1.1) to (R 1.3).

$$\text{anode:} \qquad 2\,Cl^- \longrightarrow Cl_2 + 2\,e^- \qquad\qquad\qquad \text{(R 1.1)}$$

$$\text{cathode:} \qquad 2\,H_2O + 2\,e^- \longrightarrow H_2 + 2\,OH^- \qquad\qquad \text{(R 1.2)}$$

$$\text{total reaction:}\ \ 2\,NaCl + 2\,H_2O \longrightarrow Cl_2 + H_2 + 2\,NaOH \quad \text{(R 1.3)}$$
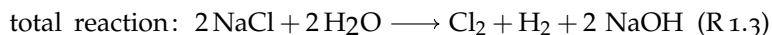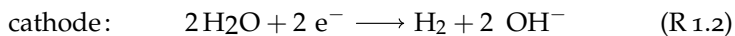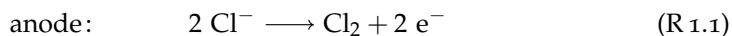
In this design, anode and cathode are separated by permeable asbestos diaphragm (see fig. 1.1). It separates the anolyte and catholyte chambers. The anode is mesh type Dimensionally Stable Anode (DSA®) with the base material of the anode being a titanium mesh coated with $RuO_2 + TiO_2 + SnO_2$, while the cathode is made of carbon steel [11]. Brine (NaCl solution) enters in the anolyte chamber and chlorine ions get oxidized to produce Cl_2. At the outlet of anolyte chamber Cl_2 gets saturated with water vapor. Further processing is required to make Cl_2 free from moisture and other impurities. Depleted brine flows into the catholyte chamber, through the permeable diaphragm. Upon reduction of water at cathode—H_2 and caustic (NaOH solution) is produced. Stream leaving the catholyte compartment contains both brine and caustic (12% by weight) which is concentrated in the downstream process. Separated NaCl salt can be reused to saturate reactant brine.

1.1.2 *Mercury cell*

Hamilton Y. Castner and Karl Kellner developed the mercury cell in 1892—known as Castner-Kellner cell. Major difference of the diaphragm and mercury cell is the cathode reaction, the anode reaction being the same. Figure 1.2 shows the schematic diagram of the cell. Mercury cell produces chlorine gas and Na-Hg is decomposed in the decomposer. Reaction of brine electrolyzer and decomposer are given by eqs. (R 1.4) to (R 1.6)
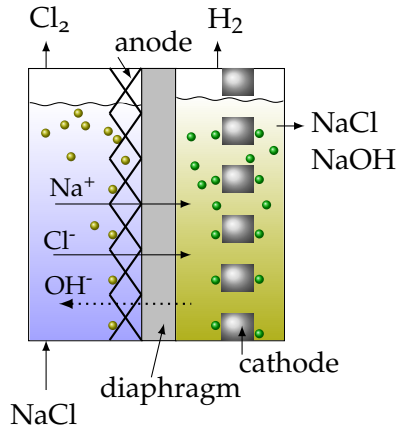
Figure 1.1: Schematic diagram of diaphragm cell.

in electrolyzer

$$\text{anode:} \qquad 2\,Cl^- \longrightarrow Cl_2 + 2\,e^- \qquad\qquad \text{(R 1.4)}$$

$$\text{cathode:} \qquad 2\,Na^+ + 2\,Hg + 2\,e^- \longrightarrow 2\,Na{-}Hg \qquad \text{(R 1.5)}$$

$$\text{total reaction:} \quad 2\,NaCl + 2\,Hg \longrightarrow 2\,Na{-}Hg + Cl_2 \qquad \text{(R 1.6)}$$
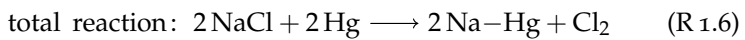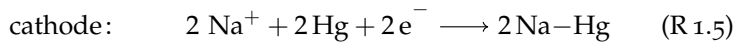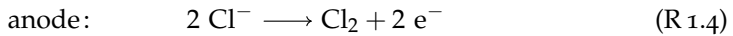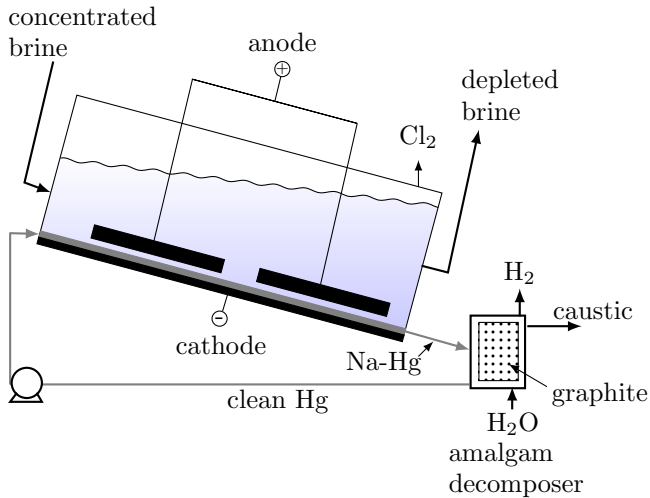
Figure 1.2: Schematic diagram of mercury-cell.

Brine electrolyzer consists of a slightly inclined trough through which the brine flows from this trough. While the anode is made of titanium; coated with $RuO_2 + TiO_2$ and the cathode is made up of Nickel [11]. Anode's bottom surface is close to the film of sodium amalgam. Brine reaction at the cathode generates Na metal from Na^+ ions migrating toward the mercury cathode, which dissolves in the mercury. Cl_2 gas is formed at anode. Cl_2 produced by this process is almost pure and can be used without any further treatment. Reduction of Na^+ ions at the cathode generates low concentration of sodium about 0.1 to 0.3% (by weight). $Na-Hg$ reacts with H_2O in the decomposer to produces H_2 and pure concentrated caustic (50% by weight). Pure Hg from the decomposer is recirculated to the electrolyzer with the help of a pump. In Europe, mercury cell based chlorine producers voluntary declared to shift to non-mercury technology, by 2020 [12].
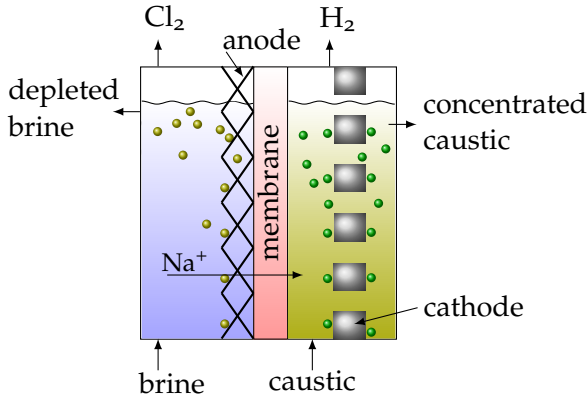
Figure 1.3: Schematic diagram of membrane cell. (conventional cell)

1.1.3 *Membrane cell*

The major difference in diaphragm and membrane cell is that, the diaphragm is replaced by the selective ion conducting membrane. Reactions at anode and cathode are the same as given by eqs. (R 1.1) to (R 1.3). The membrane passes only Na^+ from the anolyte to the catholyte chamber, shown in fig. 1.3. Thus avoiding the brine crossover to the catholyte chamber. Membranes for this technology are manufactured by DuPont/USA, Asahi Glass, and Asahi Chemical/Japan under the trade names Nafion®, Flemion®, and Aciplex® respectively. Contrary to the diaphragm cell, depleted brine can be obtained easily. Brine can be re-used, after de-chlorination and saturating with solid salt. The anode is the mesh type made of titanium coated with $RuO_2 + TiO_2 + IrO_2$ and cathode is made of Ni [11]. Instead of using pure water for cathode reaction, caustic solution is fed to the electrolyzer. This strategy reduces ohmic losses, due to the caustic solution's higher ionic conductivity than pure water. Caustic solution is recycled to maintain the concentration in desired range and for heat removal. Finally as products hydrogen gas, and concentrated caustic are obtained at the outlet of catholyte chamber. This is the

7

anode reaction

$$2\ Cl^- \longrightarrow Cl_2 + 2\ e^-$$

ODC reaction

$$H_2O + \tfrac{1}{2}\ O_2 + 2\ e^- \longrightarrow 2\ OH^-$$

conventional cathode reaction

$$2\ H_2O + 2\ e^- \longrightarrow H_2 + 2\ OH^-$$
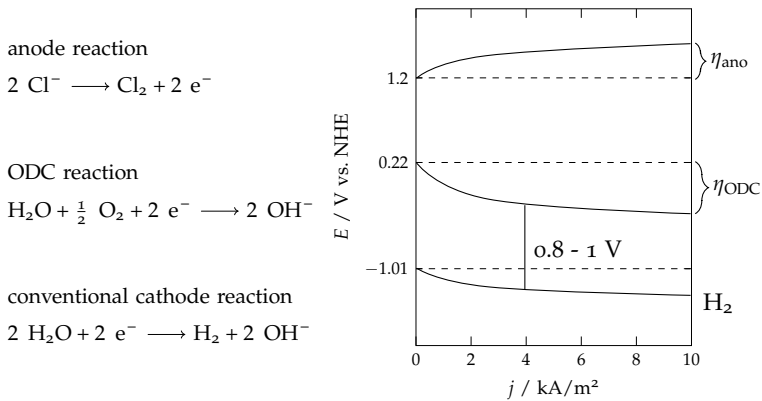
Figure 1.4: Comparison of half-cell electrode overpotential of conventional and ODC based cell (standard potential at 90 °C [16])

least electricity consuming process therefore, chlorine producers in Europe are switching to this technology. Comparison of above discussed three types of cells is given in tables 1.2 and 1.3.

Hydrogen produced in this process can be utilized for the power generation by combustion process, thereby, increases cell economy. Alternatively, it also can be used in the fuel cell but, capital investment for this is high. Instead ODC used in the chlor-alkali cell avoid hydrogen production and reduces 30% of electricity demand [13]. Energy and economical saving due ODC surpasses the hydrogen utilization savings [14]. An electricity price rise in the near future is eminent and hence the economic benefits of ODC based technology will further increase [14]. Concept of using ODC in chlor-alkali cell is explained in next section. Membrane cells with hydrogen evolution reaction is referred to as *conventional cell*—in further discussion.

8

Table 1.2: Comparison of three chlor-alkali cells [15, 6]

	Unit	Diaphragm	Amalgam	Membrane
Typical cell voltage	V	-3.44	-4.44	-3.0
Typical current density	kA/m^2	2.3	10	4
Cl$_2$ purity	%	96.5-98	98-99	97-99.5
O$_2$ in Cl$_2$	%	0.5-2	0.1-0.3	0.5-2.0
H$_2$ purity	%	>99.9	>99.9	>99.9
NaOH concentration before evaporation	%	12	50	35
Cl$^-$ in 50% NaOH	%	0.025-1.0	0.005	0.005
Brine purity requirement		high	low	very high
NaOH production rate per cell	t/year	1000	5000	100
Electricity demand	kWh/t$_{Cl_2}$	2300-2900	3100-3400	2100-2600
Total energy demand for 50% NaOH, O$_2$-free Cl$_2$	kWh/t$_{Cl_2}$	3200-3800	3100-3400	2400-2900
Environmental issues		asbestos for diaphragm	Hg used as cathode material	none

Table 1.3: Advantages and disadvantages of the three types of cells [15]

Cell	Advantages	Disadvantages
Diaphragm	Low purity brine can be used Low specific energy requirement	Require asbestos diaphragm High steam requirement for concentrating NaOH Sensitive to pressure fluctuations Low purity of chlorine
Amalgam	50% NaOH can be produced directly from cell High purity of chlorine and hydrogen recycling of brine is simple	Require Hg High quality brine is required Highest operational cost High space requirement Grater risk for environment
Membrane	Low specific energy requirement Less capital investment Cost effective cell operation High purity of NaOH Tolerate process fluctuations Further improvement is possible	Highest purity of brine is required Highest O_2 concentration in chlorine High membrane cost
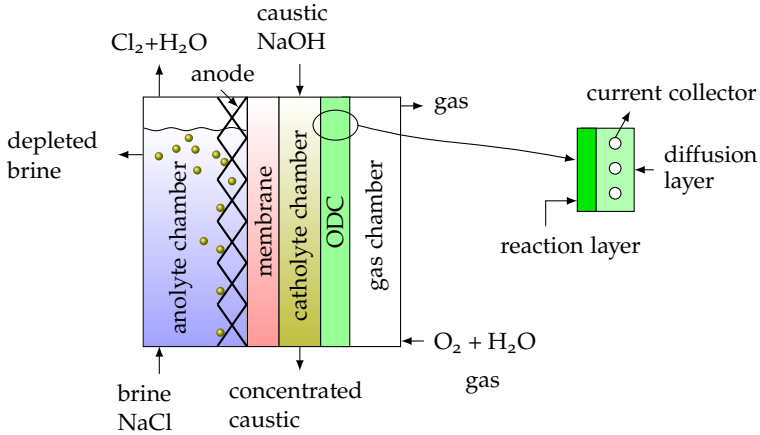
Figure 1.5: Schematic diagram of ODC based membrane cell (not to scale)

1.1.4 *Membrane cell with oxygen depolarized cathode*

From above discussion we learned that, the membrane cell is the most promising technology; it has fewer environmental impacts and low on the energy demand. Further reduction in electricity demand is possible by changing the cathode reaction. Oxygen Reduction Reaction (ORR) depolarizes cathode by suppressing the hydrogen evolution reaction. Figure 1.4 shows that, the difference in equilibrium potential decrease by 1.23 V and a gain of 0.8 V to 1 V can be reached at industrially relevant current densities.

In practice, it is known that gas diffusion electrode facilitate ORR, for example in fuel cell. Depolarizing gas diffusion electrode in chlor-alkali cell is called as Oxygen Depolarized Cathode (ODC). Total reaction of NaCl electrolyzer based on Oxygen Depolarized Cathode (NaCl-ODC) is given as follows,

$$\text{total reaction:} \quad 2\,NaCl + H_2O + \frac{1}{2}O_2 \longrightarrow Cl_2 + 2\,NaOH \quad \text{(R 1.7)}$$
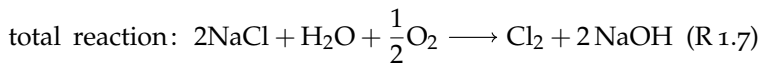
ODC reaction shown in fig. 1.4 indicates that, ODC requires liquid water, gaseous oxygen and electrons from solid phase. There-

fore, ODC should be a porous electrode and the cathode compartment has to be split in two chambers, one each for caustic solution and oxygen gas. Figure 1.5 shows the falling-film configuration of ODC based cell. Some other cell configurations are available for example, zero-gap technology, in which catholyte chamber is eliminated. It offers two benefits og having simpler design and diminishing the ohmic losses of the catholyte chamber. Some other designs for NaCl-ODC technology are discussed in detail by Moussallem et al. [13] and Jörissen et al. [8].

Gas diffusion electrode in chlor-alkali cell should facilitate intimate contact of gaseous oxygen, liquid water and electrons from solid state. Figure 1.6 shows that, the O_2 gas dissolves in the electrolyte and then, reacts with electrons and liquid water to form hydroxyl ions. Established three phase (gas, solid and liquid) boundary in gas diffusion electrodes should meet following requirements [13],

- Chemically stable in alkaline solution at temperature from 80 °C to 90 °C.

- High mechanical stability in technical electrolyzer with area of 2.72 m^2.

- High electronic conductivity and low thickness.

- High activity and surface area of electrocatalyst.

- Appropriate hydrophobic/hydrophilic pore structure for easy access of gases and liquid. Such a structure avoids the breakthrough of gas in catholyte chamber and the flooding of the electrode.

- Stable performance even in pressure fluctuations.

- Long-term operational life and consistent performance.

- Low cost material

Spray method can be used for manufacturing Gas Diffusion Electrode (GDE) and process for which is depicted in fig. 1.7. Suspension of silver powder (catalyst), PTFE solution, water(solvent)
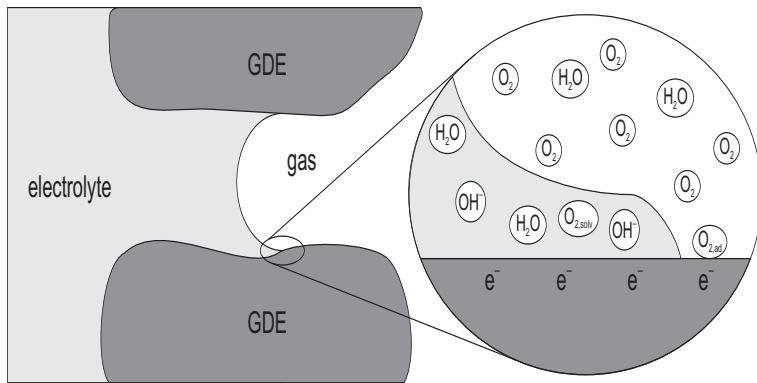
Figure 1.6: Illustration of three phase boundary in pore structure of the ODC (reproduced with publisher's permission [13])
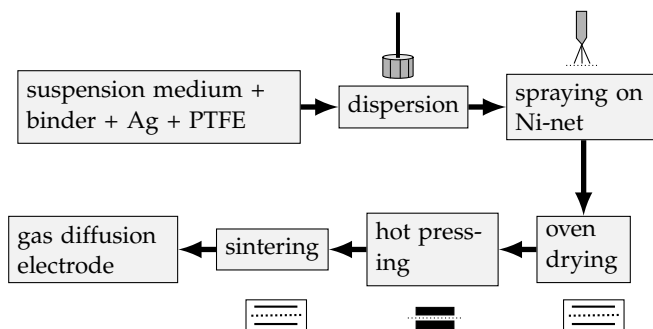
Figure 1.7: Illustration of gas diffusion electrode manufacturing process

and methyl-cellulose (binder) is prepared. Hydrophobic/hydrophilic nature of electrode is controlled by the Polytetrafluoroethylene (PTFE) content. Methyl-cellulose also acts as thickening agent so that the heavy Ag powder does not settle immediately. This suspension is repeatedly sprayed over the Ni-net until the desired thickness is achieved. Ni-net acts as a current distributor in the electrode as well as offers mechanical stability to the electrode. Later, the finished electrode dries in oven and is subsequently hot pressed to establish intimate contact between the catalyst particles. Sintering is the final step in the production process. In this process, methyl cellulose is burned out and creates pores in the electrode to offer the passage to the gas as well as electrolyte. Detailed description of manufacturing process is given in [17].

The idea of using ODC in the chlor-alkali cell is over 50 years old. Many companies tried to develop this technology since 1980s. Summary of all research programs and their outcomes are discussed in detail by Moussallem et al. [13]. In 2006, BMS started a joint research program to commercialize NaCl-ODC technology, in cooperation with several industries and universities. Clausthal University of Technology was one project partners of this program and current dissertation is one of the outcomes of the project. Project was funded by BMBF, see details in www.klimazwei.de. Important outcome of this project is that "A demonstration plant using this process (NaCl-ODC cell) started operations at the Krefeld-Uerdingen site in mid-2011." [18]. Today, this technology is exclusively marketed by, ThyssenKrupp Industrial Solutions and UH-DENORA. Important features of the commercial electrolyzer are given in table 1.4.

1.2 OBJECTIVE OF THE DISSERTATION

From previous sections, it is well understood that, the chlor-alkali process is an energy intensive one. Over the years, several ideas were implemented to overcome environmental and economical impact of this process. Even though, ODC based chlor-alkali cell seems to be a promising solution. It has always been difficult to commercialize the NaCl-ODC technology. The Gas Diffusion Electrode (GDE) is the key component of the process as it brings

Table 1.4: Important features of NaCl-ODC cell [13, 17, 19, 20]

	Unit	Value
Typical current density	kA/m^2	4
Typical cell voltage	V	2 - 2.2
Cl_2 purity	% (m^3/m^3)	>98
O_2 in Cl_2	% (m^3/m^3)	0.5 - 1
NaOH concentration before evaporation	% (kg/kg)	32
NaCl in NaOH	ppm	<60
O_2 consumption with O_2 recycling	Nm^3/mt_{Cl_2}	183
Power consumption	kWh/mt_{NaOH}	1400
Cell temperature	°C	82-90
Active area per element	m^2	2.72
Height of the electrode	m	>1
ODC life	years	4
ODC electrocatalyst		Silver

all the three reacting phases in intimate contact for the ORR. Failure of the electrode will result in cell voltage increase, subsequently resulting in evolution of hydrogen. Apart from this, electro-catalysts are expensive and hence the understanding of physical and chemical process taking place in the pores of ODC is essential for optimizing of the electrodes. To address these issues, Pinnow et al. [21] developed a steady state model and predicted the performance of the cell. This model was validated using laboratory scale electrode.

On the operational side, the concern remains that of how electrode will perform in a technical electrolyzer? Industrial scale electrodes have large of about 2.7 m^2 and height of over 1 m (see table 1.4). Owing to this, uniform current density distribution is of utmost important for the following reasons,

- Proper utilization of electro-catalyst

- Longer operational life of ODC

- To avoid side reactions e. g. hydrogen peroxide

- High current efficiency

- Increase of production per unit electrode area

Until now, there have been no attempt made to determine current and overpotential distribution of the industrial scale electrode—either theoretically or experimentally. Similarly, there is a lack of discussion, on heat balance of industrial scale NaCl-ODC electrolyzer.

Objective of this dissertation is to predict the ODC performance in industrial electrolyzer. Under this framework temperature, current, and overpotential distribution of the industrial scale ODC is predicated. Rectified three phase current is required for the industrial electrolyzer. Therefore, effect of ripple (unwanted residual periodic variation of the Direct Current (DC)) on the performance of electrode is also predicted in this work. To achieve the aforementioned objective following research work is undertaken,

STEADY STATE MODELLING

Height dependent model (section 3.2) predict the magnitude of heat and it's distribution in industrial scale electrolyzer. It also estimates the mass balance of electrolyzer, along the height. Previously developed Thin-Film Flooded Agglomerate (TFFA) model [21] (along thickness) and height dependent model solved together to predict current density and overpotential distribution of the ODC. This array of calculation is denoted as 1D+1D approach (section 3.3).

DYNAMIC MODELLING

To predict the effect of ripple on the performance of the electrode, a dynamic model has been developed (chapter 4). To validate dynamic model CI (section 6.2) experimental data has been used.

As explained above, this work gives an existing opportunity to enhance our understanding of industrial scale ODC. Due to constrains of availability of data and computational complexity, certain assumptions were made and discussed in detail during the course of discussion.

*"Whenever a theory appears to you as the only possible one,
take this as a sign that you have neither understood the
theory nor the problem which it was intended to solve."*
— *Karl Popper*

2

THERMODYNAMICS AND HEAT BALANCE

Previous chapter explained that the chlor-alkali process is energy intensive in terms of electricity requirement. However, only some of the provided electrical energy is used for the reaction in electrolysis while unused part is converted into heat. To estimate this heat generation it is essential to understand the thermodynamics of the process. This chapter explains the heat balance and associated thermodynamics of the electrochemical reactor.

2.1 GIBBS FREE ENERGY AND ELECTRICAL WORK

The Gibbs free energy of a reaction provides the information about the maximum work done in a thermodynamic system. To understand it better let's consider a galvanic cell producing electricity. The obvious question would be how much is the maximum electrical work done by this cell? We know that in a reversible process work done is maximum. Gibbs free energy of the reaction gives the information about maximum electrical work. Mathematically it can be express as below,

$$\Delta G = -E\,n\,F \tag{2.1}$$

where, ΔG is the change in Gibbs free energy, E is the reversible potential, n is the number of electrons in half-cell reaction, and F is the Faraday's constant. Since reversible process are always in a state of equilibrium therefore, reversible potential is also called as equilibrium potential/voltage. Reverse case of galvanic cell is electrolytic cell. In this cell, electric work is required due to the non-spontaneity of the reaction. In this case the question is how

much minimum electrical work is required to progress the reaction in the desired direction? Again answer is, Gibbs free energy at constant temperature and pressure. So far, we understood the relation between E of the cell and Gibbs free energy of the reaction. Similarly, other thermodynamic quantities can be derived from reversible potential. From Gibbs-Helmholtz relation,

$$\Delta S = -\left(\frac{\partial \Delta G}{\partial T}\right)_P \tag{2.2}$$

where T is the temperature and S is the entropy. From eq. (2.1) and eq. (2.2)

$$\Delta S = n F \left(\frac{\partial E}{\partial T}\right)_P \tag{2.3}$$

and

$$\Delta H = \Delta G + T \Delta S = n F \left[\left(T\frac{\partial E}{\partial T}\right)_P - E\right] \tag{2.4}$$

where H is the enthalpy of the reaction.

2.2 HEAT PRODUCTION IN ELECTROCHEMICAL CELL

Industrial cell voltage is much higher than the reversible potential. Total cell voltage can be further split in to the following forms,

$$U_{cell} = E + \sum R + \sum \eta \tag{2.5}$$

where, U_{cell} is the total cell voltage, R is the cell resistance, and η is the overpotential. The last two terms at the right hand side of eq. (2.5) contribute to the irreversible heat and is called Joule heat.

$$Q_{\text{Joule,T}} = -n F \left(\sum R + \sum \eta\right) \tag{2.6}$$

where, Q is the heat in J/mol and subscripts 'Joule' and 'T' indicate Joule heat and total respectively. The total heat produced
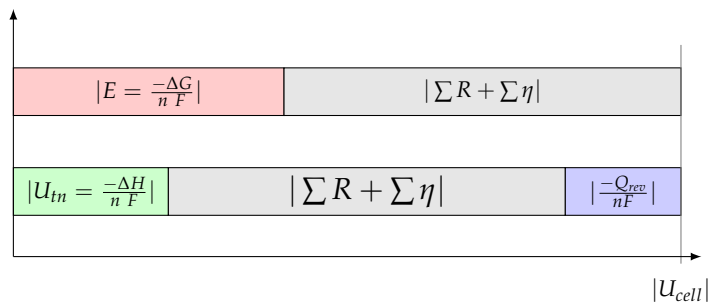
Figure 2.1: Illustration of thermodynamic of heat production in electrolytic cell

in the cell shouldn't be necessarily equal to Joule heat because entropy may contribute the reversible heat (Q_{rev}),

$$Q_{rev} = T\Delta S \tag{2.7}$$

where, subscript 'rev' indicate reversible. Negative value of Q_{rev} indicates that the entropy is reduced during the reaction, hence heat is released. The opposite case is the positive value where the heat is absorbed. Reversible heat will be either evolved or absorbed, depending on the thermo-neutral cell voltage (U_{tn}),

$$U_{tn} = -\frac{\Delta H}{n\,F} \tag{2.8}$$

Enthalpy of the reaction and it's relation to reversible heat is explained in the fig. 2.1. In this figure, first y-axis bar from the top, shows the total cell voltage divided into reversible potential and summation of ohmic losses and overpotential. Consider $U_{tn} < E$ for same cell (see second y-axis bar from top); it doesn't contribute to heat production. Summation of U_{tn} and $|\sum R + \sum \eta|$ is less than U_{cell}. Thus, remainder of electrical energy will produce heat. This heat is produced due to entropy of the reaction, hence called as reversible heat. With this analogy, when, $U_{tn} > E$ reversible heat will be absorbed from surrounding and for $U_{tn} = E$ reversible heat will be zero. From this understanding, following

Table 2.1: Comparison of heat produced in conventional and ODC based chlor-alkali electrolysis at 4 kA/m²

Cell	U_{cell} [*]	U_{tn} [†]	Q_{irr}	$\frac{Q_{irr}}{nFU_{cell}}$	Q_{rev}
	V	V	kJ/mol	%	kJ/mol
conventional	3.0 [‡]	2.27	140.9	24.3	20.1
NaCl-ODC	2.2 [§]	0.80	270.2	63.6	-36.7

equation can be written to determine total irreversible heat produced in electrolysis cell.

$$Q_{irr} = -n F \left(U_{cell} - U_{tn} \right) \tag{2.9}$$

Subscript 'irr' denotes irreversible. Alternatively, following equation can be written,

$$Q_{irr} = Q_{Joule,T} + Q_{rev} \tag{2.10}$$

From the above discussion, we understood how to calculate the magnitude of the heat source or heat sink. Based on the above understandings, we can compare the heat produced in the conventional chlor-alkali cell and NaCl-ODC cell. Table 2.1 shows the comparison of heat produced in conventional and NaCl-ODC cell. This comparison is based on industrial operational conditions and parameters. The most important revelation from this table is the percentage of the amount of heat produced for same operating conditions. For example, NaCl-ODC cell produces heat of upto 63.6% of total electricity input, while for the conventional cell this is 24.3%. It is interesting point out the large difference despite the anode reaction for both the cell types being the same. This difference can be explained by the vaöues of U_{tn} and Q_{rev}. In a conventional chlor-alkali cells the heat is absorbed from the immediate surrounding due to the increase of the entropy. This

---

[*] positive sign convention is taken for electrolytic cell
[†] from [22] at 90 °C
[‡] from [15]
[§] from [20]

accounts for positive value of Q_{rev}. Contrary to this in an ODC based cell heat is released due to decrease of the entropy.

2.3 HALF CELL REACTION THERMODYNAMICS

From the above discussions it can be well understood that in conventional chlor-alkali cells reversible heat is absorbed from the surrounding and is reverse for NaCl-ODC cell. However, total reaction entropy doesn't provide information of half cell reaction entropy. Uniform heat distribution on electrode ensures high current efficiency. In worst cases, poor heat management can damage membrane. Therefore, it is necessary to calculate the individual half cell reaction entropy.

In this work, method of thermal coefficients by deBethune et al. [23], Salvi and deBethune [24] is used. It calculates half-cell reversible potential as function of temperature. Later the entropy is calculated by Gibbs-Helmholtz equation (eq. (2.3)).

The heat produced in an electrode is caused by the overpotential and through entropy effects. The reversible heat produced by the entropy can be calculated by the Gibbs–Helmholtz equation,

$$Q_{rev}(T) = T\,\Delta S(T) = TnF\,\frac{\mathrm{d}E(T)}{\mathrm{d}T}. \tag{2.11}$$

The half-cell equilibrium potential as function of temperature can be calculated by the method of thermal coefficients [23, 24], assuming unit activity of the species

$$E(T) = E^{\ominus} + (T - T^{\ominus})\frac{\mathrm{d}E^{\ominus}}{\mathrm{d}T} + \frac{(T - T^{\ominus})^2}{2}\frac{\mathrm{d}^2 E^{\ominus}}{\mathrm{d}T^2}. \tag{2.12}$$

Here, $E^{\ominus}$ is the equilibrium potential at standard conditions. The first temperature coefficient in the above equation is,

$$\frac{\mathrm{d}E^{\ominus}}{\mathrm{d}T} = \frac{\Delta H}{nFT} + \frac{E^{\ominus}}{T}, \tag{2.13}$$

where ΔH is the enthalpy change during the reaction at temperature T. The second temperature coefficient can be calculated with the following equation [24]

$$\frac{\mathrm{d}^2 E^{\ominus}}{\mathrm{d}T^2} = \frac{\Delta C_p^{\ominus}}{nFT},$$ (2.14)

where $\Delta C_p^{\ominus}$ is the change of the molar specific heat capacities at standard conditions during the reaction. Data for molar specific heat capacity and heat of formation is taken from [25].

Figure 2.2 compares reversible heat of ODC and conventional cell's half-cell reaction, at 363 K [I]. The anode reaction is the same in both the cells and is endothermic. Similarly, cathode reaction's reversible heat in both the cell is exothermic. However, ODC reaction is more exothermic than conventional reaction. Therefore, reversible heat of overall reaction in ODC based cell is exothermic, while it is endothermic in conventional cell.

Jörissen et al. [8] showed that ODC is the highest contributor to the overpotential at industrially relevant current density. ODC overpotential contribute to Joule heat and in addition, reversible heat is also produced. Thus, ODC is highest contributor of heat production. Therefore, appropriate heat removal measures are necessary, to avoid damage to the membrane due to heat generation as well as to obtain uniform temperature distribution. Heat management becomes even more crucial in zero gap arrangement of the cell in which the ODC and the membrane are in close contact.

2.4 HEAT BALANCE OF ELECTROLYSIS CELL

Normally, the industrial electrolysis process operates at higher temperature (chlor-alkali at 88-90 °C) [20] and hence making heat transfer very crucial. Non-uniform heat distribution could burn out the membrane and isothermal operation may not occur. Proper heat management of Joule heating can reduce the usage of external heat used for electrolytes preheating. It can also be utilized to increase the rate of mass transfer and the reaction rate.

¶ Specific heat and heat of formation data is taken from ref. [25]
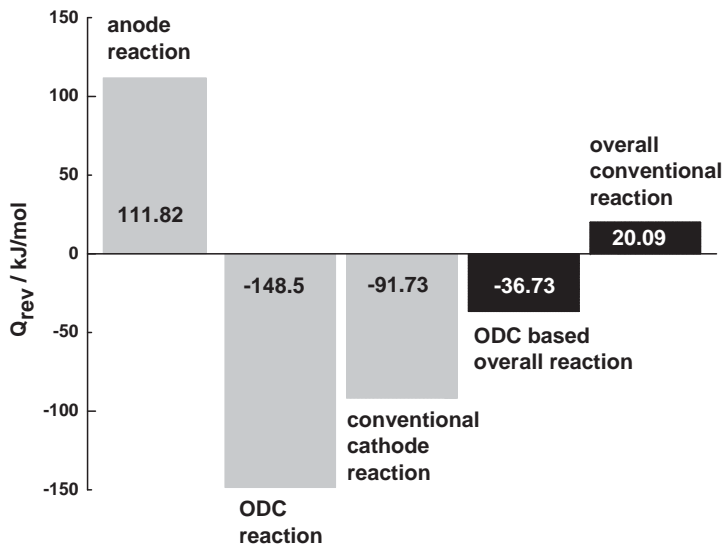
Figure 2.2: Reversible heat of half cell reaction and overall reaction for ODC based cell and conventional cell at 363 K
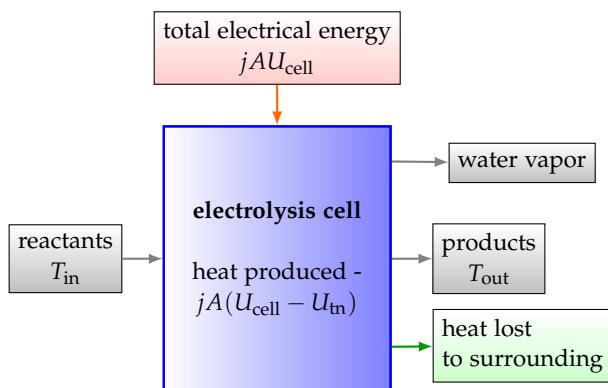
Figure 2.3: Illustration of heat transfer of steady-state-continuous electrochemical reactor

These pros and cons compel us to understand the process of heat transfer in electrolysis cell. So far, we understood the method of calculating the magnitude of heat production. However, the process of heat transfer is equally important.

Figure 2.3 shows, an illustration of the continuous electrochemical reactor and heat flow. In any electrolysis cell total electrical energy applied is expressed as below,

$$\text{total electrical work applied} = j \, A \, U_{\text{cell}} \quad (2.15)$$

where j is the current density and A is the area of the electrode. Only some part of the applied electrical energy is required for the formation of the product i.e. ΔH, remainder converts into the heat. Reactants streams enter into the cell at temperature T_{in}, and acts as heat-exchanging medium. Heat production in the cell increases the temperature of these reactant streams and leaves the cell at T_{out}. It leads to a change in the enthalpy of these streams. At the same time, gaseous streams that get saturated with water vapor also require heat. In addition to this the outer surface of the cell transfers heat to the surrounding by convection and radiation. At steady state, the heat produced in the cell is equal to the flowing steams' enthalpy change and heat loss. It can be mathematically expressed as follows,

$$\dot{q}_{\text{T}} = \sum_j \dot{m}_{j,\text{out}} c_{P,j,\text{out}} (T_{j,\text{out}} - T^{\ominus})$$
$$- \sum_j \dot{m}_{j,\text{in}} c_{p,j,\text{in}} (T_{j,\text{in}} - T^{\ominus}) + \dot{q}_\lambda + \dot{q}_{\text{loss}} \quad (2.16)$$

where, $\dot{m}$ is the mass flow rate of stream and $\dot{q}$ is the heat flow rate in W. Subscript in, out, λ, and loss refer to inlet, outlet, phase change, and loss to the surrounding respectively. The first term at the right side of equality calculates the summation of the enthalpy change of the outlet streams from the datum temperature ($T^{\ominus} = 298K$). The second term, calculates the summation of the enthalpy change of the inlet stream from the datum temperature. While the third term is the heat consumed by evaporated water flowing along with the gases. The last term is the heat lost from the surface of the cell by radiation and convection.

MODELING

What is research, but a blind date with knowledge.
— William Henry

3

STEADY STATE MODELLING

A porous electrode or GDE plays an important role in electro-chemical applications such as in various types of fuel cells, batteries, and electrolysis cells. Porous electrode provides a large interface area compared to its superficial area. This distinctive feature provides a high reaction rate at lower overpotential. It also enables passage for gaseous reactants to reach the reaction sites and thereby facilitates a three phase contact of gas, liquid and solid, which is important to avoid poor performance of the electrode.

GDE modeling can play a vital role for revealing physical and chemical phenomena taking place in the GDE at microscopic and macroscopic levels. Its performance can be predicted in connection with decisive structural, transport and kinetic parameters of the electrode reaction. Thus, insights provided by modeling results, may help in planning critical experiments or operational optimization. Well planned experiments always save time as well as expensive resources. In some cases, conducting experiments could be costly thus, modeling may serve as an economical alternative. It is a proven tool for structural optimization of GDEs used in fuel cells. ODC is also a GDE therefore, modeling might serve our objectives as well.

MODELING METHODOLOGIES

Today, GDEs are modeled extensively for fuel cell and battery technologies. A detailed review of the fuel cell models is presented by Weber and Newman [27]. Overall aim of the study dictates the approach of the modeling. To start with a favorable geometry of the GDE is required to be chosen. Later the equa-

gas phase

solid phase

1: electrolyte side
2: gas side

electrolyte (solid or liquid)
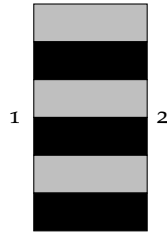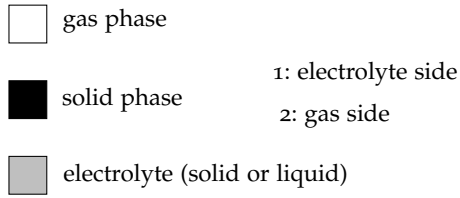
(A) cylinder pore model
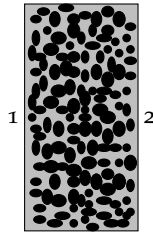
(B) homogeneous model
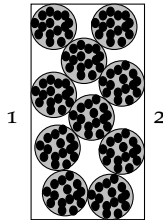
(C) spherical agglomerate model

Figure 3.1: Various geometry used for modeling gas diffusion electrode [26]

tions or complex expressions related to mass transports, charge transport and electrochemical reactions are required. Sometimes, energy and momentum balance of each component is incorporated. These types of the models are often complex because the dependent variables are coupled with nonlinear equations.

Simplest form of the models are the empirical models [28, 29, 30, 31]. These models describe the polarization curve (current-voltage relationship), a typical expression for these types of model is given as follows,

$$U_{\text{cell}} = E + \sum R + \sum \eta \qquad (3.1)$$

These models are easy to evaluate and compare experimental data. Other complex models can further be classified as microscopic, macroscopic and quantum levels. Microscopic models focus at individual pore level while in macroscopic models the catalyst is assumed to form a certain ordered geometry. All phases exists uniformly in the volume and constitutes variables like porosity and surface area per unit volume. Quantum models investigate the reaction mechanism and elementary transfer reaction.

Most widely used geometries to model gas diffusion electrode are shown in figs. 3.1 and 3.2. Perhaps the first model consists of a single cylindrical gas pore, developed by Euler and Nonnenmacher [32]. Later Austin et al. [33], Grens and Tobias [34] assumed that the pore is flooded with electrolyte (fig. 3.1 (A)). In a cylindrical pore model or flooded pore model the solid catalyst exhibit cylindrical shape and pores are filled with electrolyte phase [35, 36]. Electrolyte phase carry the ions and reactants. Electrons flow only in the solid phase and reactions takes place at the liquid-solid interphase . Cutlip [37] considered a thin film of electrolyte over the agglomerate and presented the so called Thin-Film Flooded Agglomerate (TFFA) model (see fig. 3.2). Homogeneous models (fig. 3.1 (B)) consider the catalyst particle as continuously distributed in the electrode and pores are filled with the electrolyte. Effective ionic and electronic conductivity is used, based on the porosity of the electrode instead of pure state property. These types of the model are one dimensional as the catalyst particles are much smaller than the thickness of the electrode. Based on homogeneous geometry a seminal paper presented by
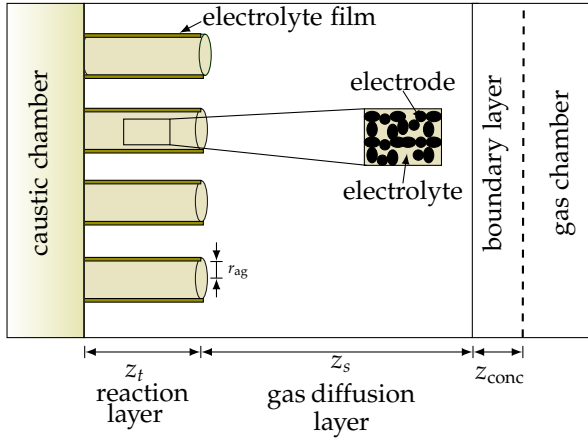
Figure 3.2: Thin-Film Flooded Agglomerate (TFFA) geometry of the model [45]

Springer et al. [38] on modeling of GDE for polymer-electrolyte fuel cell. This model predicts the performance of the fuel cell. Later, several groups [39, 40, 41] modeled gas diffusion electrodes based on this geometry. Spherical agglomerate geometry (fig. 3.1 (C)) was also used to model gas diffusion electrodes [42, 43, 44]. In these types of models, agglomerates are assumed to be of same size and shape. Catalyst particles are covered with the electrolyte film and reactant diffuses through this film. In this work a TFFA geometry has been used to model the ODC.

3.1 THIN-FILM FLOODED AGGLOMERATE MODEL

Figure 3.2 explains the TFFA geometry. It assumes that, ODC is made of cylindrical agglomerates and its void are flooded with electrolyte (caustic solution) in Reaction Layer (RL). In the same layer, a thin film of electrolyte covers the agglomerate. A Gas Diffusion Layer (GDL) gives the passage to the oxygen for reaching up to the reaction sites in the RL. Figure 3.3 shows the scanning-electron-micrograph of an electrode produced by spray method on Ni-net. The electrodes produced have a typical thickness of
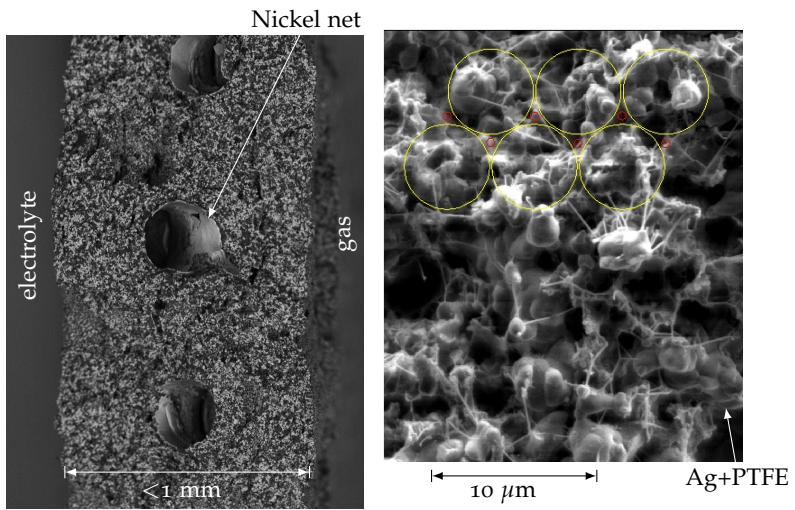
Figure 3.3: Schematic representation of the model in real electrode [16]

less than 1 mm. The real pore structure of an electrode can be seen in the right side of fig. 3.3. Silver catalyst particles can be seen surrounded by PTFE fibers. The drawn small and large circles represent a typical distribution of the corresponding gas and liquid filled regions in the reaction layer of the electrode, adopted from the model. To model the ODC of chlor-alkali cell, Wang and Koda [46, 47] used the TFFA geometry. These models were isothermal and take into account the structural parameters of the electrode such as thickness, porosity etc. They predicted the performance of the electrode at various current density. Pinnow [16] extended the Wang and Koda [46, 47] model by using generalized Maxwell-Stefan equation to describe the mass transfer of the multi-component system in gas and liquid phase. Electrochemical reaction described by the Tafel reaction and two Tafel slopes were used to validate the model. In this dissertation, to model 1D+1D (height + thickness), Pinnow [16] model is used along the thickness. Some of the parameters are made as function of temperatures as discussed in section 3.1.2. Important assumptions of the TFFA model with relevance to this work are summarized in the following section

3.1.1 *Model assumptions*

All the assumptions considered in the previous model [21, 16] are valid for ODC, except of being isothermal. In this work, transport parameters and solubility of oxygen in caustic solution are described as function of temperature. Additionally the boundary layer thickness is changed, due to cell's industrial scale dimensions. Structural parameters of the electrode remains the same. The model assumptions are listed below:

1. Tafel slope and exchange current density are independent of the temperature. This is justified by the fact that only small temperature gradients occur in the ODC, as will be demonstrated later.

2. The thickness of the solid phase components is much smaller than the height. Therefore, along the thickness (z) uniform

temperature is assumed. Addition of temperature dependent parameters are useful for the 1D+1D model (section 3.2).

3. The silver electrical conductivity is very high and therefore, assumed independent of temperature.

4. Thickness of concentration and thermal boundary layer are equal (see section 3.2.7).

5. Concentration and thermal boundary layer are fully developed. Linear temperature distribution is assumed in the thermal boundary layer.

3.1.2 *Temperature dependent parameters*

This section describes the TFFA model modifications to solve temperature dependent behavior of the ODC.

Ionic conductivity

The ionic conductivity of caustic solution as a function of temperature and concentration is based on data from BMS,

$$\frac{\kappa_{\text{caustic}}}{\text{S/m}} = 1.729 \left(\frac{T}{\text{°C}}\right) - 99.89 \left(\frac{w_{\text{caustic}}}{\text{kg}_{\text{NaOH}}/\text{kg}_{\text{caustic}}}\right) - 3.794 \quad (3.2)$$

where κ_{caustic} is the ionic conductivity of the caustic solution and w is the mass fraction. Subscript caustic denotes caustic solution or related to caustic chamber. Equation 3.2 is valid for $0.294 < w_{\text{caustic}} < 0.322$ and $70\text{°C} < T < 95\text{°C}$. Comparison of the results obtained with the correlation and experimental data are shown in fig. 3.4.

Diffusivity of O₂ in caustic solution

Diffusivity of oxygen ($D^l_{O_2}$) in NaOH solution as a function of temperature is calculated by using Stokes-Einstein equation.

$$D^l_{O_2} = \frac{D^l_{O_2,\text{ref}}\mu_{\text{ref}}}{\mu(T)} \left(\frac{T}{T_{\text{ref}}}\right) \quad (3.3)$$
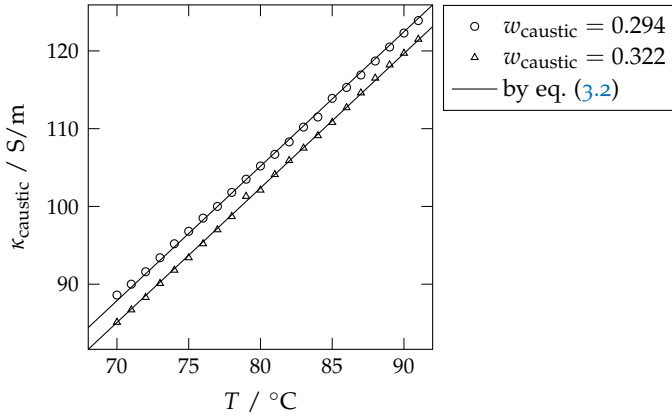
Figure 3.4: Comparison of experimental data with values obtained from eq. (3.2)

In the above equation μ is the dynamic viscosity and subscript ref is used for reference condition at which diffusivity is known for a given temperature. Reference values in Stokes-Einstein equation are taken from [48, 49] at 80 °C.

Henry constant of O_2 in caustic solution

Henry constant (*He*) for oxygen in NaOH solution as a function of temperature is calculated by using Van't Hoff equation. Reference values for this equation are taken from [48] at 80 °C.

$$He(T) = He_{ref} \cdot exp\left(-C_H\left[\frac{1}{T} - \frac{1}{T_{ref}}\right]\right) \tag{3.4}$$

where C_H is the constant, related to heat of dissolution of oxygen in caustic solution.

Thermal conductivity of ODC

The ODC is made from Silver, PTFE and as current distributor Ni net. Therefore, the thermal conductivity of the solid part (K_{sd}) is mass averaged and calculated using the following equation,

$$K_{sd} = (w_{Ni} \cdot K_{Ni}) + (w_{Ag} \cdot K_{Ag}) + (w_{PTFE} \cdot K_{PTFE}) \tag{3.5}$$

33
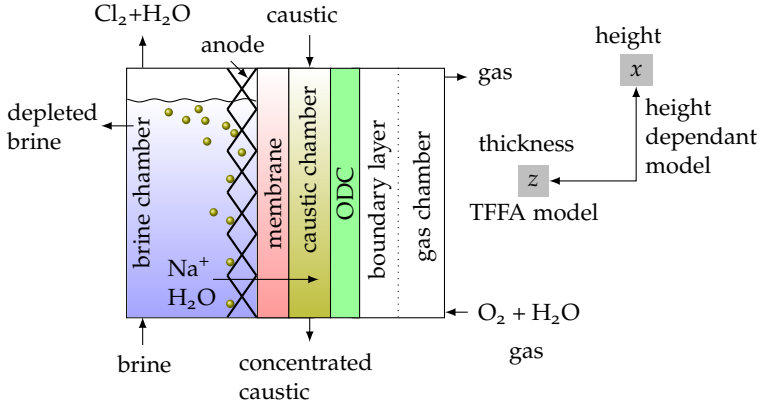
Figure 3.5: Schematic diagram of falling-film NaCl-ODC cell and domains of the model (not to scale)

where K is the thermal conductivity of the subscripted species and w is the mass fraction. Subscript PTFE denotes Polytetrafluoroethylene; it's thermal conductivity is taken from [50] at 100 °C. Thermal conductivity of metal as a function of temperature is determined by using correlation given in [51]. Effective thermal conductivity (K_{eff}) of the porous electrode can be calculated by Bruggeman's relation of approximation [52]. Thermal conductivity of the gas and caustic solution is much less than that of the metal and hence neglected in following equation [53],

$$K_{eff} = (1 - \epsilon_s)^{1.5} K_{sd}. \tag{3.6}$$

Here, ϵ_s is the porosity of the GDL and $(1 - \epsilon_s)$ is the volume fraction of the solid in the ODC.

3.2 HEIGHT DEPENDENT MODEL

Figure 3.5 shows a schematic diagram of the falling-film configuration of a NaCl-ODC electrolyzer. It also explains the model region and the length domain. The height dependent model determines the temperature distribution of electrolyzer components

such as anode, membrane, and ODC as well as the electrolyte streams (brine, caustic, and gas). It also calculates the electrolyte's mass balance. It should be noted that, brine and caustic flow are counter-current and same for caustic and gas flow. In this model heat sources are the reversible heat at cathode and the Joule heat due to ohmic losses. Heat sinks are reversible heat at the anode, water evaporation and the cold electrolyte streams coming inside the electrolyzer. Important assumption are summarized in the following section

3.2.1 *Model assumptions*

1. Since the production of chlorine gas in the brine chamber creates considerable turbulence, it is assumed that the brine flow is ideally mixed. This assumption is backed by Chandran and Chin [54], who also considered the brine chamber in their study as Continuous Stirred-Tank Reactor (CSTR).

2. For the caustic solution flowing from the electrolyzer top, plug flow is assumed.

3. For simplification, gas flow is also treated as ideal plug flow.

4. Water flowing through the membrane along with Na^+ ions is in thermal equilibrium with the membrane.

5. Temperature gradients in z-direction are neglected, because the thickness of the solid phase components is much smaller than their height.

6. Chlorine gas evolving in the brine chamber is saturated with water vapor.

7. Dissolution of chlorine in the brine is neglected.

8. No side reactions occur, therefore the current efficiency is assumed to be one hundred percent.

9. The electrolyzer is assumed to be adiabatic. Hence, heat losses to the surroundings are neglected.

10. The pressure drop along the height of the cell is not considered.

3.2.2 *Brine chamber*

The stoichiometry of the anode reaction is

$$2\,Na^+ + 2\,Cl^- \longrightarrow 2\,Na^+ + Cl_2 + 2\,e-. \tag{R 3.1}$$
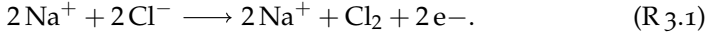
While chlorine ions are oxidized to produce Cl_2 and electrons, Na^+ ions cross the membrane to reach the caustic chamber (see fig. 3.5). The electrons flow through the external circuit toward the ODC. Taking into account the stoichiometry of the overall ODC reaction (R 1.7), the rate of NaCl consumption during the electrolysis process can be calculated with Faraday's law

$$R_{NaCl} = \frac{j_{avg}\,A\,M_{NaCl}}{F}, \tag{3.7}$$

where F is the Faraday constant, M_{NaCl} the molar mass of sodium chloride and j_{avg} is the average current density. As per assumption 1, the brine flow profile is perfectly back-mixed. Thus, this compartment can be treated as CSTR for mass and energy balance and the outlet mass flow rate, $\dot{m}_i$ of species i is calculated with the following equation,

$$\dot{m}_{i,out} = \dot{m}_{i,in} + R_i. \tag{3.8}$$

Equations 3.7 and 3.8 can be used to calculate the mass flow rate of Cl_2 leaving the brine chamber

$$\dot{m}_{Cl_2,out} = \frac{j_{avg}\,A\,M_{Cl_2}}{F}. \tag{3.9}$$

Together with sodium ions, a certain amount of water flows from the brine chamber to the caustic chamber through the membrane (see fig. 3.6). The corresponding mass flow rate is

$$\dot{m}_{H_2O_{(l)},mem} = n_d\,\frac{j_{avg}\,A\,M_{H_2O}}{F}, \tag{3.10}$$

where n_d is the number of moles of water flowing per mole of Na^+ ion. The produced chlorine gas flow is saturated with water vapor thus yielding the following water mass flow

$$\dot{m}_{H_2O_{(g)},out,brine} = \frac{M_{H_2O}}{M_{Cl_2}} \cdot \frac{P^{sat}_{H_2O_{(g)},out,brine} \cdot \dot{m}_{Cl_2,out}}{(P_{T,brine} - P^{sat}_{H_2O_{(g)},out})}. \tag{3.11}$$

Here, P_T is the total pressure and $P^{sat}_{H_2O_{(g)}}$ the water saturation pressure above the brine solution, which is obtained from [55]. With

$$\dot{m}_{H_2O_{(l)},out,brine} = \dot{m}_{brine,in} - \dot{m}_{NaCl,in,brine}$$
$$- \dot{m}_{H_2O_{(l)},mem} - \dot{m}_{H_2O_{(g)},out,brine} \tag{3.12}$$

the flow rate of liquid water and

$$\dot{m}_{brine,out} = \dot{m}_{NaCl,in,brine} - R_{NaCl} + \dot{m}_{H_2O_{(l)},out,brine}. \tag{3.13}$$

the flow rate of the brine at the outlet of brine chamber are calculated. The anode is perforated (see figure fig. 3.6) so that Na^+ ions can pass to the caustic chamber through the membrane. The ohmic loss (φ) in the brine solution due to the flow of these ions is calculated with

$$\varphi_{brine} = (1 - \epsilon_{ano}) \frac{j_{avg}}{\kappa_{brine}} d_{ano}, \tag{3.14}$$

where ϵ_{ano} is the area fraction of the anode which is in contact with the membrane, d_{ano} is the anode thickness and κ_{brine} is the ionic conductivity of the brine, which is estimated by Kubasov's theory [56]. The Ohmic loss in the brine produces Joule heat, which is calculated as follows

$$\dot{Q}_{brine} = j_{avg} b \varphi_{brine}, \tag{3.15}$$

where $\dot{Q}$ is the heat gradient in W/m and b is the width of the electrode. Fig. 3.6 shows that, due to the perforation of the anode, brine is in contact with the membrane and $\dot{Q}_{ano}$ and $\dot{Q}_{mem}$ are
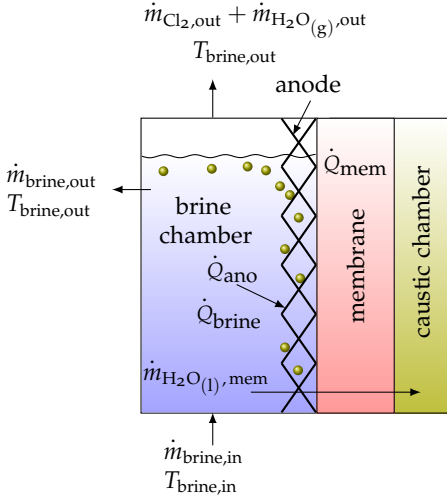
Figure 3.6: Illustration of mass flows and location of heat sources/sinks associated with the brine chamber [45]

the heat sources at anode and membrane, respectively. Hence, the respective heat flows are proportional to the corresponding contact areas. Some of the heat is used to saturate chlorine gas with water vapor, while the enthalpy change of water flowing through the membrane is also considered. Finally, the steady state energy balance for this cell compartment is as follows,

$$\dot{Q}_{\text{brine}} h + \epsilon_{\text{ano}} \alpha_{\text{brine}} A (T_{\text{ano,avg}} - T_{\text{brine,out}}) + (1 - \epsilon_{\text{ano}}) \alpha_{\text{brine}}$$
$$A (T_{\text{mem,avg}} - T_{\text{brine,out}}) + \dot{m}_{\text{brine,in}} c_{p,\text{brine,in}} (T_{\text{brine,in}} - T^{\ominus}) =$$
$$\dot{m}_{\text{H}_2\text{O}_{(g)},\text{out,brine}} \left[H_{\text{wg}}(T_{\text{brine,out}}) - H_{\text{wl}}(T_{\text{brine,in}}) \right] + \dot{m}_{\text{H}_2\text{O}_{(l)},\text{mem}}$$
$$\left[H_{\text{wl}}(T_{\text{brine,out}}) - H_{\text{wl}}(T_{\text{brine,in}}) \right] + \left[\dot{m}_{\text{Cl}_2} c_{p,\text{Cl}_2} + \dot{m}_{\text{brine,out}} \right.$$
$$\left. c_{p,\text{brine,out}} \right] (T_{\text{brine,out}} - T^{\ominus}), \quad (3.16)$$

Here, h is the height of the electrode and α is the heat transfer coefficient. For determination of the heat transfer coefficient, chlorine bubble diameter and gas velocity are required [57, 58]. However, this data is unavailable for the chosen configuration

and operating conditions. Therefore, the overall enthalpy balance
(see section 5.3) and the height dependent model had to be solved
simultaneously to determine the required values for $T_{\text{brine,out}}$ and
α_{brine}. Data for chlorine and brine specific heat capacity is taken
from [59]. H_{wg} and H_{wl} are the specific enthalpy of water in
gaseous and liquid phase respectively. For the description of en-
thalpy of water as function of temperature, a correlation from
[60] was employed.

3.2.3 Anode

The anode overpotential is calculated with the following Tafel
relationship,

$$\eta_{\text{ano}} = T_{\text{s,ano}} \cdot \log \left(\frac{j_{\text{avg}}}{j_{0,\text{ano}}} \right), \tag{3.17}$$

where η is the overpotential, T_s is the Tafel slope and j_0 is the
exchange current density. Finally, the total heat flow produced at
the anode $\dot{Q}_{\text{ano}}$ taking into account reversible and Joule heat is
obtained from

$$\dot{Q}_{\text{ano}} = j_{\text{avg}} \, b \left(\frac{-Q_{\text{rev,ano}}(T)}{nF} \right) + j_{\text{avg}} \, b \, \eta_{\text{ano}}. \tag{3.18}$$

Since the anode receives additional heat from the hot membrane
surface, the overall heat balance is given by the following equa-
tion

$$\epsilon_{\text{ano}} \, A \, K_{\text{ano}} \frac{\mathrm{d}^2 T_{\text{ano}}(x)}{\mathrm{d}x^2} = \epsilon_{\text{ano}} \, \alpha_{\text{brine}} \, b \, (T_{\text{ano}}(x) - T_{\text{brine,out}})$$
$$- \dot{Q}_{\text{ano}} - \epsilon_{\text{ano}} \, b \, \frac{(T_{\text{mem}}(x) - T_{\text{ano}}(x))}{R_{\text{th}}}. \tag{3.19}$$

Here, K_{ano} is the thermal conductivity of the anode material (ti-
tanium), the values of which are calculated using a correlation
from [51]. R_{th} is the thermal contact resistance between mem-
brane and anode, which was considered as a fitting parameter. It
was varied until the temperature difference between the anode
and the membrane at the bottom of the cell became less than

1K. However, this assumption is arbitrary, it was made to allow for the development of different temperatures in the two solids, membrane and anode. If this contact resistance is neglected the two components would attain the same temperature.

3.2.4 *Membrane*

In the membrane Na^+ ions are transported from the brine to the caustic chamber. During this ionic transport, additional water molecules are dragged. The resulting mass flux of water through the membrane can be calculated as follows

$$\frac{d\dot{m}_{H_2O_{(l)},mem}(x)}{dx} = \frac{n_d \, j(x) \, b \, M_{H_2O}}{F}. \tag{3.20}$$

This water also takes up heat from the membrane (see assumption 4). The membrane potential as function of temperature and current density for a Flemion® membrane was calculated using data by Jörissen et al. [61].

$$\frac{\varphi_{mem}(x)}{mV} = 5.326 \times 10^{-11} \left(\frac{j(x)}{kA/m^2}\right)^2 - 2.4 \left(\frac{j(x)}{kA/m^2} \cdot \frac{T}{°C}\right) \tag{3.21}$$

$$+0.267 \left(\frac{T}{°C}\right)^2 + 260.8 \left(\frac{j(x)}{kA/m^2}\right) - 39.37 \left(\frac{T}{°C}\right) + 1462.4 \tag{3.22}$$

Comparison of experimental potential of membrane (F-8020 SP) with values obtained by eq. (3.21) is shown in fig. 3.7. The corresponding heat source is the ohmic loss within the membrane and is represented by,

$$\dot{Q}_{mem}(x) = j(x) \, b \, \varphi_{mem}(x). \tag{3.23}$$
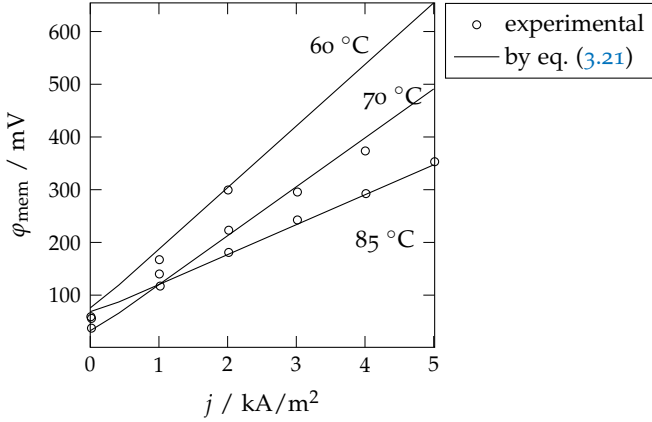
Figure 3.7: Comparison of experimental potential of membrane (F-8020 SP) with values obtained by eq. (3.21)

On the other hand, anode and brine solution are heat sinks for the membrane resulting in the following overall energy balance

$$
\begin{aligned}
AK_{\text{mem}} \frac{\mathrm{d}^2 T_{\text{mem}}(x)}{\mathrm{d}x^2} &= \alpha_{\text{caustic}}\, b\, (T_{\text{mem}}(x) - T_{\text{caustic}}(x)) \\
&- \dot{Q}_{\text{mem}}(x) + (1 - \epsilon_{\text{ano}})\, \alpha_{\text{brine}}\, b\, (T_{\text{mem}}(x) - T_{\text{brine,out}}) + \epsilon_{\text{ano}}\, b \\
&\frac{(T_{\text{mem}}(x) - T_{\text{ano}}(x))}{R_{\text{th}}} + \frac{\mathrm{d}\dot{m}_{\text{H}_2\text{O}_{(l)},\text{mem}}(x)}{\mathrm{d}x} \\
&[H_{\text{wl}}(T_{\text{mem}}(x)) - H_{\text{wl}}(T_{\text{brine,out}})].
\end{aligned} \tag{3.24}
$$

Since thermal conductivity data for the Flemion® membrane is unavailable, thermal conductivity of a Nafion® membrane has been used. This assumption appears to be valid since both types of membranes are chemically very similar to tetrafluoroethylene based fluoropolymers.

3.2.5 *Caustic chamber*

In the caustic chamber, caustic solution flows under plug flow condition is as per assumption 2 and the according mass and
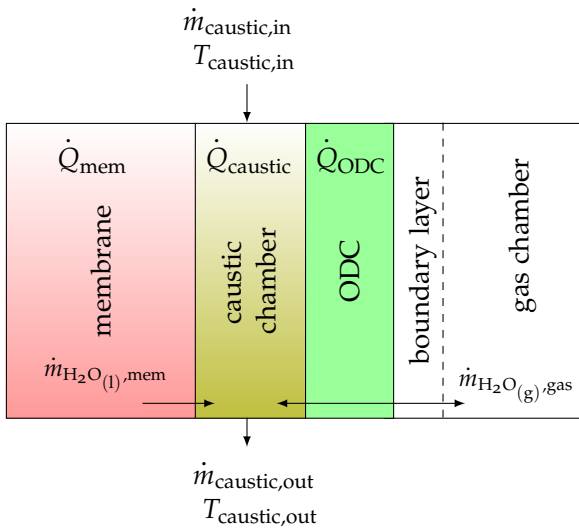
Figure 3.8: Illustration of mass flows and location of heat sources/sinks associated with the caustic chamber [45]

energy balances had to be used. The rate of production and consumption is given by the following differential equation

$$\frac{dR_i(x)}{dx} = \frac{\nu_i \, j(x) \, b \, M_i}{n \, F}.$$ (3.25)

Oxygen comes in contact with caustic solution through the porous part of the ODC while water from the caustic solution evaporates to saturate oxygen in the gas chamber (see fig. 3.8). Details of the calculation of water evaporation are given in section 3.2.7. The water balance in the caustic chamber as a function of height is expressed using the following equation,

$$\dot{m}_{H_2O_{(l)},\text{caustic}}(x) = R_{H_2O_{(l)}}(x) + \dot{m}_{H_2O_{(l)},\text{mem}}(x)$$
$$- \dot{m}_{H_2O_{(g)},\text{gas}}(x). \quad (3.26)$$

The flow rate of caustic as function of height is given by,

$$\dot{m}_{\text{caustic}}(x) = \dot{m}_{H_2O_{(l)},\text{caustic}}(x) + R_{\text{NaOH}}(x).$$ (3.27)

The mass fraction of the caustic is calculated by the following equation.

$$w_{\text{caustic}}(x) = \frac{R_{\text{NaOH}}(x)}{\dot{m}_{\text{caustic}}(x)}.$$ (3.28)

The ohmic loss in the caustic chamber is obtained with

$$\varphi_{\text{caustic}}(x) = \frac{j(x)}{\kappa_{\text{caustic}}(T)} \, d_{\text{caustic}},$$ (3.29)

where d_{caustic} is the thickness of caustic chamber and κ_{caustic} is the ionic conductivity. The heat gradient in the caustic solution caused by the ohmic losses is

$$\dot{Q}_{\text{caustic}}(x) = j(x) \, b \, \varphi_{\text{caustic}}(x).$$ (3.30)

Furthermore, the caustic solution receives heat from the ODC, while the addition of water coming along with Na^+ through the

membrane also causes an enthalpy change. The resulting energy balance for the caustic compartment can be described with

$$\dot{m}_{\text{caustic}}(x)\, c_{p,\text{caustic}}(x)\, \frac{dT_{\text{caustic}}(x)}{dx} = \alpha_{\text{caustic}}\, b\, (T_{\text{mem}}(x)$$
$$- T_{\text{caustic}}(x)) + \dot{Q}_{\text{caustic}}(x) + \alpha_{\text{caustic}}\, b\, (T_{\text{ODC}}(x) - T_{\text{caustic}}(x))$$
$$+ R_{\text{NaOH}}(x)\, \Delta H_{\text{dil}}(T_{\text{caustic}}). \quad (3.31)$$

Here, $\Delta H_{\text{dil}}(T)$ is the enthalpy change due to dilution, which is calculated with a correlation from [49]. The specific heat capacity for the caustic solution is taken from [59].

3.2.6   *Oxygen Depolarized Cathode (ODC)*

In the porous ODC liquid water reacts with oxygen to produce hydroxyl ions according to the following stoichiometric equation,

$$\frac{1}{2}\; O_2 + H_2O + 2\; e^- \longrightarrow 2\; OH^- \qquad (R\,3.2)$$
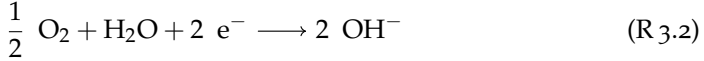
These hydroxyl ions and Na^+ ions coming from the membrane finally produce $NaOH_{(aq)}$ inside the caustic chamber. The TFFA model developed by Pinnow et al. [21] is used. However, some of the added temperature dependencies are discussed in section 3.1. Uniform temperature is assumed along the thickness (z-coordinate) of an ODC but not along the height (x-coordinate). The heat gradient along the height of the ODC taking into account the overpotential and the reversible heat is given by

$$\dot{Q}_{\text{ODC}}(x) = j(x)\, b\, \eta_{\text{ODC}} + j(x)\, b\left(\frac{-Q_{\text{rev}}(T)}{nF}\right). \qquad (3.32)$$

This heat produced in the ODC is transferred to the caustic solution and the gas mixture. A portion of the heat is used to evap-

orate water, which flows along with the oxygen gas. The final energy balance can be described by the following equation:

$$A K_{\text{eff}} \frac{\mathrm{d}^2 T_{\text{ODC}(x)}}{\mathrm{d}x^2} = \alpha_{\text{caustic}} \, b \left(T_{\text{ODC}}(x) - T_{\text{caustic}}(x) \right) - \dot{Q}_{\text{ODC}}(x)$$

$$+ \alpha_{\text{gas}} \, b \left(T_{\text{ODC}}(x) - T_{\text{gas}}(x) \right) + \frac{\mathrm{d}\dot{m}_{\text{H}_2\text{O}_{(l)},\text{gas}}(x)}{\mathrm{d}x} \left[H_{\text{wg}}(T_{\text{ODC}}(x)) \right.$$

$$\left. - H_{\text{wl}}(T_{\text{caustic}}(x)) \right]. \quad (3.33)$$

3.2.7 *Gas chamber*

Figure 3.5 shows how the mixture of oxygen and water vapor enters the gas chamber, where oxygen diffuses through the concentration boundary layer to the ODC. On the other hand, a thermal boundary layer develops in the gas chamber due to the temperature difference between ODC and bulk gas stream, which also might have an effect on the mass transport in concentration boundary layer. The thermal boundary layer thickness (δ_{thermal}) is calculated using the following equation

$$\delta_{\text{thermal}} = \frac{\alpha_{\text{gas}}}{K_{\text{gas}}}, \quad (3.34)$$

while the thickness of the concentration boundary layer (δ_{conc}) is obtained from the Lewis number

$$Le^{1/3} = \frac{\delta_{\text{thermal}}}{\delta_{\text{conc}}}. \quad (3.35)$$

As the resulting thickness ratio amounts to 1.03 for the given conditions, we assumed that concentration and thermal boundary layer have the same thickness (assumption 4). In the thermal boundary layer, a linear temperature profile ranging from the ODC temperature to the bulk gas temperature was assumed (c.f. eq. (3.40)).

The conversion of O_2 under the assumed plug flow condition is described by

$$\frac{\mathrm{d}R_{\text{O}_2}(x)}{\mathrm{d}x} = \frac{j(x) \, b \, M_{\text{O}_2}}{4F}. \quad (3.36)$$
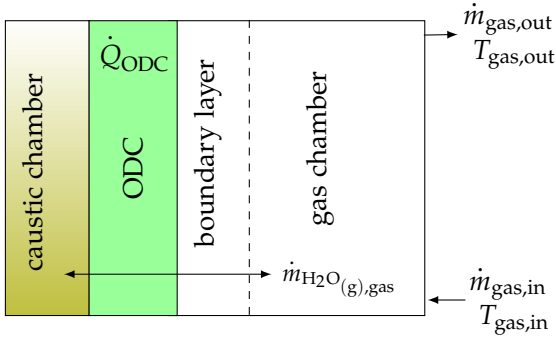
Figure 3.9: Illustration of mass flows and location of heat sources/sinks associated with the gas chamber [45]

Figure 3.9 shows that water vapour enters the gas chamber through the ODC while additional water is transported along with the gas stream. The resulting water balance can be expressed with

$$\frac{d\dot{m}_{H_2O_{(g)},gas}(x)}{dx} = -b\, N_{H_2O}(x) M_{H_2O},$$ (3.37)

where $N_{H_2O}(x)$ is the molar water vapor flux at the interface of gas chamber and boundary layer (for details see Pinnow et al. [21]). The flow rate of the complete gas mixture along the height can be calculated with

$$\dot{m}_{gas}(x) = \dot{m}_{H_2O_{(g)},gas}(x) + R_{O_2}(x).$$ (3.38)

The partial pressure of species i in the gas chamber is calculated using the following equation

$$P_{i,gas}(x) = \frac{P_{T,gas}\, \dot{m}_{i,gas}(x)}{M_i \sum_j \dot{m}_{i,gas}(x)/M_i}$$ (3.39)

where subscript j denotes the various species in the gas chamber. Since ODC is the only heat source for the gas mixture, the temperature distribution along the electrolyzer height can be calculated as follows

$$\dot{m}_{gas}(x) c_{p,gas}(x) \frac{dT_{gas}(x)}{dx} = \alpha_{gas} b (T_{ODC}(x) - T_{gas}(x)),$$ (3.40)

46

where the specific heat capacity of the gas mixture $c_{p,\text{gas}}$ is calculated with Aspen Properties® software.

3.3 1D+1D APPROACH

The TFFA model has a fixed water and oxygen boundary concentration however, along the height of the electrolyzer, temperature and concentration changes. Thus, the TFFA model has to account for the changes in boundary conditions along the height. The height dependent model (section 3.2) provides boundary conditions to the TFFA model (section 3.1); these models are iterated to determine either the current density distribution or the overpotential distribution. Such solution approach is called as 1D+1D or pseudo-2-D model. Previously several researcher [62, 63, 64, 65] used such 1D+1D models for fuel cell. A major drawback of 1D+1D approach is—it can not calculate current and overpotential distribution simultaneously. Nevertheless, proper discretization of a 1D+1D model reflects the result of full 2D model [27].

Previously Šimek and Roušar [66] developed a two-dimensional model to determine the primary (in the absence of overpotentials) and secondary (taking into account activation overpotentials) current density distribution in an amalgam cell. Their analysis revealed that the secondary current density distribution is more uniform than the primary current density distribution at the cathode. White et al. [67] determined the three-dimensional current density distribution for bipolar conventional electrolysis. The obtained results showed that the primary current density distribution is uniform in the electrodes due to their high conductivity. Byren et al. [68] predicted primary, secondary, and pseudo-tertiary current density distributions of a conventional chlor-alkali cell. None of these models, however, were applied to a chlor-alkali cell with ODC. This dissertation is a first attempt to determine the current and overpotential distribution in a NaCl-ODC electrolyzer.

The configuration of the cell and the flow directions are shown in fig. 3.5. This model accounts the mass transport in z and x direction, whereas heat transport is calculated in x-direction only.

Aspen Custom Modeler® V7.3 is used, to solve model equations simultaneously. Structural and kinetic parameters of the ODC are the same as given in Table 1 and Table 2 of [21] nevertheless, some important parameters are summarized in table 3.1. Other important parameters used for the simulation are given in table 3.2 and table 3.3. Algorithms to calculate current density and overpotential distribution along the height are explained as follows,

Solution technique (1)

Objective of this technique is to determine current density distribution, assuming a constant overpotential in the ODC. A calculation algorithm is shown in fig. 3.10 (see page 52). Microsoft Excel VBA (Visual Basic for Applications) is used to do iterations.

Solution technique (2)

This technique determines ODC's overpotential distribution, assuming a constant current density in the ODC. The simulation by this technique determines a current density distribution. It takes the initial value of η_{ODC} from the solution technique -1. A calculation algorithm is shown in fig. 3.11 (see page 53).

3.4 TOTAL CELL VOLTAGE

Once the solution is achieved either by solution technique (1) or solution technique (2), the total cell voltage can be calculated.

for solution technique (1)

ODC's overpotential is constant along the height for solution technique (1) and the total cell voltage (U_{cell}) is calculated by following equation,

$$U_{cell}(x) = E(x) + \eta_{ano} + \varphi_{brine}(x) + \varphi_{mem}(x) + \varphi_{caustic}(x) + \eta_{ODC} \quad (3.41)$$

Table 3.1: Important structural parameters of the electrode (for detail see [21])

Name	Symbol	Unit	Value
Gas diffusion layer			
thickness	z_s	m	1.0×10^{-4}
Porosity	ϵ_s	m^3/m^3	0.4
Averaged radius of the gas channel	r_s	m	5.0×10^{-7}
Reaction layer			
thickness	z_t	m	2.0×10^{-4}
Porosity	ϵ_t	m^3/m^3	0.32
Averaged radius of the gas channel	r_t	m	2.5×10^{-7}
Averaged radius of the agglomerate	r_{ag}	m	5.0×10^{-6}
thickness of the film	δ_{tf}	m	6.0×10^{-8}
Total thickness of the electrode	$z_s + z_t$	m	3.0×10^{-4}

Table 3.2: Important parameters used for base case simulation

Name	Symbol	Unit	Value	Remark
Pressure at brine chamber	$P_{T,1}$	bar	1.2	Industrial value from [69]
Heat transfer coefficient in brine chamber	α_1	$W/m^2 \cdot K$	350	own estimate
Thickness of anode	d_{ano}	mm	1	own estimate
Tafel slope of anode	T_s	V	0.038	0.25 kg_{NaCl}/kg_{brine} NaCl solution at 95°C [70]
Exchange current density of anode	i_s	A/m^2	12.5	0.25 kg_{NaCl}/kg_{brine} NaCl solution at 95°C [70]
Contact resistance in membrane and anode	R_{th}	$m^2 \cdot K/W$	0.002621	fitting parameter, see section 3.2.4
Electro-osmotic drag coefficient	n_d	mol/mol	4	[71]
Thermal conductivity of Nafion® membrane	K_{mem}	$W/m \cdot K$	0.29	65°C fully humidified [72], see also section 3.2.4

Table 3.3: Important parameters used for base case simulation

| Name	Symbol	Unit	Value	Remark
Thickness of caustic chamber	d_2	mm	1	[13]
Heat transfer coefficient in caustic chamber	α_2	$W/m^2 \cdot K$	2733	own estimate
Area of ODC	A	m^2	2.7	[13]
Height of ODC	h	m	1.3	[13, 20]
Width of ODC	b	m	2.077	calculated from the value of A and h
Tafel slope of ODC	$T_{s,ODC}$	V/decade	0.20	from [21]
Constant used in eq. (3.4)	C_H	K	1800	[73]
Heat transfer coefficient in Gas chamber	α_3	W/m^2K	2.01	own estimate
Concentration and thermal boundary layer thickness	δ_{conc} $\delta_{thermal}$	mm	13	by using eq. (3.34) and equation eq. (3.35), see also assumption no. 4
Pressure in Gas chamber	$P_{T,gas}$	bar	1.1234	from [21]
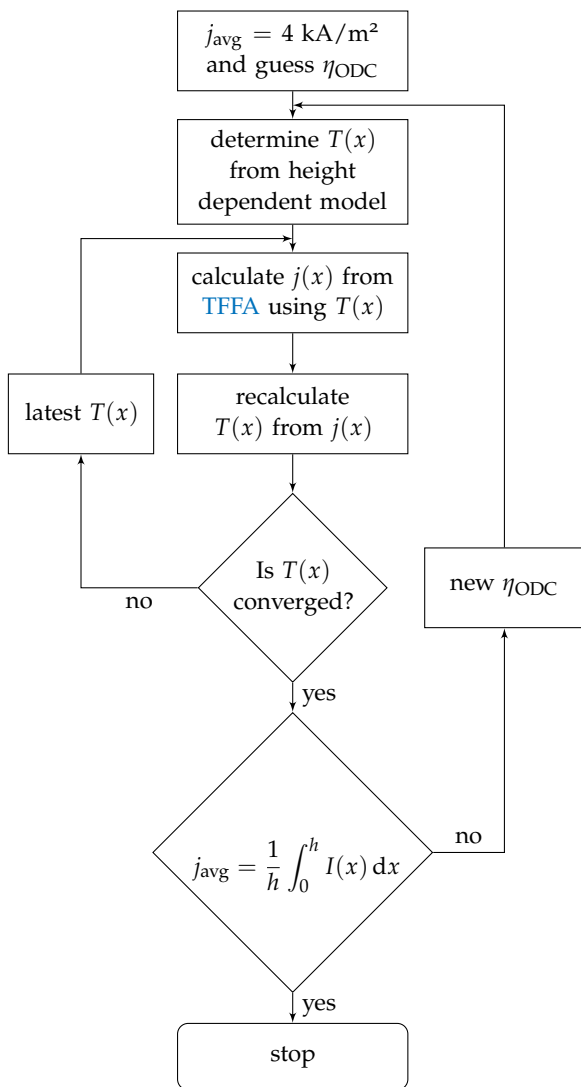
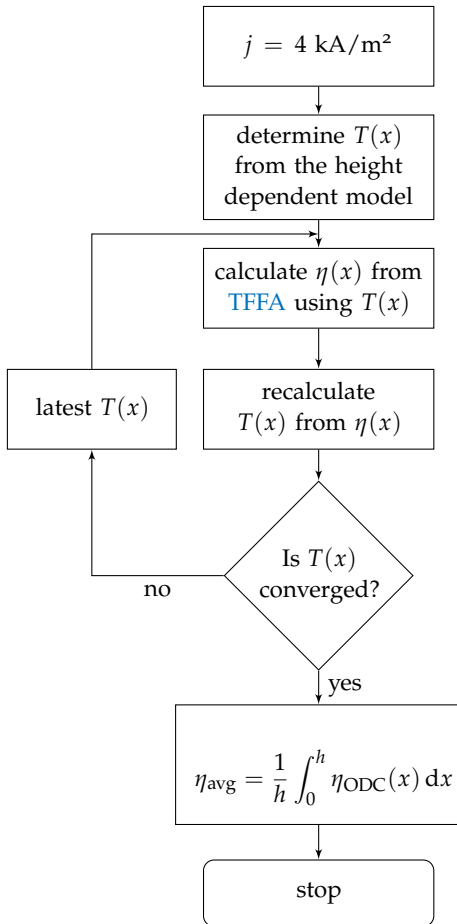Figure 3.10: Algorithm to determine current density distribution of ODC [45]

Figure 3.11: Algorithm to determine overpotential distribution of
ODC [45]

53

for solution technique (2)

ODC's overpotential is a function of height for solution technique (2) and the total cell voltage is calculated by the following equation,

$$U_{\text{cell}}(x) = E(x) + \eta_{\text{ano}} + \varphi_{\text{brine}}(x) + \varphi_{\text{mem}}(x) + \varphi_{\text{caustic}}(x) + \eta_{\text{ODC}}(x) \quad (3.42)$$

3.5 BOUNDARY CONDITIONS

For the energy balance of the solid compartments two boundary conditions at the top ($x = h$) and the bottom ($x = 0$) of the electrolyzer are required, which are summarized in the following equations.

ODC energy balance, $x = h$:

$$A \, K_{\text{eff}} \frac{\mathrm{d}T_{\text{ODC}}}{\mathrm{d}x} = \dot{m}_{\text{caustic}} \, c_{p,\text{caustic}} (T_{\text{ODC}} - T_{\text{caustic}})$$
$$+ \dot{m}_{\text{gas}} \, c_{p,\text{gas}} (T_{\text{ODC}} - T_{\text{gas}}) \quad (3.43)$$

Membrane energy balance, $x = h$:

$$A \, K_{\text{mem}} \frac{\mathrm{d}T_{\text{mem}}}{\mathrm{d}x} = \dot{m}_{\text{caustic}} \, c_{p,\text{caustic}} (T_{\text{mem}} - T_{\text{caustic}})$$
$$+ \dot{m}_{\text{brine}} \, c_{p,\text{brine}} (T_{\text{mem}} - T_{\text{brine}}) \quad (3.44)$$

Anode energy balance, $x = h$:

$$\epsilon_{\text{ano}} \, A \, K_{\text{ano}} \frac{\mathrm{d}T_{\text{ano}}}{\mathrm{d}x} = \dot{m}_{\text{brine,avg}} \, c_{p,\text{brine}} (T_{\text{ano}} - T_{\text{brine}})$$
$$+ \epsilon_{\text{ano}} \, b \, \frac{(T_{\text{mem}} - T_{\text{ano}})}{R_{\text{th}}} \quad (3.45)$$

As the electrolyzer is assumed to be adiabatic (assumption 9), the following boundary conditions at the bottom ($x = 0$) apply

$$\frac{\mathrm{d}T_{\text{ODC}}}{\mathrm{d}x} = 0, \quad \frac{\mathrm{d}T_{\text{mem}}}{\mathrm{d}x} = 0, \quad \text{and} \quad \frac{\mathrm{d}T_{\text{ano}}}{\mathrm{d}x} = 0.$$

Table 3.4: Electrolyte streams inlet parameters

Stream	Flow rate	Concentration	Temperature
Brine	237.6 kg/h	0.25 kg_{NaCl}/kg_{brine}	60 °C
caustic	453.6 kg/h	0.30 $kg_{NaOH}/kg_{caustic}$	71 °C
Gas	8.22 kg/h	0.025 mol_{H_2O}/mol_{gas}	20 °C

Electrolytes' mass and energy balance equations require inlet flow rates and temperatures respectively as their boundary conditions. These boundary conditions are given in table 3.4. The oxygen flow at the entrance of the electrolyzer is 1.27 times higher than the stoichiometric requirement. This slight excess was chosen to maintain a sufficient oxygen supply even at the end of the gas chamber.

The most beautiful thing we can experience is the
mysteries. It is the source of all true art and science.
— Albert Einstein

4

DYNAMIC MODEL

Previous chapter explained the steady state model for a industrial scale NaCl-ODC electrolyzer—aimed to determine temperature, current, and overpotential distribution. However, these results consider that the current flowing through the electrolyzer is DC. In practice, three phase Alternating Current (AC) is obtained from the power plant and therefore the rectifier is used to obtain DC. However, incomplete suppression of the components of harmonics results in ripple. It has the small undesirable residual harmonic variation in the DC. Ripple is responsible for reduction of current efficiency [74]. In this chapter a dynamic model will be developed to predict the effect of ripple current on the performance of the ODC.

AC current tends to concentrate near the surface of the conductor, which increases the resistivity and this phenomenon is called skin effect. Increased resistivity due to the skin effect results in unnecessary heat production. Apart from that, ripple current also reduces process equipment life, creates disturbance in process instrumentation, electromagnetic coupling with nearby structures. These are some additional undesirable effects. Ripple current varies with time, therefore it is necessary to develop a dynamic model to understand its effect on the performance of the ODC. To simulate TFFA model under dynamic condition, double layer current need to be added. For the ease in computation, previously developed model by Pinnow et al. [21] is simplified.

4.1 THREE PHASE DIODE BRIDGE RECTIFIER

In industry, three phase current is required due to a high power requirement of electrolytic cells operating in stack. To produce

(a) Three phase diode bridge rectifier with electrolysis cell

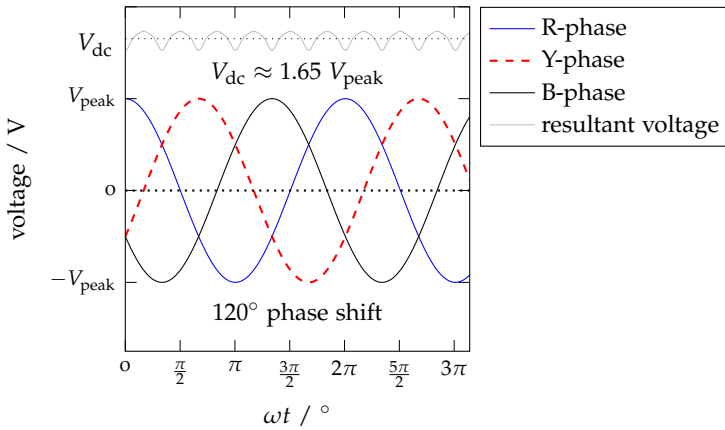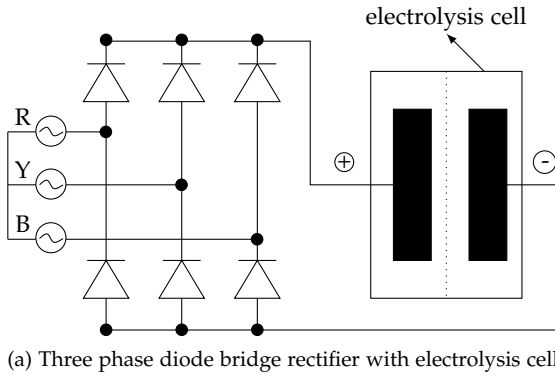(b) Wave for of input voltage and output DC voltage

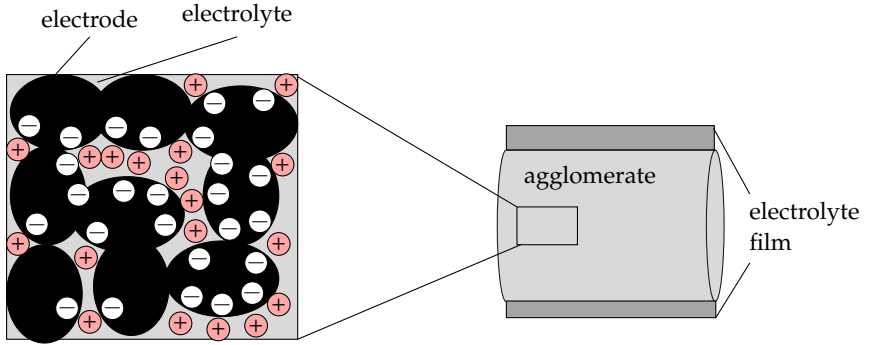Figure 4.1: Principle of working of a three phase bridge rectifier

Figure 4.2: Illustration of electrochemical double layer

DC, a three phase diode rectifier is required as shown in fig. 4.1(a). The rectifier is supplied by a balanced three-phase voltage with a phase shift of 120°, shown in fig. 4.1(b). The diodes conduct only in positive direction thus producing constant voltage (V_{DC}). Three phase diode bridge rectifier is a full wave rectifier and the voltage responsible for the direct current is given by [75],

$$V_{DC} \approx 1.65 V_{peak}, \tag{4.1}$$

where, V_{peak} is the peak voltage in the three phase. The output DC voltage wave is shown in fig. 4.1(b); it is calculated by the following Fourier series [75],

$$V_r = \frac{3\sqrt{3}V_{peak}}{\pi}\left(1 - \sum_{k=1}^{+\infty} \frac{2}{36k^2-1}cos(6k\omega t)\right), \tag{4.2}$$

Here, V_r is the output ripple voltage from the rectifier, ω is the angular frequency and t is the time.

4.2 DYNAMIC MODEL

An important difference in steady and dynamic state models is that accumulation term in the dynamic model is not zero. In any electrochemical system ions get accumulated, at the interface of

the electrode and electrolyte (see fig. 4.2). Accumulation of ions creates electrochemical capacitance. Under unsteady state condition double layer current flows due to ions accumulation. Therefore, it is necessary to include double layer current [43], to predict unsteady state behavior.

4.3 MODEL ASSUMPTION

This model is based on our previous steady state model [21, 16]. For ease in calculations some of the assumptions are changed. These changes do not affect much on the performance of the electrode, as discussed later in section 6.1. These assumptions are summarized as follows,

1. Electrolyte diffusion is neglected.

2. Binary diffusion in between O_2 and H_2O is considered.

3. O_2 is saturated with water vapor in ODC as well as in a gas chamber.

4. Total pressure is allowed to change as H_2O partial pressure changes.

5. Effect of N_2 is simulated by changing partial pressure of oxygen in the gas chamber [76].

6. Solid potential is assumed zero due to high conductivity of solid.

As per the above assumptions, H_2O vapor flux and it's partial pressure won't add any constrains on the ODC behavior therefore, these quantities are not calculated. Rest of the assumptions of Pinnow et al. [21] are the same.

4.4 MODEL EQUATIONS

Figure 4.3-a shows that, concentration gradient starts developing from the boundary layer, due to the electrochemical reaction.
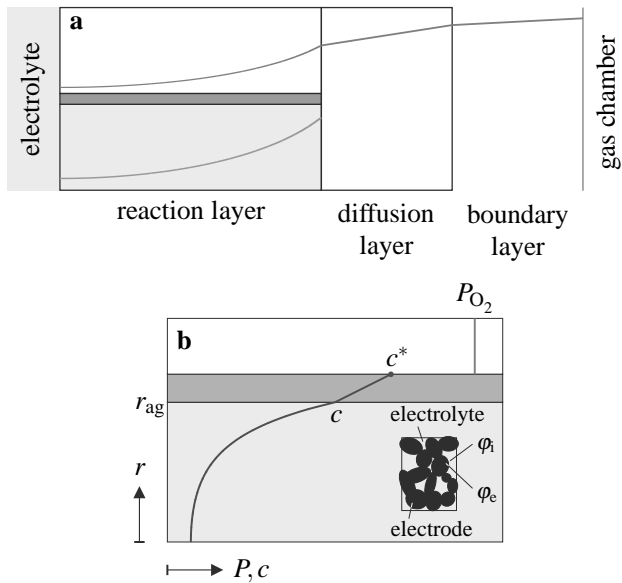
Figure 4.3: Schematic diagram of partial pressure and concentration profiles in various regions (reproduced with publisher's permission [21])

Therefore, O_2 mass transfer from the boundary layer to the RL needs to be calculated. The rate of reaction is calculated by Tafel equation and, the double layer current is calculated for dynamic behavior. Equations (4.3) to (4.5) calculate partial pressure of O_2 at steady state. Steady state equations are required to specify the initial values of dynamic state as well as to predict steady state performance.

Boundary layer

The change in O_2 partial pressure in the boundary layer ($P_{O_2,b}$) is calculated by Fick's law,

$$N_{O_2,b} = \frac{D_{O_2,H_2O}^{gas}}{RT} \frac{\partial P_{O_2,b}}{\partial z''} \tag{4.3}$$

where N_{O_2} is the oxygen flux, the additional subscript b denotes the boundary layer. D_{O_2,H_2O} is the binary diffusion coefficient of the subscripted species, R is the ideal gas constant and T is the temperature.

Gas Diffusion Layer

Due to Porosity and tortousity of the GDL and RL creates resistance to O_2 flow. Therefore, the effective diffusivity (D_{O_2,H_2O}^{eff}) is required in Fick's diffusion,

$$N_{O_2,s} = \frac{D_{O_2,H_2O,s}^{eff}}{RT} \frac{\partial P_{O_2,s}}{\partial z'} \tag{4.4}$$

where subscript s denotes in GDL. Similarly change in oxygen partial pressure ($P_{O_2,t}$) in RL is calculated by Fick's law,

Reaction Layer

$$N_{O_2,t} = \frac{D_{O_2,H_2O,t}^{eff}}{RT} \frac{\partial P_{O_2,t}}{\partial z} \tag{4.5}$$

Oxygen flux

Flux of the oxygen in RL is calculated by Faraday's equation,

$$N_{O_2}(z) = -4F\, j_{tf} \tag{4.6}$$

where j_{tf} is the faradic current. O_2 flux in GDL and boundary layer is equal to the RL flux at $z = 0$.

$$N_{O_2}(z = 0) = N_{O_2}(z') = N_{O_2}(z'') \tag{4.7}$$

Potential balance

As per the assumption no. 6 solid potential (φ_e) is assumed zero. Electrolyte's potential (φ_i) is calculated by Ohms's law,

$$\varphi_e = 0 \tag{4.8}$$

$$\frac{\partial \varphi_i}{\partial z} = \frac{j_i}{\kappa_i^{eff}} \tag{4.9}$$

where j_i and κ_i^{eff} is the ionic current density and the effective ionic conductivity respectively. At the end of RL ionic current density is equal to the external current density j.

$$j_i(z) = -j \tag{4.10}$$

Driving force for the reaction is the, potential difference between electrode and electrolyte phase; it is calculated by the following equation,

$$\Delta\varphi = -(\varphi_e - \varphi_i) \tag{4.11}$$

ODC overpotential (η) is calculated by the following equation,

$$\eta_{ODC} = \varphi_i(z_t) - \varphi_e - E \tag{4.12}$$

E^* is the equilibrium potential at $T = 80°C$.

---

* 231 mV experimental value

$P_{O_2,t}$ values obtained from the eq. (4.5) are the initial steady state values for unsteady state diffusion. Dynamic change of $P_{O_2,t}$ is calculated by following equation,

$$\frac{\partial P_{O_2,t}}{\partial t} = D^{\text{eff}}_{O_2,H_2O,t} \frac{\partial^2 P_{O_2,t}}{\partial z^2} - \frac{S_{\text{tf}}\, j_{\text{tf}}}{nF} \tag{4.13}$$

For the ORR oxygen must dissolve in the agglomerate's electrolyte film (see 4.3-b). Therefore, dissolved O_2 concentration (c^*) in the agglomerate's electrolyte film is calculated by Henry's law,

$$c^* = \frac{P_{O_2,t}}{He} \tag{4.14}$$

Specific surface area of thin-film (S_{tf}) is calculated by following equation,

$$S_{\text{tf}} = \frac{2}{r_{\text{ag}}} (1 - \epsilon_t) \tag{4.15}$$

where r_{ag} and ϵ_t are the radius of agglomerate and porosity of the RL respectively. The oxygen concentration change at the boundary of electrolyte film−agglomerate (c, see fig. 4.3) with respect to time can be calculated by following equation,

$$\frac{\partial c}{\partial t} = S_{\text{tf}} \left(\frac{D^l_{O_2}}{\delta_{\text{tf}}} (c^* - c) - \frac{j_{\text{tf}}}{nF} \right) \tag{4.16}$$

where δ_{tf} is the thickness of thin film, and j_{tf} is the faradic current; it is calculated by following equation,

$$j_{\text{tf}} = \begin{cases} -A_1\, c\, 10^{\frac{\Delta\varphi}{T_{s1}}} & \text{for } \eta \leq E_{\text{change}} \\ -A_2\, c\, 10^{\frac{\Delta\varphi}{T_{s2}}} & \text{for } \eta > E_{\text{change}} \end{cases} \tag{4.17}$$

Double layer current density (j_{di}) is calculated as follows,

$$j_{\text{di}} = C_{\text{d}} \frac{\partial \varphi}{\partial t} \tag{4.18}$$

where, C_d is double layer capacitance. The change in the local current density flowing through the electrolyte j_i is the sum of the double layer current density and the faradic current density,

$$\frac{\partial j_i}{\partial z} = S_{tf} \left(j_{di} + j_{tf} \right) \tag{4.19}$$

The rate of reaction (r) is calculated by the following equation,

$$r = S_{tf} \frac{j_{tf}}{4\,F} \tag{4.20}$$

The oxygen concentration in the agglomerate (c_{ag}) as with respect to time is calculated by the following equation,

$$\frac{\partial c_{ag}}{\partial t} = \frac{D_{O_2}^l}{r_{ag}} \left(\frac{\partial c_{ag}}{\partial r_{ag}} + r_{ag} \frac{\partial c_{ag}^2}{\partial r_{ag}^2} \right) - r \frac{c_{ag}}{c_{ag}(R_{ag})} \tag{4.21}$$

$c_{ag}(R_{ag})$ is the oxygen concentration, when, $r_{ag} = R_{ag}$. The partial pressure of oxygen in the gas chamber is increased a bit, from 1.0×10^5 Pa to 1.015×10^5 Pa. This change is required to equalize the current model and Pinnow et al. [21] model results. As per assumption no. 5—for 75% of N_2 partial pressure of O_2 in gas chamber is changed as follows,

$$P_{O_2}(z'' = 0) = 0.75 \cdot P_{O_2,3} \tag{4.22}$$

For 50% of N_2,

$$P_{O_2}(z'' = 0) = 0.5 \cdot P_{O_2,3} \tag{4.23}$$

The effectiveness factor (η_{eff}) is calculated by the following equation,

$$\eta_{eff} = \frac{\text{Average rate of reaction in the agglomerate}}{r} \tag{4.24}$$

To simulate the ripple effect the overpotential is made harmonic $\eta_{ODC,r}$ by using following equation [75],

$$\eta_{ODC,r} = \frac{3\sqrt{3}\,\eta_{ODC,peak}}{\pi} \left(1 - \sum_{k=1}^{+\infty} \frac{2}{36k^2 - 1} cos(12\pi f k t) \right), \tag{4.25}$$

where f is the frequency. $\eta_{\text{ODC,peak}}$ is calculated by following equation,

$$\eta_{\text{ODC,peak}} = \frac{\eta_{\text{ODC}}}{1.65} \tag{4.26}$$

where η_{ODC} is the constant voltage at which ODC is expected to be operated.

RESULTS AND DISCUSSION

5

STEADY-STATE SIMULATIONS

At low current density, kinetics is the limiting phenomenon in electrolysis, whereas at high current density mass transfer becomes limiting. Generally, the industrial scale electrolysis process is aimed to operate at higher current density. 1D+1D model reveals the location of the heat source and the cell's temperature distribution. It also determines the ODC's current and overpotential distribution. Following calculations are based on solution technique (1), in which ODC's overpotential is constant along the height and current density is varying. However, fig. 5.2 is based on solution technique (2), in which current density is constant (4 kA/m^2) along the height and ODC overpotential is varying. Enthalpy balance is carried out to determine the process of heat removal; it is based on electrolyte streams' inlet and outlet temperature obtained from the 1D+1D model. Later, the operating current density (j_{avg}) and the inlet oxygen concentration are varied, to understand the current density distribution of ODC.

5.1 COMPARISON OF THE TWO SOLUTION TECHNIQUES

Figure 5.1 shows the ODC current density distribution along the height for a constant overpotential (solution technique (1)). It can be seen that the difference between the top and the bottom of the electrolyzer is only about 293 A/m^2 at the chosen average current density of 4 kA/m^2. This result is the outcome of the distribution of transport parameters due to the temperature, for detail see Appendix A. Figure 5.2 shows the overpotential distribution in the ODC assuming a constant current density of 4 kA/m^2 (solution technique (2)) as a function of the electrolyzer height. The average overpotential in this case is 0.5848 V, which is almost identical to the constant value used for solution technique (1) (fig. 5.1).
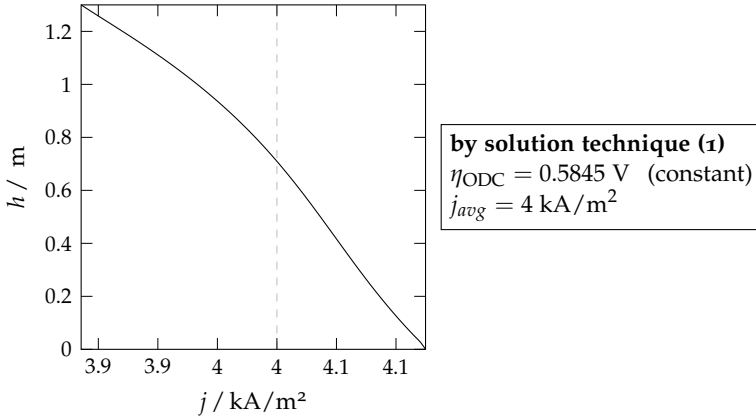
Figure 5.1: Current density distribution in the ODC along the height, assuming uniform overpotential in the ODC [45]

The results of these simulations reveal that neither current density (at constant overpotential) nor overpotential (at constant current density) exhibit strong variations over the height of the electrolyzer. For this reason, all following calculations are based on solution technique (1) assuming a constant overpotential in the ODC.

5.2 DISTRIBUTION OF CELL VOLTAGE AND TEMPERATURE

In fig. 5.3 the ohmic losses in the different cell compartments and their contribution to the total cell voltage are depicted as a function of height*. In agreement with earlier results by Jörissen et al. [8] one can see that, in addition to the equilibrium potential, ODC overpotential and ohmic losses in the membrane are the by far largest contributors to the resulting total cell voltage. It is furthermore evident that only the membrane losses are significantly changing as a function of height with the highest values occur-

---
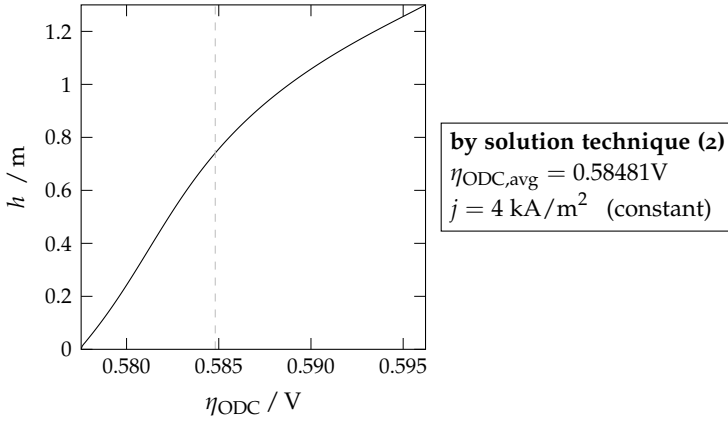
* for detail see appendix B

Figure 5.2: Overpotential distribution in the ODC along the height, assuming uniform current density in the ODC [45]

ring at the top of the cell. In contrast, the contributions of losses at the anode as well as in the brine and the caustic are relatively small[†]. This behavior can be explained with the developing temperature profile in the membrane which is depicted in fig. 5.4. It can be seen that the ODC is the hottest electrolyzer compartment, except for a small section at the top of the cell, where the brine, that is assumed to be ideally mixed, has a slightly higher temperature. This is due to both, the large amounts of reversible heat released and the high overpotential in the ODC (see fig. 5.5). Caused by the intimate contact between ODC, caustic falling film, membrane and anode, all these compartments have quite similar temperatures with differences of only a few kelvins. Larger deviations only occur at the very top of the cell where caustic solution enters with a temperature of 71 °C (cf. Table 3.4). The brine, which has an inlet temperature of 60 °C, exhibits a constant temperature of about 79.5 °C throughout the height of the brine chamber. Oxygen, that is fed with ambient temperature at the bottom of the cell, is heated very slowly by the hot ODC. Only at the top of the cell, gas temperatures around 78 °C are

---

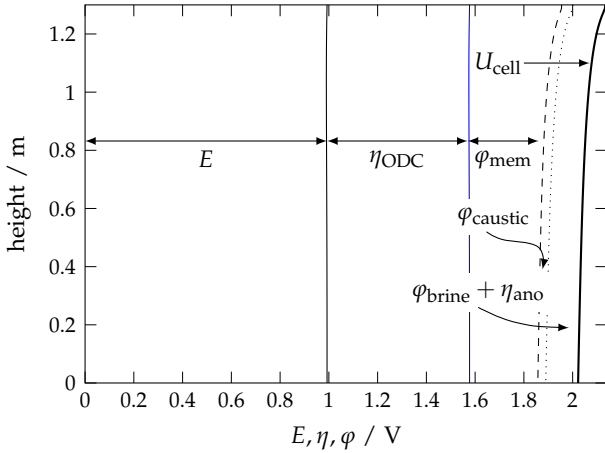[†] Individual profiles of heat source and sink are shown in appendix B.

Figure 5.3: Equilibrium potential, overpotentials, and ohmic losses in the cell as a function of height (solution technique (1)) [45]

achieved. This behavior can be explained by the low heat transfer coefficient in the gas phase.

Figure 5.5 shows the quantitative distribution of heat source/sink in the cell [‡]. Positive values indicate heat evolved and negative heat absorbed. At the anode reversible heat is absorbed and at the cathode it is evolved. The anode's Joule heat is quantitatively low compared to the reversible heat. As a result the Joule heat doesn't compensate the endothermic reversible heat. On the contrary, ODC Joule heat due to overpotential and exothermic reversible heat makes the ODC highest heat producing element of the cell. Membrane is the second highest contributor to the Joule heat. Ohmic losses in the brine and the caustic are of the same magnitude, therefore Joule heat produced on these elements have same magnitude. However, the heat produced in these liquid electrolytes is of much lower magnitude than the membrane and the ODC. Individual profiles of heat sources and sinks are shown in appendix C.

In tables 5.1 and 5.2, the operating parameters of the electrolyte
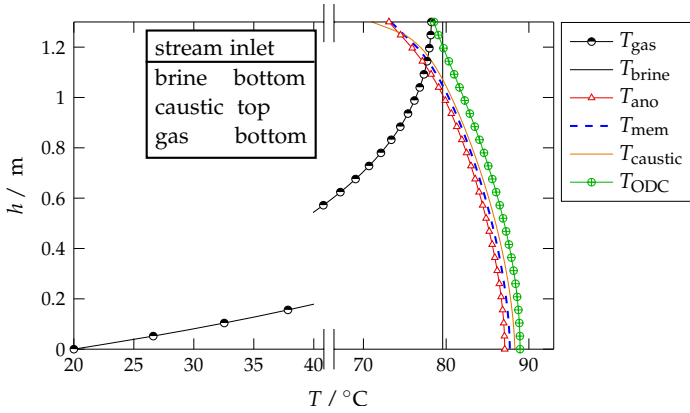
---

‡ for detail see appendix C

Figure 5.4: Temperature distributions in chlor-alkali cell along the height [45]

Table 5.1: Electrolyte streams' inlet parameters

Stream	Flow rate	Concentration	Temperature
Brine	237.6 kg/h	0.25 kg_{NaCl}/kg_{brine}	60 °C
caustic	453.6 kg/h	0.30 $kg_{NaOH}/kg_{caustic}$	71 °C
Gas	8.22 kg/h	0.025 mol_{H_2O}/mol_{gas}	20 °C

streams are summarized. The concentration changes in the brine and the caustic calculated with our model are in the same range as values reported for the conventional as well as the ODC based chlor-alkali electrolysis process [77, 78, 79]. For optimal performance of the cell, the outlet temperature of the caustic solution should be in a range from 85 °C to 95 °C [79] at cell temperatures from 82 °C to 90 °C [77]. Similarly, the brine flow rate should be maintained in such a way that the temperature difference between inlet and outlet of the caustic solution is not greater than 15 °C [79]. The model results shown in table 5.1 and table 5.2 reveal that our simulations and the reported industrial operation conditions are in the same range.
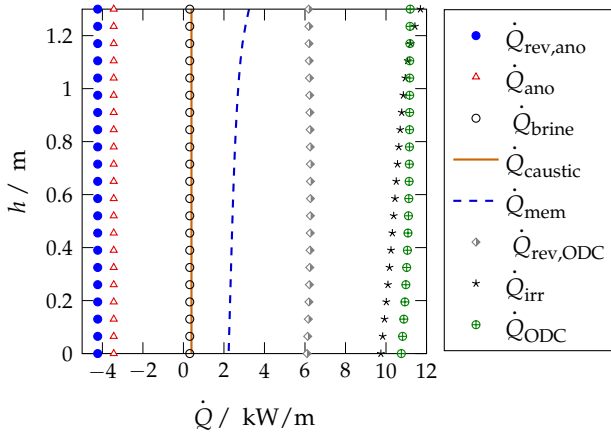
Figure 5.5: Location of the heat source/sink in electrolysis cell at 4 kA/m² (heat at the electrode is a summation of the reversible and Joule heat)

Table 5.2: Electrolyte streams' outlet parameters

Stream	Flow rate	Concentration	Temperature
Brine	183.0 kg/h	0.20 kg_{NaCl}/kg_{brine}	79.5 °C
caustic	494.4 kg/h	0.307 $kg_{NaOH}/kg_{caustic}$	88.3 °C
Gas	5.62 kg/h	0.182 mol_{H_2O}/mol_{gas}	78.1 °C

With the developed 1D+1D model, it is possible to calculate the temperature distribution in solid phases and electrolyte streams as discussed in the previous sections. However, the question remains if the electrolyzer is thermally balanced with the given simulation results. For this reason the enthalpy change in the electrolyte streams based on their inlet and outlet temperatures was compared with the total irreversible heat produced. The heat flow related to water evaporation in the brine chamber ($\dot{q}_{\lambda,\text{brine}}$) is given by the following equation

$$\dot{q}_{\lambda,\text{brine}} = \dot{m}_{H_2O_{(g)},\text{out,brine}} \left\{ H_{wg}(T_{\text{brine,out}}) - H_{wl}(T_{\text{brine,in}}) \right\}, \quad (5.1)$$

whereas the heat flow due to water evaporation in the gas chamber ($\dot{q}_{\lambda,\text{gas}}$) is obtained by

$$\dot{q}_{\lambda,\text{gas}} = (\dot{m}_{H_2O_{(g)},\text{out,gas}} - \dot{m}_{H_2O_{(g)},\text{in,gas}})$$
$$\left\{ H_{wg}(T_{\text{gas,out}}) - H_{wl}(T_{\text{caustic,in}}) \right\}. \quad (5.2)$$

The total heat related to water evaporation in the electrolyzer ($\dot{q}_{\lambda,\text{T}}$) is then the sum of the two terms. The overall enthalpy change in the electrolyte streams can finally be calculated with

$$\dot{q}_{\text{T}} = \sum_i \dot{m}_{i,\text{out}} c_{p,i,\text{out}}(T_{i,\text{out}} - T^{\ominus}) - \sum_i \dot{m}_{i,\text{in}} c_{p,i,\text{in}}(T_{i,\text{in}} - T^{\ominus})$$
$$+ \dot{q}_{\lambda,\text{T}}. \quad (5.3)$$

In the above equation i denotes liquid (brine, caustic) and gaseous (Cl_2, O_2, $H_2O_{(g)}$) streams. On the other hand, the irreversible heat produced in the cell is given by

$$\dot{q}_{\text{irr}} = j_{\text{avg}} A \left(U_{\text{cell,avg}} - E_{\text{avg}} \right.$$
$$\left. + \frac{-Q_{\text{rev,ano,avg}}}{n\,F} + \frac{-Q_{\text{rev,ODC,avg}}}{n\,F} \right). \quad (5.4)$$

Only in case of $\dot{q}_{\text{irr}} = \dot{q}_{\text{T}}$ the electrolyzer is thermally balanced and the simulation results are consistent. To achieve this goal,
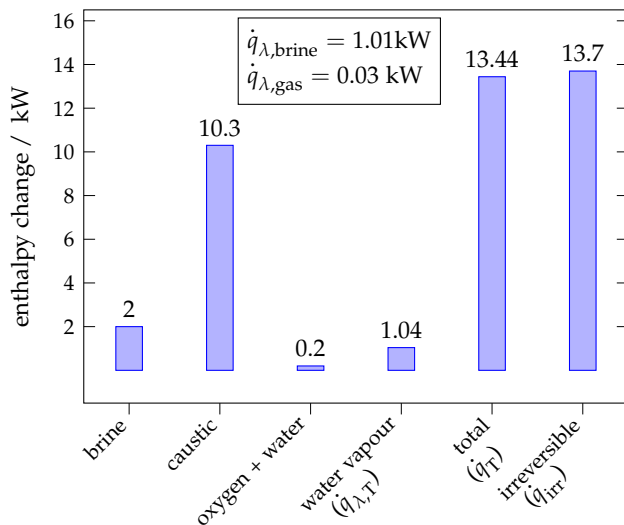
Figure 5.6: Change in enthalpy of flowing streams due to genera-
tion of heat [45]

overall enthalpy balance and 1D+1D model were solved itera-
tively using α_{brine} as fitting parameters. Figure 5.6 reveals that
consistent results could be obtained. The slight differences be-
tween enthalpy change and irreversible heat can be explained by
the fact that produced heat was calculated with average entropy
values whereas distributions as a function of the electrolyzer height
were taken into account for the enthalpy balance. Figure 5.6 also
shows that most of the released heat inside the electrolyzer is re-
moved through the liquid streams, especially the caustic solution.
This can be explained by high values of the heat transfer coeffi-
cient, heat capacity, and the mass flow rate of the sodium hy-
droxide solution. Caused by the lower flow rate and the vicinity
to the endothermic anode, the contribution of the brine is much
lower. The only significant contribution to the heat removal of the
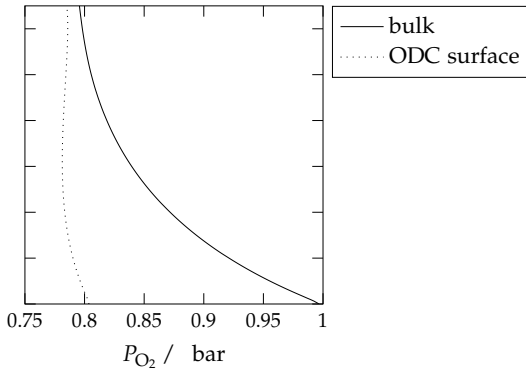gaseous streams is due to the evaporation of water in the brine
chamber.

Figure 5.7: Distribution of Partial pressure of oxygen in the bulk of gas stream and at the interface of ODC and boundary layer [45]

5.4 GAS CHAMBER

Insight into the operation of the ODC electrolyzer can also be gained from the calculated distribution of the oxygen concentration along the gas chamber as well as in the porous structure of the cathode. As the total pressure was fixed for the calculation and oxygen is consumed during the electrochemical reaction, the partial pressure of oxygen must decrease in the electrolyzer. Figure 5.7 shows the development of the oxygen pressure versus height in the bulk gas phase as well as at the end of the concentration boundary layer, i. e. at the surface of the ODC. The strong decrease of the concentration gradient in the boundary layer can be explained by the increasing temperature in the gas phase (cf. Figure 5.4), which favors the mass transport. Nevertheless, the change in the oxygen partial pressure along the height is less than 20%. Figure 5.8 shows that the oxygen distribution in the ODC is relatively homogeneous with a slight minimum occurring in the reaction layer at heights of 0.4 m to 0.8 m. It is interesting to note that due to the profiles of oxygen concentration and temperature as a function of height, the direction of the net water flow between the caustic solution and the gas chamber changes
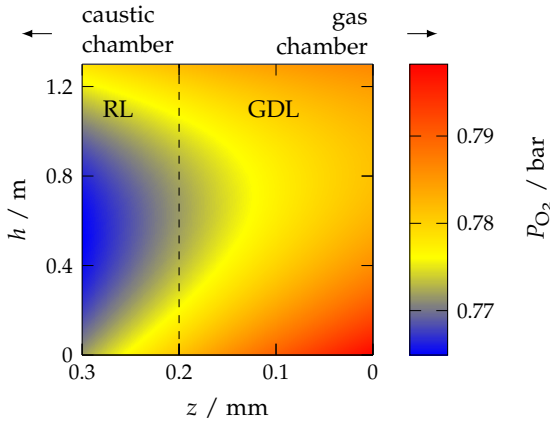
Figure 5.8: Distribution of oxygen pressure in ODC gas phase
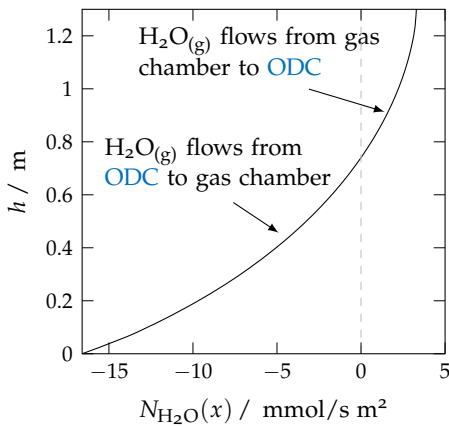(color denotes pressure in bar) [45]

Figure 5.9: Distribution of water vapor flux at the interface of
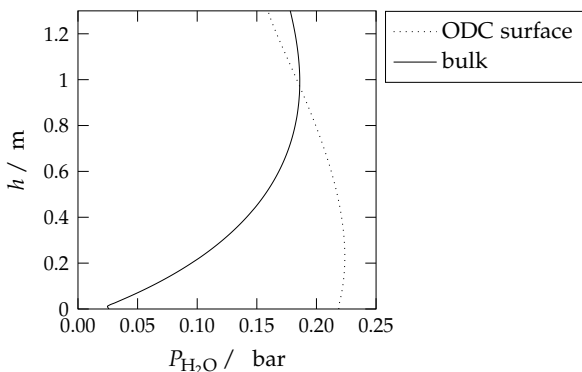boundary layer and gas chamber along the height [45]

Figure 5.10: Distribution of the partial pressure of water in the bulk of gas stream and at the interface of ODC and boundary layer

(fig. 5.9). It can be seen that the water flux at the interface of the concentration boundary layer and the bulk gas phase is negative until a height of about 0.7 m is reached. This means that water is transported from the catholyte through the ODC to the gas phase. This can be explained by fig. 5.10, where the partial pressure of water in the gas chamber is increasing along the height due to the transport of water. After a certain height the partial pressure profiles are intersecting. This behavior is caused by the decreasing temperature in the caustic with increasing height and the corresponding decrease of the saturation pressure. Nevertheless, the integral water flow in the whole cell is clearly directed from the caustic to the oxygen stream.

5.5 EFFECT OF CHANGE IN CURRENT DENSITY

It is common in industry to operate a cell at higher current density as it gives higher production rates. Therefore, it is necessary to understand the ODC behavior at a higher current density. Figure 5.11 shows that, as the average current density of ODC increases, the current density distribution along the height becomes more non-uniform. It is because at a higher current density more
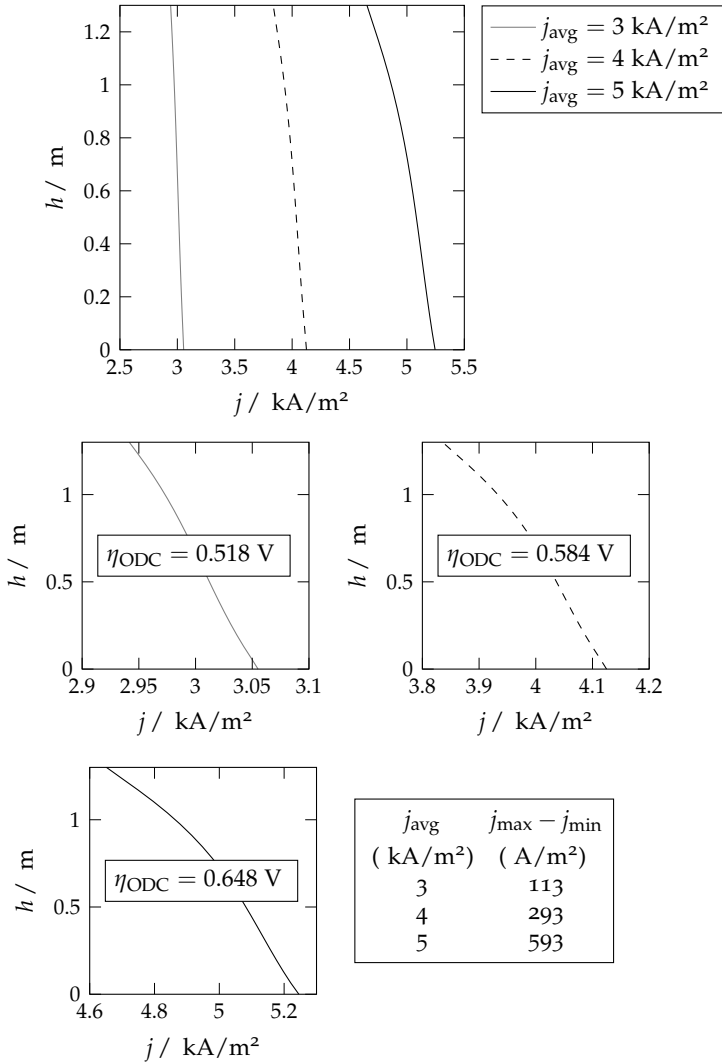
Figure 5.11: Effect of the changing average current density (at constant overpotential)
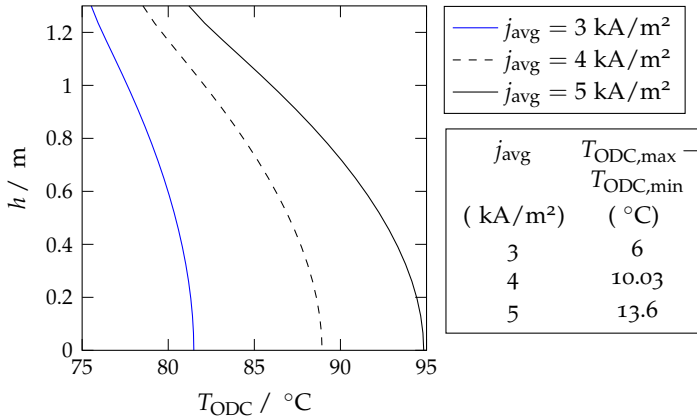
Figure 5.12: Effect of the changing average current density on the ODC temperature distribution

heat will be produced in the cell and the temperature of the ODC will also increase. Figure 5.12 shows the temperature distribution in the ODC for variation of the average current density distribution. As the average current density increases the ODC temperature distribution becomes more non-uniform reaching 95 °C at 5 kA/m². Similarly, current density distribution also becomes non-uniform as current density increases. Further increase in current density will raise the temperature of the cell that could damage the temperature sensitive membrane.

A summary of the electrolytes' important parameters is given in the table 5.3 and the table 5.4. However, caustic temperature becomes more non-uniform compared to ODC temperature, see fig. 5.13. It also shows that, at $j_{avg} = 5$ kA/m² caustic temperature at the bottom reaches 94 °C. Brine outlet concentration at $j_{avg} = 5$ kA/m² also gets lower i.e. 18.0% (see table 5.3) when compared to the conventional chlor-alkali cell's value [78]. Brine flow rate can be increased to cope the reduction of the brine concentration [79] and rise of electrolytes' temperature at higher current density.

Table 5.3: Calculated electrolytes' parameters at the outlet

j_{avg}	Temperature			Mass Fraction[†]		
	Brine	Caustic	Gas	Brine	Caustic	Gas
(kA/m^2)	(°C)	(°C)	(°C)	(kg_{NaCl}/kg_{brine})	$(kg_{NaOH}/kg_{caustic})$	(mol_{H_2O}/mol_{gas})
3	74.6	80.8	73.7	0.215	0.305	0.148
4	79.5	88.3	78.2	0.200	0.307	0.182
5	83.5	93.9	82.02	0.180	0.309	0.211

Table 5.4: Calculated electrolytes' outlet flow rate

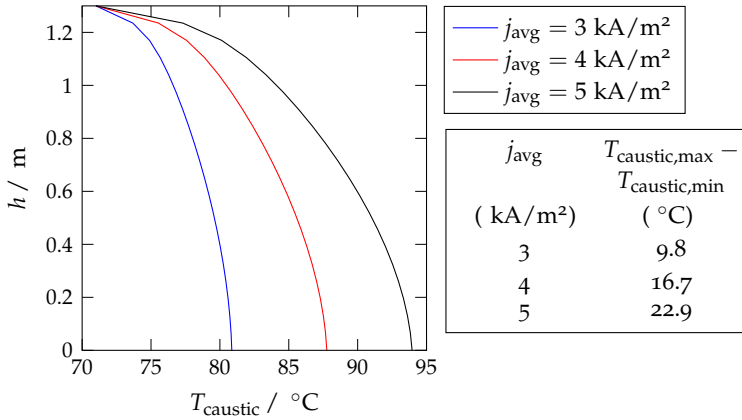| j_{avg}	Flow rate		
	Brine	Caustic	Gas
(kA/m^2)	(kg/hr)	(kg/hr)	(kg/hr)
3	197.3	484	5.71
4	183	494.4	5.62
5	169.47	504.31	4.1

Figure 5.13: Effect of changing average current density on caustic temperature distribution

5.5.1 *Enthalpy balance*

Figure 5.14 shows the enthalpy balance of the electrolyte streams at various current densities. The results shows that as current density increases the heat production also increases. In heat removal the caustic solution plays an important role, while brine solution remains almost un-affected. It is due to the increased flow of water from the brine chamber to the caustic chamber along with Na^+ ions. Water evaporation along with chlorine gas also increases.

5.6 EFFECT OF CHANGE OF CONCENTRATION

Using oxygen at a lower concentration is always lucrative for an industrial scale operation. In an extreme case ODC working on air will give substantial financial benefits given that overpotential is lower than hydrogen evolution reaction. However, using impure oxygen obtained by Pressure Swing Adsorption (PSA) might be the first step toward the ultimate goal of using air-ODC. PSA produces oxygen concentration in the range of 88% to 93% [80]. Therefore, in this section the performance of the industrial
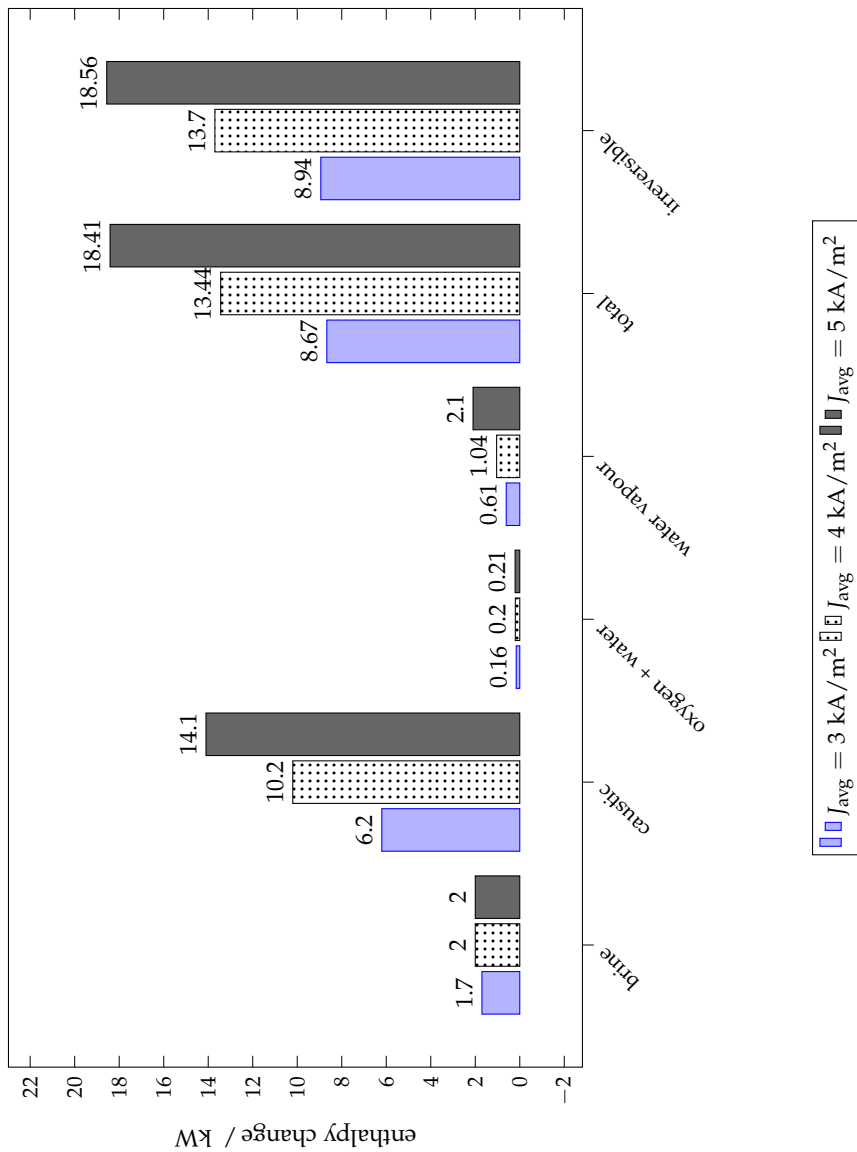
Figure 5.14: Change in enthalpy of flowing streams at various current densities
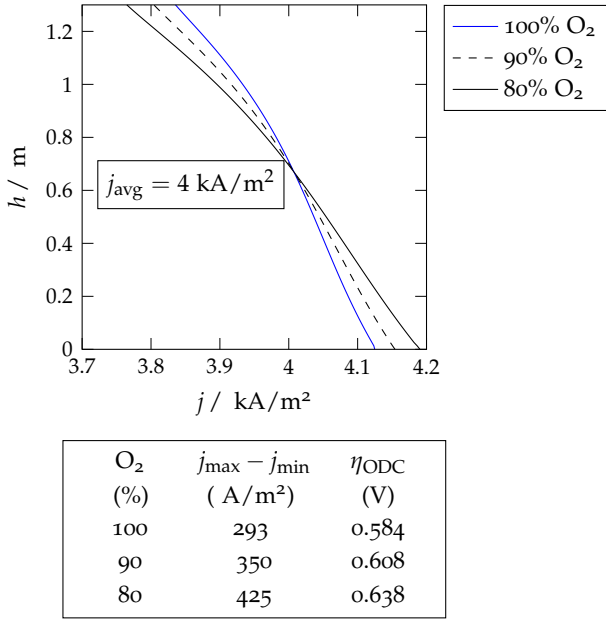
Figure 5.15: Effect of variation in oxygen partial pressure on the current density distribution (j_{avg}=4 kA/m^2)

scale ODC is predicted for the variation in the oxygen concentration. The experimental effect of the variation of the oxygen concentration on the ODC performance is extensively studied by Polcyn [81]. Pinnow et al. [21] validated the TFFA model using these experimental results. However, above mentioned work were performed on laboratory scale electrodes. In current work the focus is on the industrial scale electrode performance. Figure 5.15 shows the current density distribution for variation in the oxygen concentration at an average current density of 4 kA/m^2. It is evident that, up to 90% of oxygen there is insignificant change in the current density distribution. Rise in the ODC temperature is also minimal as can be seen from fig. 5.16. Figure 5.17 shows the partial pressure distribution of the components of the gases along the height of the gas chamber. Due to the constant average current density i.e. 4 kA/m^2 the oxygen partial pressure reduc-
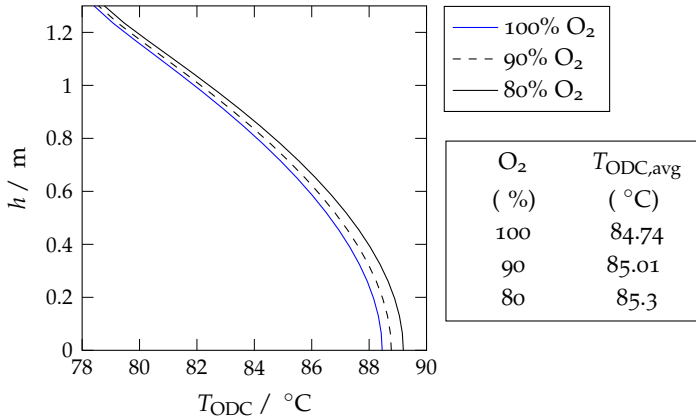
Figure 5.16: Effect of variation in oxygen partial pressure on ODC temperature distribution (j_{avg}=4 kA/m^2)

tion along the height is of the same magnitude. While the water partial pressure along the height doesn't change significantly due to the temperature rise in ODC is minimal. Thus, ODC can be operated at lower oxygen concentration. Figure 5.18 (page 86) shows the working of NaCl-ODC electrolyzer with PSA unit and recycling of gas stream. In this illustration, it is assumed that O_2 concentration at the inlet of gas chamber is 80% and 88% at the outlet of PSA unit. O_2 concentration at the outlet of the gas chamber will be approximately 62% at 4 kA/m^2 and other parameters are same as given table 5.1. Purging of the recycle stream is necessary to reduce the concentration of inert nitrogen.
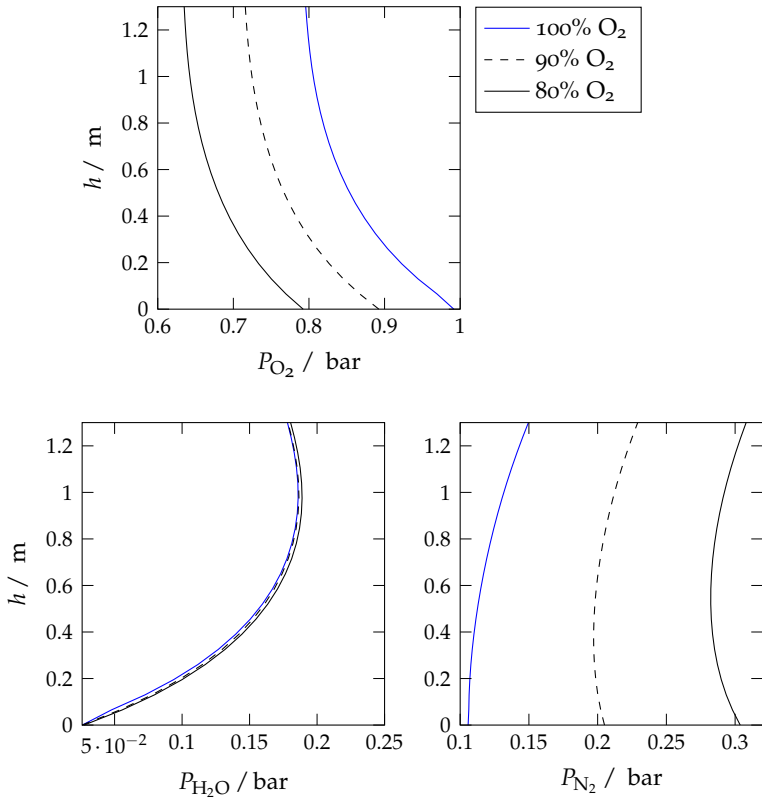
Figure 5.17: Effect of variation in oxygen partial pressure on the gas chamber's partial pressure profile along the height (j_{avg}=4 kA/m^2)
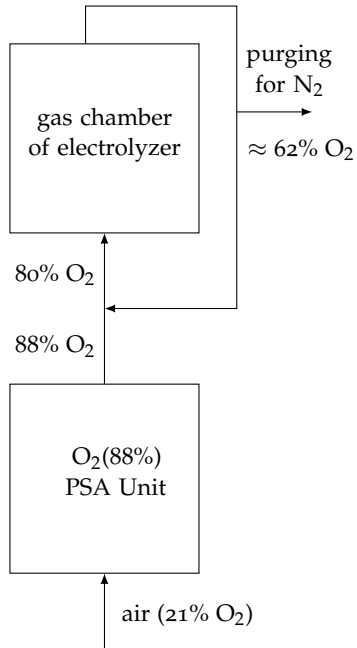
Figure 5.18: Illustration of using oxygen produced by PSA unit and it's recycling

Every solution breeds new problems.
— Arthur Bloch

6

DYNAMIC MODEL SIMULATIONS

In previous chapter, simulation results of the steady state model are shown. In this chapter, simulation results of the dynamic state are discussed. To validate the dynamic model, CI measurement data has been used. Experimental results by the Polcyn [81] are used to validate the simplified TFFA model. Later, the performance of the ODC is predicted under the effect of ripple voltage.

6.1 COMPARISON OF SIMPLIFIED MODEL

For ease in the calculation model developed by the Pinnow et al. [21] is simplified. To understand the difference, both models' results are compared at steady state. Structural parameters of the ODC are the same as given in [21]. Figure 6.1 shows the comparison of the simplified and Pinnow et al. [21] model. Results of the both models are almost the same except at high current densities. For all simulations Tafel slopes, pre-exponential factors (A_1 and A_2) and equilibrium potential are the same as given in the [21]. Thus simplified model can be used to do further calculations.

6.2 PRINCIPLE OF CURRENT INTERRUPTION TECHNIQUE

Generally, CI technique is used to determine electrode's ohmic losses. When external current goes zero i.e. interrupted, ohmic losses vanish and the double layer starts to discharge. Thus, local current continues to flow and the overpotential decay starts. After some characteristic time (time constant), it reaches the equilibrium potential. CI technique separates the physical and chemical processes on different time scale. Thus, it offers the unique opportunity to investigate reaction's mechanism and kinetic parameters e.g. Tafel slope and exchange current density. Potential relaxation obtained from the current interruption method is free
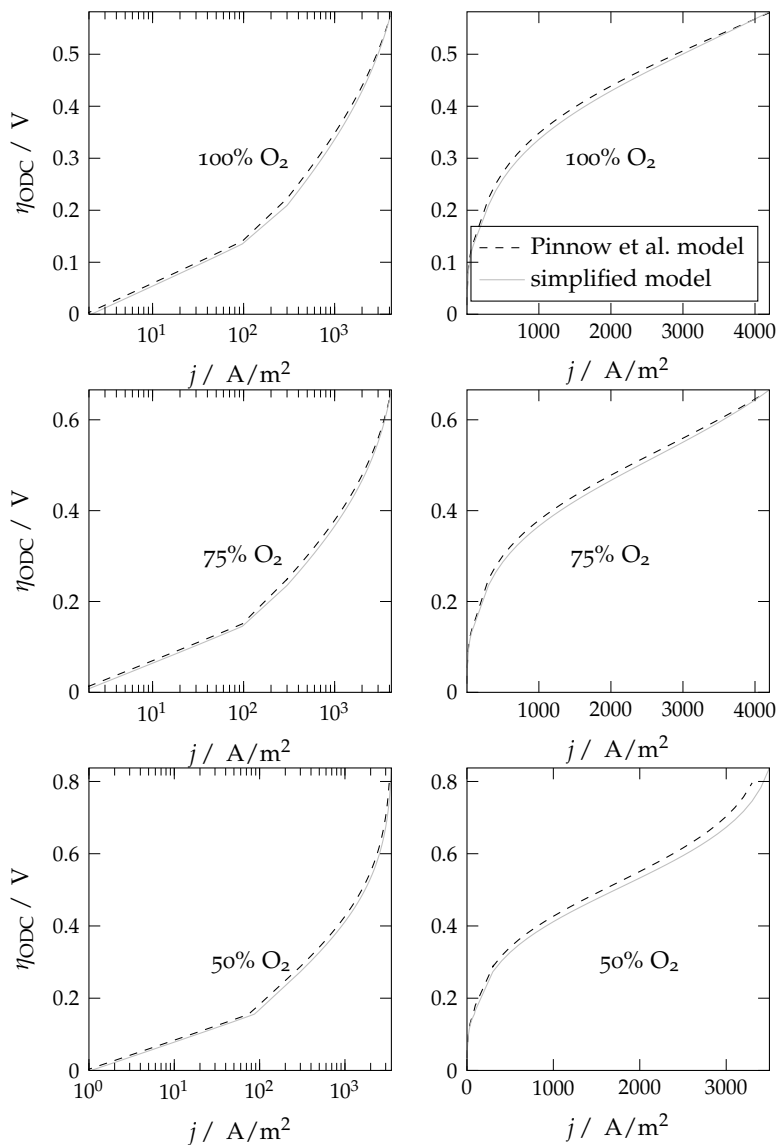
Figure 6.1: comparison of simplified model with Pinnow et al. [21] model for variation in oxygen partial pressure
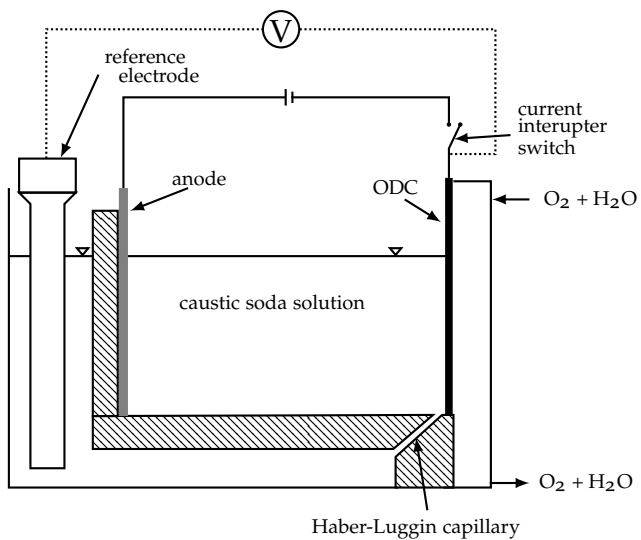
Figure 6.2: Illustration of the principle of working of CI measurement.

of IR losses, contrary cell running under steady state includes the IR losses. Therefore, Tafel slopes obtained by the steady state technique, and by the CI are different, particularly at high current density.

Figure 6.2 shows the principle of working of CI measurement. With the help of Haber-Luggin capillary overpotential of the ODC is measured against the reference electrode when current is interrupted. Current interruption measurements were performed by Polcyn [81] at TU Dortmund university. For these measurements caustic soda concentration was 0.31 $kg_{NaOH}/kg_{caustic}$ at 80 °C and humidified O_2 fed to the electrode. ODCs used in these measurements were manufactured by the spray process [17]. Current interrupter switch breaks down the current within $< 1\mu s$, when cell is operating in steady state at a particular current density. Potential relaxation is measured against the reference electrode. Ohmic losses are eliminated within $< 10^{-10}$ s after current interruption. Later diffusion and reaction overpotential relaxes at their respective time constants.

6.3 STEADY STATE PERFORMANCE WITH AND WITHOUT IR CORRECTION

Figure 6.3 shows the IR corrected experimental data and the modeling results simulated for pure oxygen. Experimental result used in previous work [21] were at steady state but not IR corrected. Table 6.1 shows the comparison of fitting parameters used in previous work [21] (with IR losses) and without IR losses (shown in fig. 6.3). fig. 6.4 shows the overpotential difference before and after current interruption due to the IR losses in the electrode. As shown in the figure, even at low current density i.e. 1 kA/m^2 IR loss is 10 mV. Thus, it is necessary to use the IR corrected overpotential.

In CI technique, when, external current goes zero, electrode seek new steady state potential and current density. *This new steady state potential and current density is called as equilibrium potential and exchange current density.* During simulation when current interrupts, in eq. (4.10) an exchange current density has been used i.e. $j = j_{01}$, because it is a new steady state current density.
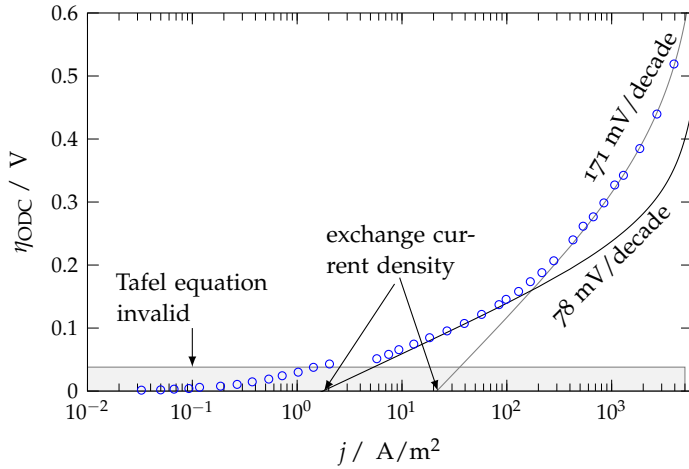
Figure 6.3: IR corrected experimental data at steady state in presence of pure oxygen and model results
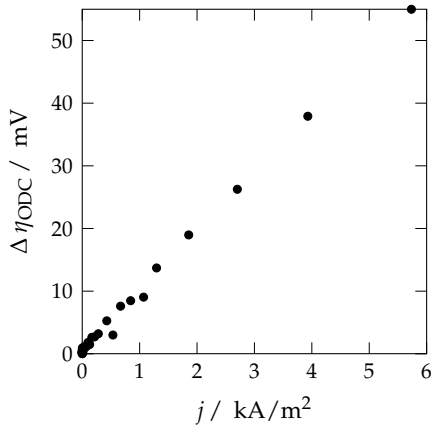

Figure 6.4: Overpotential difference before and after current interruption

Table 6.1: Comparison of fitting parameters of steady state model with and without IR correction

Name	Symbol	Unit	Value with IR losses (from [21])	Value without IR losses (from fig. 6.3)
Equilibrium potential	E	mV	214	231[+]
Low potential region				
Constant	A_1	A m/mol	0.007	0.003
Tafel slope	T_{s1}	mV/decade	80	78
Exchange current density	j_{01}	A/m²	3	2
High potential region				
Constant	A_2	A m/mol	4	1.5
Tafel slope	T_{s2}	mV/decade	200	171
Exchange current density	j_{02}	A/m²	37	22

+ experimental value

This section discusses the possibility of fitting experimental CI data by using the parameters used to fit steady state data. Experimental points (symbol) shown in fig. 6.5(A) are obtained by interrupting curve at 1855 A/m², in presence of pure oxygen. Black curve in fig. 6.5 is simulated by using the parameters which fits IR corrected experimental steady state data (see also table 6.2). Black curve in current interruption follows the experimental points up to the 0.01 s later it deviates and finally relaxes at 2 s. Possible reason of deviation could be high exchange current density. It is known that ODC kinetics is sluggish [82], therefore exchange current density should be low. On the contrary, an exchange current density from the model is high i. e. 2 A/m². This problem arises due to the limitation of Tafel equation in low potential region.

As per aforementioned arguments discussed in above paragraph, model parameters are changed to fit experimental CI data; see dotted curve in fig. 6.5. In a fuel cell study by Jaouen et al. [26] showed that, Tafel slope and exchange current density of the steady state need to be change to fit potential relaxation of the GDE in dynamic state. In case of ODC also, Tafel slopes and pre-exponential factors are changed; comparison of fitting parameters is given in the table 6.2. Major difference is low value of A_1 compared to steady state value. Steady state curve simulated by using the CI-fitting-parameters is shown in fig. 6.5 (B) (dotted line). This curve shows the deviation from experimental values in low potential region, due to the low value of A_1.

6.5 CURRENT DENSITY VARIATION IN PRESENCE OF PURE OXYGEN

Figure 6.6 shows the potential relaxation curves, when current is interrupted at different current densities. Symbols are experimental results, while lines overlapping the experimental points are the results of the model. Fitting parameters are the same as given in table 6.2 for CI fit. Model seems to be in good agreement with experimental values up to 10 s and corresponding overpo-
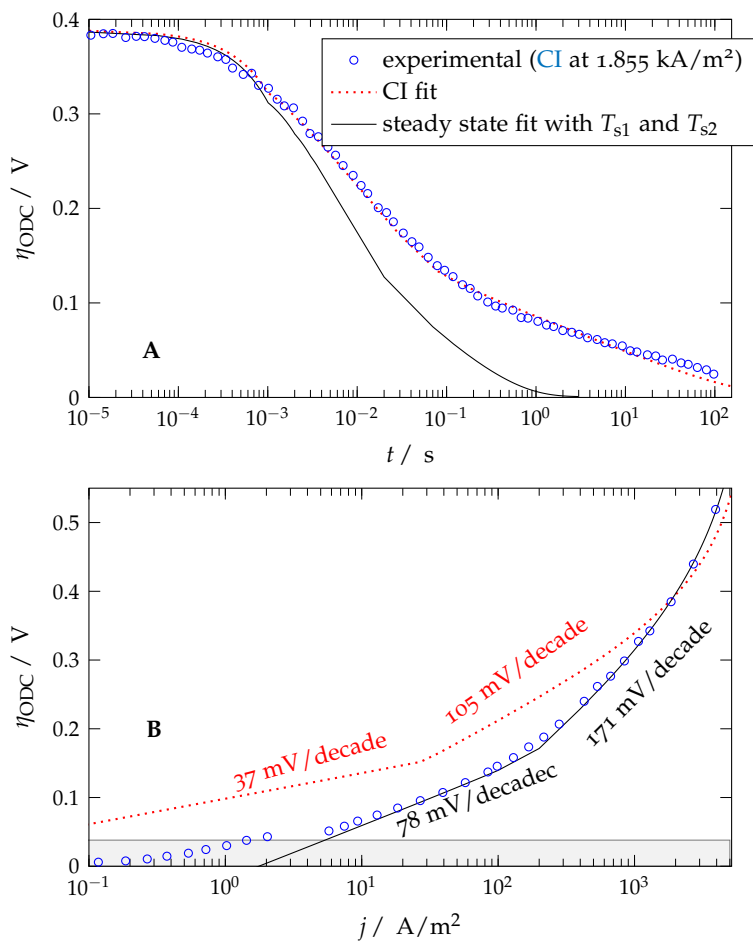
Figure 6.5: Current interruption (A) and steady state (B) results in presence of pure oxygen

Table 6.2: Model fitting parameters in steady state and CI data

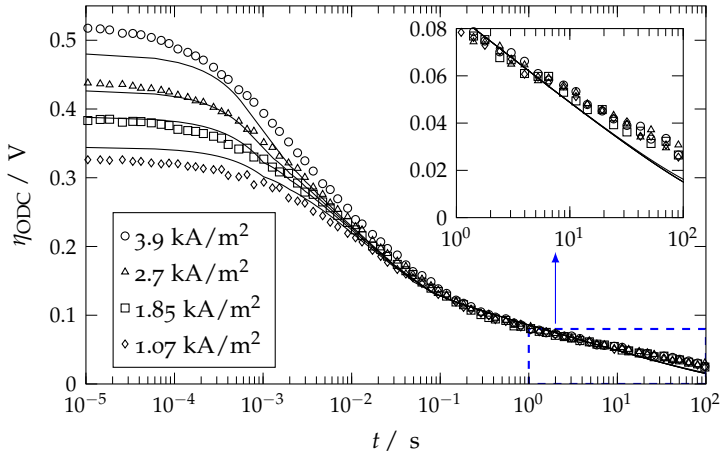| Name	Symbol	Unit	Value CI fit	Value steady state fit (IR corrected)
Capacitance	C_d	F/m²	0.5	0.5
Low potential region				
Constant	A_1	A m/mol	2×10^{-9}	0.003
Tafel slope	T_{s1}	mV/decade	37	78
Exchange current density	i_{01}	A / m²	0.003	2
High potential region				
Constant	A_2	A m/mol	0.01	1.5
Tafel Slope	T_{s2}	mV/decade	105	171
Exchange current density	i_{02}	A/m²	1	22

Figure 6.6: Current interruption at various current densities in presence of pure oxygen (symbol: experiment and line: model)

tential is 50 mV. After 10 s model overpotential relax faster than experimental values.

6.6 VARIATION OF OXYGEN PARTIAL PRESSURE IN GAS CHAMBER

Figure 6.7 shows the CI experimental data (symbols) at different current density and O_2 partial pressure. Lines overlapping the experimental points are the results of the model. Fitting parameters are the same as given in table 6.2 for CI fit except the equilibrium potential. For 75% and 50% oxygen equilibrium potential are 236 mV and 223 mV respectively. Capacitance affects the initial relaxation time, and it is same for all three cases.
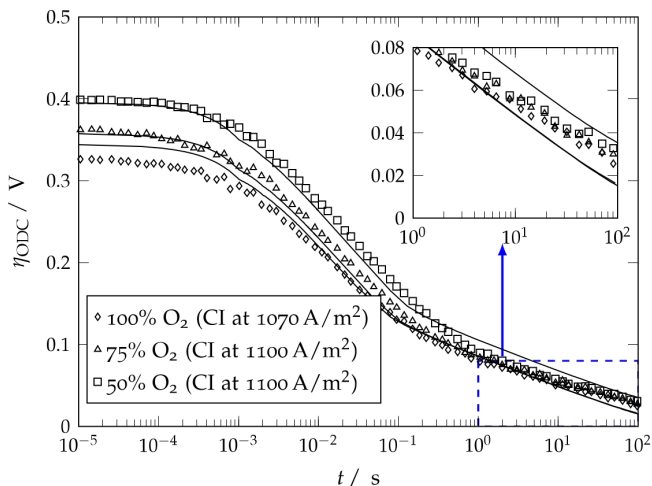
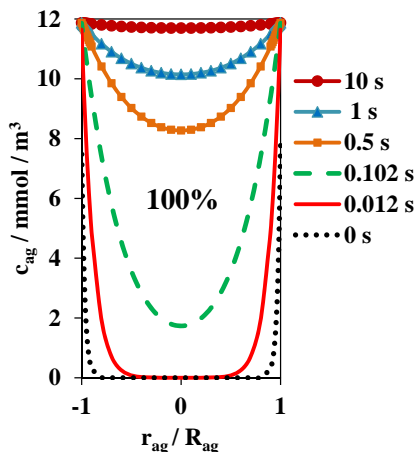Figure 6.7: Current interruption results of variation in partial pressure of oxygen

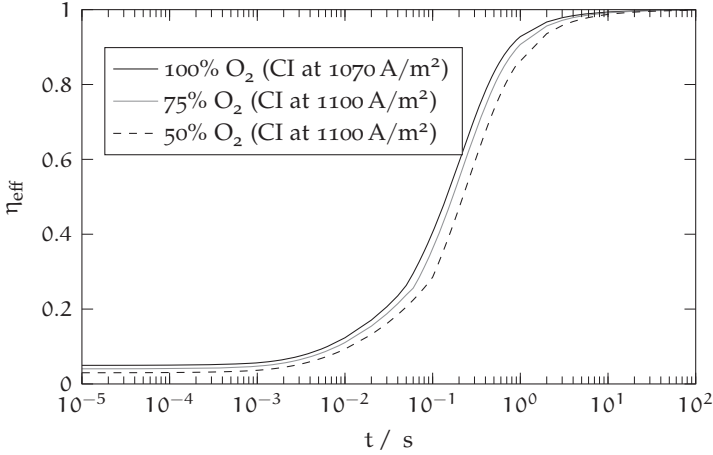Figure 6.8: Change in oxygen concentration in agglomerate with respect to time 100% oxygen partial pressure (CI at 2.7 kA/m^2)

Figure 6.9: Effectiveness factor change with respective time for variation in oxygen concentration

6.7 EFFECT OF OXYGEN PARTIAL PRESSURE ON THE CONCENTRATION RELAXATION IN THE AGGLOMERATE

Pinnow et al. [21] showed that ODC is under strong mass transfer limitation. It implies that, concentration relaxation time will be more. We also know that, ODC kinetic is sluggish [82], therefore kinetic relaxation time will be also high. It is question: how much is the kinetic and concentration relaxation time ? Figure 6.8 shows the concentration relaxation time in agglomerate is approximately 10 seconds for pure (100%) oxygen. Kinetic relaxation time can be calculated by subtracting the concentration relaxation time from total time i. e. 100 s (see fig. 6.6), which gives 90 s. Thus, kinetic relaxation time is longer than the concentration relaxation time.

Higher the kinetic relaxation time (τ_{kr}), lower the exchange current density and both parameter are related by following equation,

$$i_0 = \frac{R\,T C_d}{F \tau_{kr}} \tag{6.1}$$

Relaxation of effectiveness factor is shown in the fig. 6.9 for the variation in oxygen partial pressure. It can be seen that the irrespective of the oxygen pressure electrode remain in mass transfer control until 10 s.

6.8 EFFECT OF RIPPLE ON THE ELECTRODE

Previous section validate the dynamic model simulated for CI measurements. Thus, the dynamic model can be further used to understand the effect of the ripple on the performance of the electrode. Three phase rectifier can not suppress completely the sinusoidal current thus producing ripple. An increased heat production, a reduction in current efficiency and the life span of electrode are the adverse effect of the residual ripple. The amplitude of the overpotential oscillation is fixed by eq. (4.25) thus, the frequency is the only parameter that can be varied. Figure 6.10 shows the performance of the electrode when subjected to ripple voltage. As the frequency of the oscillation increases the hysteresis becomes more pronounced. At low frequency (1 Hz), the current-overpotential relationship in steady state and under ripple voltage coincide. However, at higher frequency hysteresis appear (100 Hz). In practice, frequency from the power plant grid is 50 Hz [83]. However, further increasing frequency i.e. 500 Hz reduces the amplitude of current oscillation. Cell operating at lower overpotential, exhibit a low amplitude of current oscillation thus, reduces the hysteresis. Figure 6.11 shows the comparison of the current-potential relationship at different O_2 partial pressures and frequencies. There is no significant difference in the amplitude of the current even after reduction of O_2 partial pressure up to 75%. Thus, ODC operating under ripple and lower oxygen concentration will not affect adversely on the performance of the electrode.
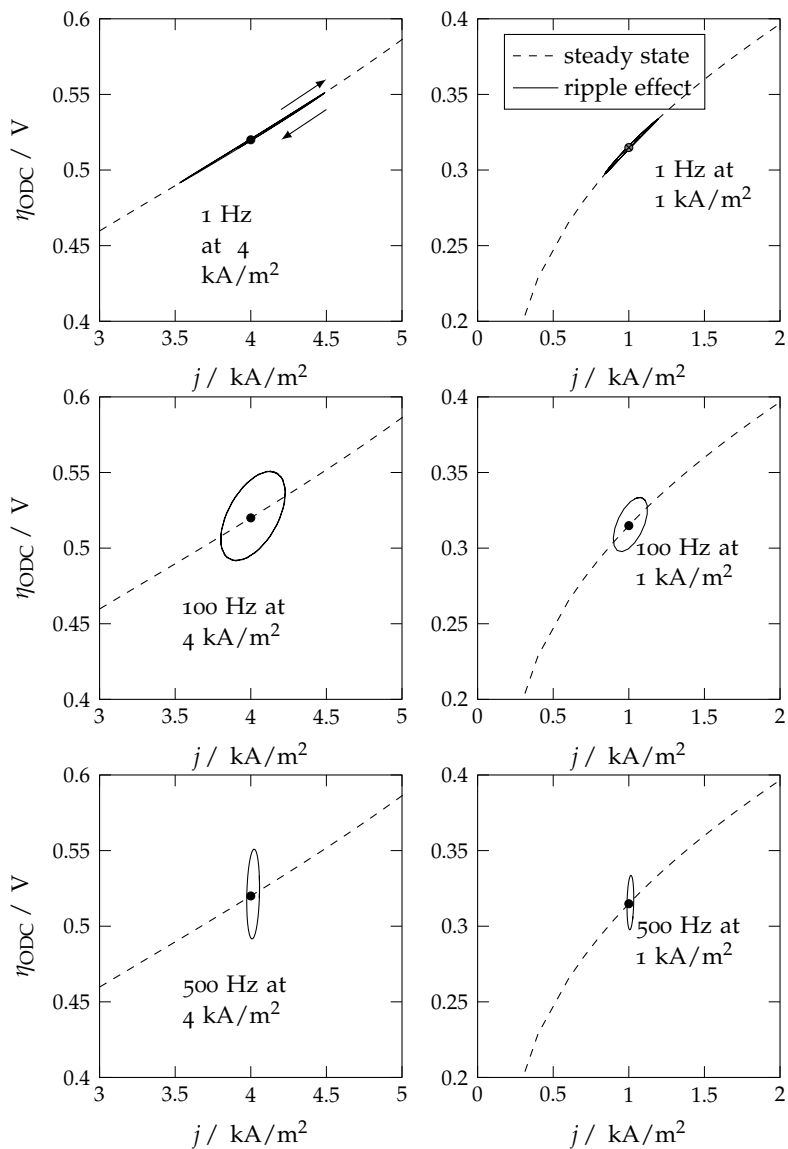
Figure 6.10: Comparison of the performance of the electrode at various ripple frequency and current density
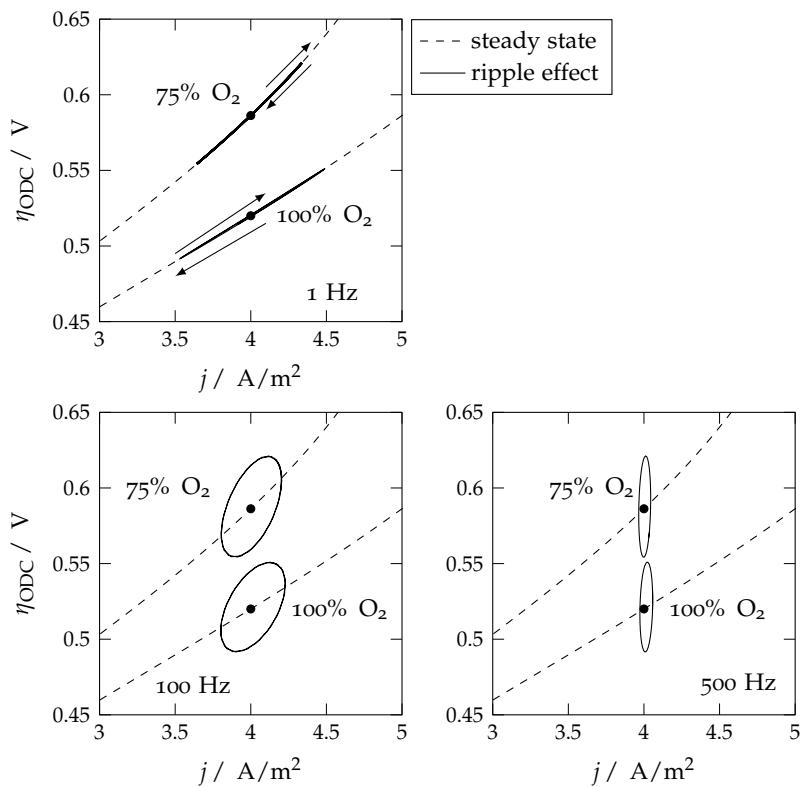
Figure 6.11: Comparison of the performance of the electrode at various ripple frequency and partial pressure

SUMMARY

*"We live on an island surrounded by a
sea of ignorance. As our island of knowledge
grows, so does the shore of our ignorance."*
— John Archibald Wheeler

CONCLUSION

Steady state (non-isothermal 1D+1D) and dynamic models are developed to understand the performance of the ODC working in industry. The height dependent model calculates the mass and heat balance along the height of technical electrolysis cell at an industrially relevant current density. For the mass balance the brine chamber is assumed as Continuous Stirred-Tank Reactor while the caustic and the gas chambers are under the Plug flow conditions. For the heat balance the Joule's heat and the reversible heat are the sources while electrolyte streams flowing through the chambers are the sinks. Apart from that, some of the transport parameters in Thin-Film Flooded Agglomerate model are made temperature dependent. Finally, two iteration loops were developed to couple the TFFA model and height dependent model.

With the model it is possible to calculate the distributions of the temperature, the concentration, the current density, and the overpotential along the height of the electrolyzer. The results obtained at an industrially relevant current density of $4 \, \text{kA/m}^2$ reveal that neither the current density nor the overpotentials exhibit strong variations along the cell height. One of the main reasons for this desirable behavior is that the temperature distributions in the solid compartments of the electrolyzer (anode, membrane, ODC) are relatively homogeneous with variations in the range of 10 K. Obviously the heat transfer between the electrodes, where the endothermic (anode) and exothermic (cathode) electrochemical reactions take place, and the electrolyte streams is highly efficient. This is especially true for the caustic solution, through which most of the irreversible heat released in the cell

is removed. For this reason zero-gap cell configurations, where the membrane and the ODC are in direct contact would have poorer heat management properties. Although the ODC is the hottest compartment in the cell, the temperature of the oxygen stream increases only slowly until at the top of the electrolyzer gas temperatures around $78\,^{\circ}\text{C}$ are achieved. Due to the initially low temperatures and the low water content of the inlet oxygen stream, the gas phase takes up considerable amounts of water vapor until at a certain height of the cell the direction of the water flow is reversed. Nevertheless, the oxygen partial pressure at the electrochemically active regions of the ODC remains high allowing for an efficient operation of the cathode.

Operating at cell at higher current density increases heat production significantly. It results in a temperature rise in the cell components and in the electrolyte streams. This rise eventually results in a non-uniform current density distribution. To cope with this problem, it is necessary to increase the mass flow rate of caustic solution keeping the constant inlet temperature. It will also help to maintain the caustic concentration almost uniform along the height. In addition, brine flow rate also must be increased to maintain brine's outlet concentration around 0.20 $\text{kg}_{\text{NaCl}}/\text{kg}_{\text{brine}}$. This strategy will maintain cell at lower temperature.

Using pressure swing adsorption or locally available recycled oxygen of lesser concentration may give financial benefit over the pure one. With state of the art electrode, reducing oxygen concentration upto the 90% is possible. It neither significantly increases the overpotential nor the temperature of the ODC. However, using 90% oxygen at a higher current density i.e. 5 kA/m^2 will need improved heat management as discussed above. It also needs long term studies to understand the effect of using lower concentration oxygen on electrocatalyst activity. It is also necessary to evaluate financial trade-off between savings due to usage of impure oxygen and corresponding increase of electricity demand.

Above modeling work is based on the certain assumption which limits the accuracy of the results. For example, assuming hundred percent current efficiency, plug flow in the gas chamber and Tafel slope independent of temperature etc. However, to re-

move these assumptions, further detailed experimental work is required. Furthermore, for validation of the model experimental results are needed. However, experimental evaluation current density distribution of an industrial scale electrode will require significant capital. Nevertheless, these results seems to be promising where the Oxygen Reduction Reaction is carried out in alkaline environment e. g. Zinc-air battery. These findings encourage to built these electrolytic cells for mass production which will give good financial return when compared to the conventional electrolysis cell.

A dynamic model has been developed, to understand the performance of the electrode in industrial set-up i.e. under the ripple voltage. CI measurement data has been used to validate this model. Results showed that, the concentration within the agglomerate relaxes in ≈ 10 s irrespective of oxygen partial pressure in gas chamber. Complete relaxation of the overpotential takes place more than 100 s. Thus, the kinetic relaxation time is much higher than the diffusion relaxation time. This confirms that, the kinetics of the ODC is sluggish and exchange current density must be very low. Influence of the ripple on the performance of the electrode is investigated with varying frequency and oxygen partial pressure. Operating a cell at constant current is possible at a higher frequency as the amplitude of the current gets lower as frequency increases. However, in Europe the frequency from power grid is fixed i.e. 50 Hz. Nevertheless, cell operating at 4 kA/m^{2}and 100 Hz, amplitude of current oscillation is only ± 300 A/m^2. There is no appreciable difference in the amplitude of the current density even after lowering oxygen partial pressure i. e. at 75%. These results infers that, industrial scale ODC operating on lower oxygen concentration and under ripple current won't have any adverse effect on the performance of the cell.
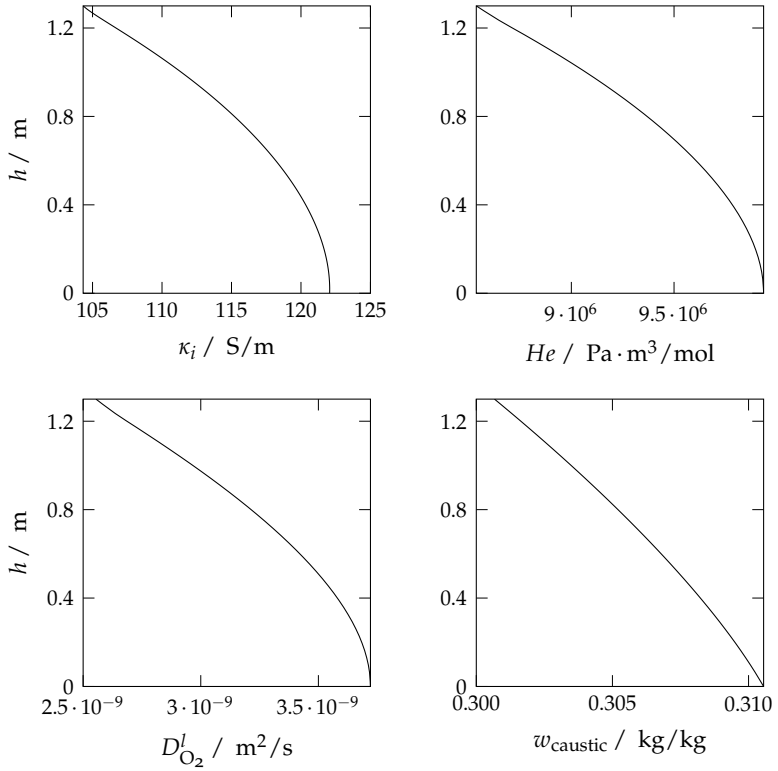
APPENDIX

VARIOUS PARAMETERS ALONG THE HEIGHT

Figure A.1: Variation in physical parameters along the height (y-axis is h in meter)
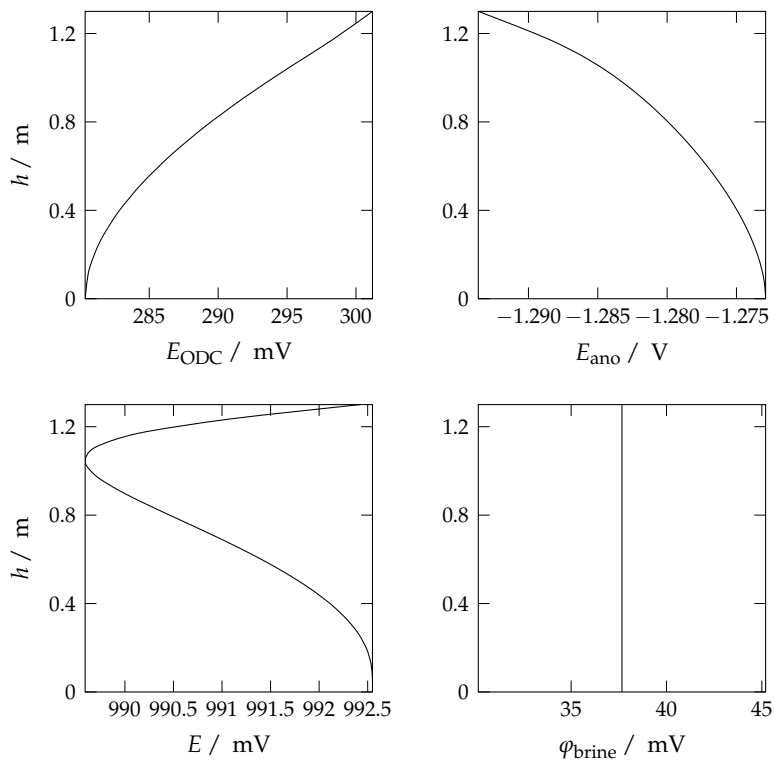
EQUILIBRIUM POTENTIAL AND OHMIC LOSSES

Figure B.1: Equilibrium potential and ohmic losses in various component of cell at 4 kA/m² (*y*-axis is *h* in meter)
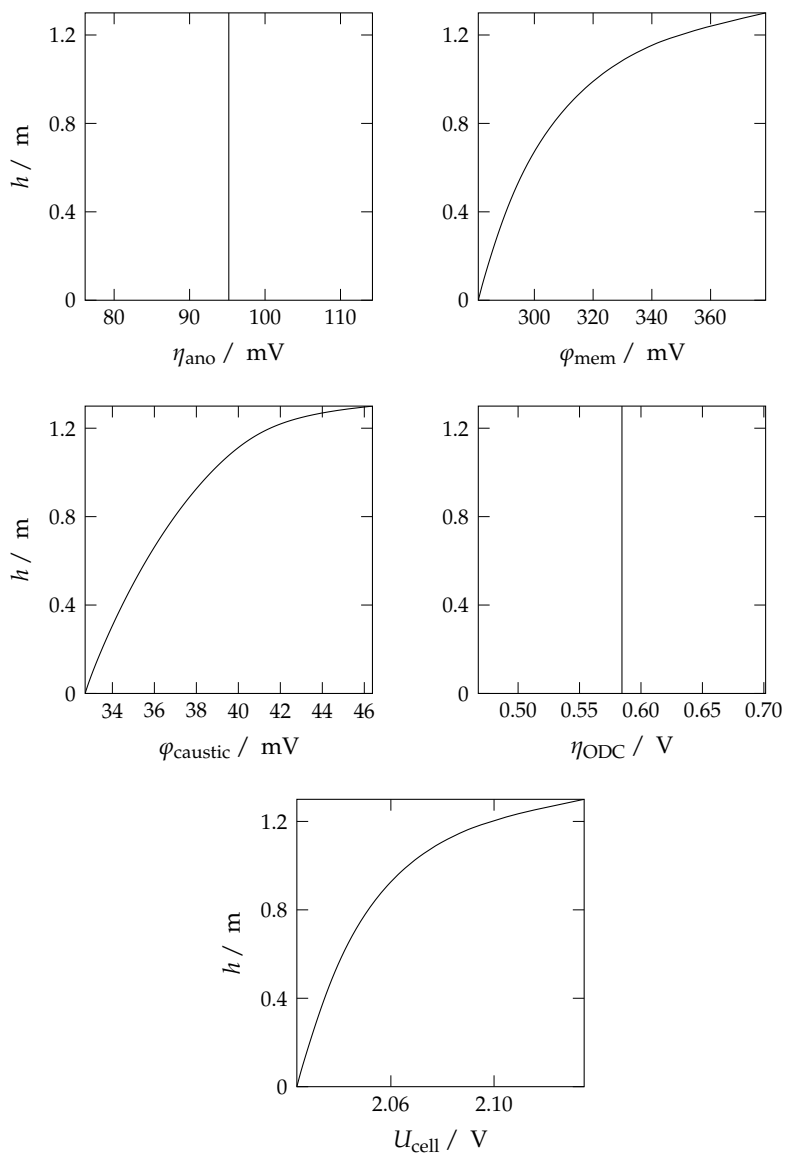
Figure B.2: Equilibrium potential and ohmic losses in various component of cell at 4 kA/m² (*y*-axis is *h* in meter)
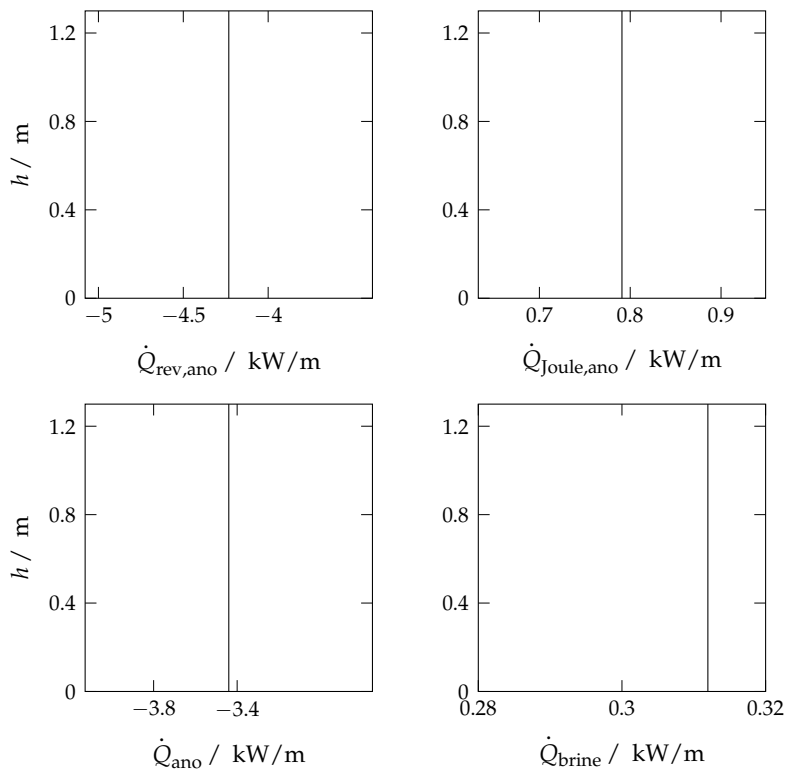
LOCATION OF HEAT SOURCE AND SINK

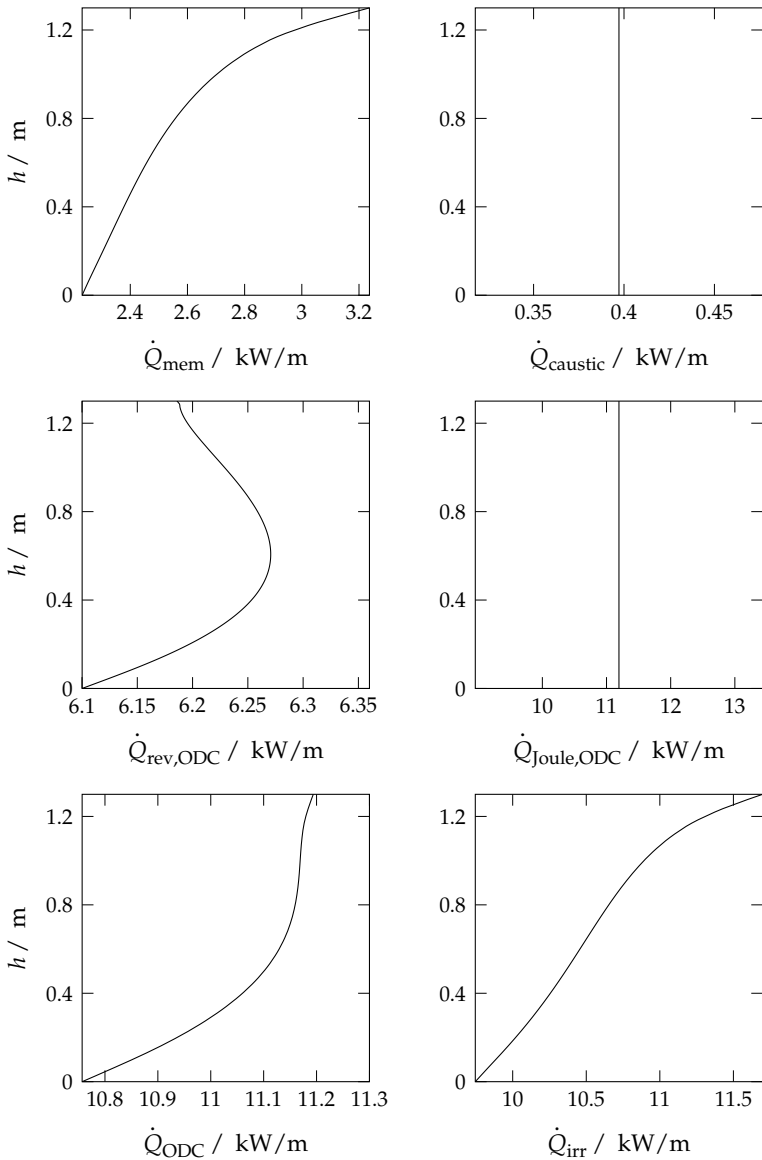Figure C.1: Heat location source/sink at 4 kA/m^2 (y-axis is h in meter)

Figure C.2: Heat location source/sink at 4 kA/m^2 (*y*-axis is *h* in meter)

BIBLIOGRAPHY

[1] *World chlorine council - sustainable development report-2002*. accessed on 19.03.2015. World chlorine council. URL: www. worldchlorine.org/wp-content/themes/brickthemewp/pdfs/ report.pdf.

[2] *The European chlor-alkali industry: an electricity intensive sector exposed to carbon leakage 2010*. accessed on 19.03.2015. Eurochlor. URL: www.eurochlor.org/media/9385/3-2-the_ european_chlor-alkali_industry_-_an_electricity_intensive_sector_ exposed_to_carbon_leakage.pdf.

[3] IHS Chemical. *World Analysis – Chlor-Alkali*. Tech. rep. 2014.

[4] *Chlorine Industry Review 2013-2014*. accessed on 19.03.2015. Eurochlor. URL: http://www.eurochlor.org/chlorine-industry- issues / sustainability / chlorine- industry- review- 2013- 2014. aspx.

[5] *Questions and Answers on the Chlor-Alkali Sector and the EU Emission Trading System (ETS)*. accessed on 06.04.2014. Eurochlor. URL: http://www.eurochlor.org/media/9379/3- 2-questions_and_answers_on_the_chlor-alkali_sector_and_the_ eu_emission_trading_system.pdf.

[6] P. Schmittinger, T. Florkiewicz, L. C. Curlin, B. Lüke, R. Scannell, T. Navin, E. Zelfel, and R. Bartsch. Chlorine. In: *Ullmann's Encyclopedia of Industrial Chemistry*. Wiley-VCH Verlag GmbH & Co. KGaA, 2000. DOI: 10.1002/14356007. a06_399.pub3.

[7] *The Uhde membrane process: Technical data*. accessed on 19.03.2015. Thyssenkrupp Electrolysis. URL: http://www.thyssenkrupp- electrolysis.com/products/chlor-alkali-electrolysis/conventional- electrolysis/technical-data.html.

[8]   J. Jörissen, T. Turek, and R. Weber. Chlorherstellung mit Sauerstoffverzehrkathoden. Energieeinsparung bei der Elektrolyse. In: *Chemie in unserer Zeit* 45.3 (2011), pp. 172–183. DOI: 10.1002/ciuz.201100545.

[9]   *Chlor-Alkali Manufacturing Processes*. accessed on 19.03.2015. World Chlorine Council. URL: www.worldchlorine.org/wp-content/themes/brickthemewp/pdfs/mfg_processes.pdf.

[10] *Chlorine Production Capacities per country*. accessed on 01.07.2013. Euro-chlor. URL: http://www.eurochlor.org/facts-figures-glossary/chlorine-production-capacities-per-country.aspx.

[11] T. F. O'Brien, T. V. Bommaraju, and F. Hine. Chemistry and Electrochemistry of the Chlor-Alkali Process. English. In: *Handbook of Chlor-Alkali Technology*. Vol. 1. Springer US, 2005. Chap. 4, pp. 75–386. DOI: 10.1007/0-306-48624-5_4.

[12] *The mercury cell process*. accessed on 17.01.2014. Eurochlor. URL: http://www.eurochlor.org/the-chlorine-universe/how-is-chlorine-produced/the-mercury-cell-process.aspx.

[13] I. Moussallem, J. Jörissen, U. Kunz, S. Pinnow, and T. Turek. Chlor-alkali electrolysis with oxygen depolarized cathodes: history, present status and future prospects. In: *J Appl Electrochem* 38.9 (2008), pp. 1177–1194. DOI: 10.1007/s10800-008-9556-9.

[14] I. Moussallem, S. Pinnow, and T. Turek. Möglichkeiten zur Energierückgewinnung aus Wasserstoff bei der Chlor-Alkali-Elektrolyse. In: *Chem Ing Tech* 81.4 (2009), pp. 489–493. DOI: 10.1002/cite.200800172.

[15] V. M. Schmidt. *Elektrochemische Verfahrenstechnik: Grundlagen, Reaktionstechnik, Prozessoptimierung*. John Wiley & Sons, 2012. URL: http://eu.wiley.com/WileyCDA/WileyTitle/productCd-352766064X.html.

[16] S. Pinnow. Modellierung von Sauerstoffverzehrkathoden für die Chloralkali-Elektrolyse. PhD thesis. TU Clausthal, 2013.

[17] I. Moussallem, S. Pinnow, N. Wagner, and T. Turek. Development of high-performance silver-based gas-diffusion electrodes for chlor-alkali electrolysis with oxygen depolarized cathodes. In: *Chem Eng and Process: Process Intensifi* 52.0 (2012), pp. 125 –131. DOI: 10.1016/j.cep.2011.11.003.

[18] *Smart technologies*. accessed on 20.03.2015. Bayer materialScience. URL: http://www.materialscience.bayer.com/en/Sustainability/Clean-Production/Processes.aspx.

[19] *Technical data*. accessed on 10.03.2014. Thyssenkrupp Electrolysis. URL: http://www.thyssenkrupp-electrolysis.com/products/chlor-alkali-electrolysis/nacl-odc-electrolysis/technical-data.html.

[20] G. Faita and F. Federico. *Electrochemical cell with gas diffusion electrodes*. EP Patent 1,446,515. 2011. URL: http://www.google.com/patents/EP1446515B1?cl=en.

[21] S. Pinnow, N. Chavan, and T. Turek. Thin-film flooded agglomerate model for silver-based oxygen depolarized cathodes. In: *J Appl Electrochem* 41.9 (2011), pp. 1053–1064. DOI: 10.1007/s10800-011-0311-2.

[22] T. F. O'Brien, T. V. Bommaraju, and F. Hine. Chemical Engineering Principles. English. In: *Handbook of Chlor-Alkali Technology*. Vol. IV. Springer US, 2005. Chap. 10, pp. 1013–1087. DOI: 10.1007/0-306-48624-5_10.

[23] A. J. deBethune, T. S. Licht, and N. Swendeman. The Temperature Coefficients of Electrode Potentials: The Isothermal and Thermal Coefficients—The Standard Ionic Entropy of Electrochemical Transport of the Hydrogen Ion. In: *J Electrochem Soc* 106.7 (1959), pp. 616–625. DOI: 10.1149/1.2427448. eprint: http://jes.ecsdl.org/content/106/7/616.full.pdf+html.

[24] G. R. Salvi and A. J. deBethune. The Temperature Coefficients of Electrode Potentials: ii . The Second Isothermal Temperature Coefficient. In: *J Electrochem Soc* 108.7 (1961), pp. 672–676. DOI: 10.1149/1.2428187.

[25] P. Atkins and J. De Paula. *Elements of physical chemistry*. Oxford University Press, 2012. Chap. Resource section, pp. 569–580. URL: http://ukcatalogue.oup.com/product/9780199608119.do.

[26] F. Jaouen, G. Lindbergh, and K. Wiezell. Transient techniques for investigating mass-transport limitations in gas diffusion electrodes ii. Experimental characterization of the PEM-FC cathode. In: *J Electrochem Soc* 150.12 (2003), A1711–A1717. DOI: 10.1149/1.1624295.

[27] A. Z. Weber and J. Newman. Modeling transport in polymer-electrolyte fuel cells. In: *Chemical Reviews* 104.10 (2004), pp. 4679–4726. DOI: 10.1021/cr020729l.

[28] A. Parthasarathy, S. Srinivasan, A J. Appleby, and C. R. Martin. Temperature dependence of the electrode kinetics of oxygen reduction at the platinum/Nafion® interface—a microelectrode investigation. In: *J Electrochem Soc* 139.9 (1992), pp. 2530–2537. DOI: 10.1149/1.2221258.

[29] A. Parthasarathy, S. Srinivasan, A. J. Appleby, and C. R. Martin. Pressure dependence of the oxygen reduction reaction at the platinum microelectrode/Nafion® interface: electrode kinetics and mass transport. In: *J Electrochem Soc* 139.10 (1992), pp. 2856–2862. DOI: 10.1149/1.2068992.

[30] J. C. Amphlett, R. Baumert, R. F. Mann, B. A. Peppley, P. R. Roberge, and T. J. Harris. Performance modeling of the Ballard Mark IV solid polymer electrolyte fuel cell II. Empirical model development. In: *J Electrochem Soc* 142.1 (1995), pp. 9–15. DOI: 10.1149/1.2043959.

[31] A.C. West and T.F. Fuller. Influence of rib spacing in proton-exchange membrane electrode assemblies. English. In: *J Appl Electrochem* 26.6 (1996), pp. 557–565. DOI: 10.1007/BF00253453.

[32] J. Euler and W. Nonnenmacher. Stromverteilung in porösen Elektroden. In: *Electrochim Acta* 2.4 (1960), pp. 268 –286. DOI: 10.1016/0013-4686(60)80025-4.

[33] L. G. Austin, M. Ariet, R. D. Walker, G. B. Wood, and R. H. Comyn. Simple-Pore and Thin-Film Models of Porous Gas Diffusion Electrodes. In: *Ind Eng Chem Fund* 4.3 (1965), pp. 321–327. DOI: 10.1021/i160015a015.

[34] E. A. Grens II and C. W. Tobias. The influence of electrode reaction kinetics on the polarization of flooded porous electrodes. In: *Electrochim Acta* 10.8 (1965), pp. 761–772. DOI: 10.1016/0013-4686(65)80041-X.

[35] M. Keddam, C. Rakotomavo, and H. Takenouti. Impedance of a porous electrode with an axial gradient of concentration. English. In: *J Appl Electrochem* 14.4 (1984), pp. 437–448. DOI: 10.1007/BF00610808.

[36] C. Cachet and R. Wiart. Couple axial gradients of potential and concentration in a cylindrical pore electrode: an impedance model. In: *J Electroanal Chem* 195.1 (1985), pp. 21–37. DOI: 10.1016/0022-0728(85)80002-4.

[37] M. B. Cutlip. An approximate model for mass transfer with reaction in porous gas diffusion electrodes. In: *Electrochim Acta* 20.10 (1975), pp. 767–773. DOI: 10.1016/0013-4686(75)85013-4.

[38] T. E. Springer, T. Zawodzinski, and S. Gottesfeld. Polymer electrolyte fuel cell model. In: *J Electrochem Soc* 138.8 (1991), pp. 2334–2342. DOI: 10.1149/1.2085971.

[39] D. M. Bernardi and M. W. Verbrugge. A Mathematical Model of the Solid-Polymer-Electrolyte Fuel Cell. In: *J Electrochem Soc* 139.9 (1992), pp. 2477–2491. DOI: 10.1149/1.2221251.

[40] M. Eikerling, Yu I. K., A. Kornyshev, and Y. M. Volfkovich. Phenomenological Theory of Electro-osmotic Effect and Water Management in Polymer Electrolyte Proton-Conducting Membranes. In: *J Electrochem Soc* 145.8 (1998), pp. 2684–2699. DOI: 10.1149/1.1838700.

[41] M. L. Perry, J. Newman, and E. J. Cairns. Mass Transport in Gas-Diffusion Electrodes: A Diagnostic Tool for Fuel-Cell Cathodes. In: *J Electrochem Soc* 145.1 (1998), pp. 5–15. DOI: 10.1149/1.1838202.

[42] K. Broka and P. Ekdunge. Modelling the PEM fuel cell cathode. In: *J Appl Electrochem* 27.3 (1997), pp. 281–289. DOI: 10.1023/A:1018476612810.

[43] C. Lagergren, G. Lindbergh, and D. Simonsson. Investigation of Porous Electrodes by Current Interruption Application to Molten Carbonate Fuel Cell Cathodes. In: *J Electrochem Soc* 142.3 (1995), pp. 787–797. DOI: 10.1149/1.2048537.

[44] M. A. Al-Saleh, S. Gultekin, Sleem ur Rahman, and A. Al-Zakri. Modified flooded spherical agglomerate model for gas-diffusion electrodes in alkaline fuel cells. In: *J Power Sources* 55.1 (1995), pp. 33 –39. DOI: 10.1016/0378-7753(94)02161-U.

[45] Naresh Chavan, Stefan Pinnow, Gregor D. Polcyn, and Thomas Turek. Non-isothermal model for an industrial chlor-alkali cell with oxygen-depolarized cathode. In: *J Appl Electrochem* 45.8 (2015), pp. 899–912. DOI: 10.1007/s10800-015-0831-2.

[46] X.-L. Wang and S. Koda. Scale-up and Modeling of Oxygen Diffusion Electrodes for Chlorine-Alkali Electrolysis I. Analysis of Hydrostatic Force Balance and its Effect on Electrode Performance. In: *Denki Kagaku* 65.12 (1997), pp. 1002–1013.

[47] X.-L. Wang and S. Koda. Scale-up and Modeling of Oxygen Diffusion Electrodes for Chlorine-Alkali Electrolysis II. Effects of the Structural Parameters on the Electrode Performance Based on the Thin-Film and Flooded-Agglomerate Model. In: *Denki Kagaku* 65.12 (1997), pp. 1014–1025.

[48] M. Chatenet, M. Aurousseau, and R. Durand. Comparative Methods for Gas Diffusivity and Solubility Determination in Extreme Media: Application to Molecular Oxygen in an Industrial Chlorine-Soda Electrolyte. In: *Ind Eng Chem Res* 39.8 (2000), pp. 3083–3089. DOI: 10.1021/ie000044g.

[49] J. Olsson, Å Jernqvist, and G. Aly. Thermophysical properties of aqueous NaOH—H$_2$O solutions at high concentrations. In: *Int J Thermophys* 18.3 (1997), pp. 779–793. DOI: 10.1007/BF02575133.

[50] M. Neubronner, T. Bodmer, C. Hübner, P. B. Kempa, E. Tsotsas, A. Eschner, G. Kasparek, F. Ochs, H. Müller-Steinhagen, H. Werner, and M. Spitzner. D6 Properties of Solids and Solid Materials. In: *VDI Heat Atlas*. VDI-Buch. Springer Berlin Heidelberg, 2010, pp. 551–614. DOI: 10.1007/978-3-540-77877-6_26.

[51] S. I. Abu-Eishah. Correlations for the Thermal Conductivity of Metals as a Function of Temperature. English. In: *Int J Thermophysics* 22.6 (2001), pp. 1855–1868. DOI: 10.1023/A:1013155404019.

[52] D. A. G. Bruggeman. Berechnung verschiedener physikalischer Konstanten von heterogenen Substanzen. I. Dielektrizitätskonstanten und Leitfähigkeiten der Mischkörper aus isotropen Substanzen. In: *Annalen der Physik* 416.8 (1935), pp. 665–679. DOI: 10.1002/andp.19354160802.

[53] A. Z. Weber, S. Balasubramanian, and P. K. Das. Chapter 2 - Proton Exchange Membrane Fuel Cells. In: *Fuel Cell Engineering*. Ed. by Kai Sundmacher. Vol. 41. Advances in Chemical Engineering. Academic Press, 2012. Chap. 2, pp. 65–144. DOI: 10.1016/B978-0-12-386874-9.00003-8.

[54] R. R. Chandran and D-T Chin. Reactor analysis of a chlor—alkali membrane cell. In: *Electrochim Acta* 31.1 (1986), pp. 39–50. DOI: 10.1016/0013-4686(86)80058-5.

[55] A. Pfennig, W. Schabel, and H. Wolf. D5 Properties of Multicomponent Fluid Mixtures. In: *VDI Heat Atlas*. VDI-Buch. Springer Berlin Heidelberg, 2010, pp. 513–550. DOI: 10.1007/978-3-540-77877-6_23.

[56] V.L. Kubasov. In: *Electrokhimiya* 9 (1973), p. 1790.

[57] H. Vogt. Mass transfer at gas evolving electrodes with superposition of hydrodynamic flow. In: *Electrochimica Acta* 23.3 (1978), pp. 203–205. DOI: 10.1016/0013-4686(78)85047-6.

[58] H. Vogt and R. Balzer. The bubble coverage of gas-evolving electrodes in stagnant electrolytes. In: *Electrochimica acta* 50.10 (2005), pp. 2073–2079. DOI: 10.1016/j.electacta.2004.09.025.

[59] T. F. O'Brien, T. V. Bommaraju, and F. Hine. appendix. English. In: *Handbook of Chlor-Alkali Technology*. Vol. V. Springer US, 2005, pp. 1491–1582. URL: http://www.springer.com/chemistry/electrochemistry/book/978-0-306-48623-4.

[60] W. Wagner, H. Kretzschmar, R. Span, and R. Krauss. D2 Properties of Selected Important Pure Substances. In: *VDI Heat Atlas*. VDI-Buch. Springer Berlin Heidelberg, 2010, pp. 153–300. DOI: 10.1007/978-3-540-77877-6_11.

[61] J. Jörissen, P. Frania, A. Heyl, D. Hoormann, G. Polcyn, G.G. Toepell, F. Verfuß, P. Hofmann, D. Donst, F. Funck, P. Toros, and P. Woltering. *System zur Messung der Membrananspannung in Elektrolysezellen*. DE Patent App. DE201,210,009,267. 2013. URL: http://www.google.com/patents/DE102012009267A1?cl=en.

[62] T. V. Nguyen and R. E. White. A Water and Heat Management Model for Proton Exchange Membrane Fuel Cells. In: *J Electrochem Soc* 140.8 (1993), pp. 2178–2186. DOI: 10.1149/1.2220792.

[63] Bussel H. P.L.H. V., F. G.H. Koene, and R. K.A.M. Mallant. Dynamic model of solid polymer fuel cell water management. In: *J Power Sources* 71.1–2 (1998), pp. 218 –222. DOI: 10.1016/S0378-7753(97)02744-4.

[64] J. S. Yi and T. V. Nguyen. An Along the Channel Model for Proton Exchange Membrane Fuel Cells. In: *J Electrochem Soc* 145.4 (1998), pp. 1149–1159. DOI: 10.1149/1.1838431.

[65] A.A. Kulikovsky. Semi-analytical 1D+1D model of a polymer electrolyte fuel cell. In: *Electrochem Communi* 6.10 (2004), pp. 969 –977. DOI: 10.1016/j.elecom.2004.07.009.

[66] M. Šimek and I. Roušar. Calculation of the current density distribution in an amalgam electrolyser by the finite element method. English. In: *J Appl Electrochem* 18.1 (1988), pp. 96–103. DOI: 10.1007/BF01016211.

[67] R. E. White, F. Jagush, and H. S. Burney. Three-Dimensional Current Distributions in a Bipolar, Chlor-Alkali Membrane Cell. In: *J Electrochem Soc* 137.6 (1990), p. 1846. DOI: 10.1149/1.2086814.

[68] P. Byrne, P. Bosander, O. Parhammar, and E. Fontes. A primary, secondary and pseudo-tertiary mathematical model of a chlor-alkali membrane cell. In: *J Appl Electrochem* 30.12 (2000), pp. 1361–1367. DOI: 10.1023/A:1026530830265.

[69] T. F. O'Brien, T. V. Bommaraju, and F. Hine. Chlor-Alkali Technologies. English. In: *Handbook of Chlor-Alkali Technology*. Vol. II. Springer US, 2005. Chap. 5, pp. 387–442. DOI: 10.1007/0-306-48624-5_5.

[70] B. V. Tilak. Kinetics of Chlorine Evolution—A Comparative Study. In: *J Electrochem Soc* 126.8 (1979), pp. 1343–1348. DOI: 10.1149/1.2129274.

[71] F. Gestermanna and A. Ottaviani. Chlorine Production with Oxygen-Depolarised Cathodes on an Industrial Scale. In: *Modern Chlor-Alkali Technology*. Ed. by John Moorhouse. Vol. 8. Blackwell Science Ltd, 2007. Chap. 4, pp. 49–56. DOI: 10.1002/9780470999479.ch4.

[72] M. Khandelwal and M. M. Mench. Direct measurement of through-plane thermal conductivity and contact resistance in fuel cell materials. In: *J Power Sources* 161.2 (2006), pp. 1106 –1115. DOI: 10.1016/j.jpowsour.2006.06.092.

[73] J. H. Carpenter. New measurements of oxygen solubility in pure and natural water. In: *Limnology and Oceanography* 11.2 (1966). http://www.jstor.org/stable/2833432, pp. 264–277.

[74] M. Mazaheri, V. Scaini, and W. E. Veerkamp. Cause, effects, and mitigation of ripple from rectifiers. In: *Industry Applications, IEEE Transactions on* 39.4 (2003), pp. 1187–1192. DOI: 10.1109/PCICON.2002.1044988.

[75] Three-Phase Diode Bridge Rectifier. In: *Three-Phase Diode Bridge Rectifier With Low Harmonics*. Power Electronics and Power Systems. Springer US, 2007, pp. 7–21. DOI: 10.1007/978-0-387-32936-9_2.

[76] H. Weydahl, M. Thomassen, B. Børresen, and S. Møller-Holst. Response of a proton exchange membrane fuel cell to a sinusoidal current load. In: *J Appl Electrochem* 40.4 (2010), pp. 809–819. DOI: 10.1007/s10800-009-0064-3.

[77] *Quantum Leap in Sustainability*. accessed on 10.03.2015. Thyssenkrupp Electrolysis. URL: http://www.thyssenkrupp-electrolysis.com/fileadmin/documents/brochures/NaCl_ODC_Electrolysis.pdf.

[78] T. F. O'Brien, T. V. Bommaraju, and F. Hine. Handbook of Chlor-Alkali Technology. English. In: vol. II. Springer US, 2005. Chap. 6, pp. 443–464. DOI: 10.1007/0-306-48624-5_6.

[79] A. Bulan, F. Gestermann, and H.D. Pinter. *Process for the electrolysis of an aqueous solution of alkali metal chloride*. US Patent 6,890,418. 2005. URL: http://www.google.co.in/patents/US6890418.

[80] *Systèmes de production de gaz PRISM®*. accessed on 17.01.2015. AIR PRODUCTS. URL: http://www.airproducts.fr/~/media/Files/PDF/products/supply-options/gas-generation/fr-FR-prism-gas-generation-systems.pdf.

[81] G. D. Polcyn. Charakterisierung und Modellierung der Sauerstoffreduktion an Sauerstoff-Verzehr-Kathoden für die Chlor-Alkali-Elektrolyse anhand Abschaltmessung. PhD thesis. TU Dortmund, 2016.

[82] J. Newman and K. E. Thomas-Alyea. *Electrochemical systems*. John Wiley & Sons, 2012. Chap. 8. URL: http://eu.wiley.com/WileyCDA/WileyTitle/productCd-0471477567.html.

[83] *Measurement of the mains frequency*. accessed on 06.03.2010. URL: http://www.mainsfrequency.com.

CURRICULUM VITAE

Personal Data

First name	Nareshkumar
Last name	Chavan
Date of birth	23.04.1981
Nationality	Indian
E-mail	chavan@icvt.tu-clausthal.de

Educational qualification

Begin/ End	Oct 2005 to Sept 2008
University	Brandenburg Technical University, Germany
Subject	Process Engineering and Plant designing
Degree	Master of Sciences (2.0)

Begin/ End	1999 to 2003
University	North Maharashtra University, India
Subject	Chemical Engineering
Degree	Bachelor of Technology (First Class)

Experience

Oct 2014 to March 15	**Institute of Chemical and Electrochemical Process Engineering, Clausthal Zellerfeld Germany**
Designation	Scientific Assistant

July 2013 to Dec 15	**Manipal Institute of Technology, India**
Designation	Assistant Professor

Dec 2008 to till date	**Institute of Chemical Process Engineering, Clausthal Zellerfeld Germany**
Designation	Scientific Assistant

Oct 07 to Aug 2008	**Bayer Technology Services, Leverkusen Germany**
Designation	Intern (For study Project and Master Thesis)

Languages known	**Computer skills**
English (Fluent)	Aspen Custom Modeler
German (good)	Ms-Office (Excel,Word,Powerpoint,Visio)
Hindi (Fluent)	Matcad
Marathi (Fluent)	gPROMS
	VB Scripts